Investigations of nanostructures of BN, BCN and other inorganic materials

A Thesis Submitted for the Degree of

Doctor of Philosophy

By

Kalyan Raidongia

Chemistry and Physics of Materials Unit
Jawaharlal Nehru Centre for Advanced Scientific Research
(A Deemed University)
Bangalore – 560 064
February 2011

Dedicated

To

My Parents and Parents in law

DECLARATION

I hereby declare that the matter embodied in this thesis entitled "***Investigations of nanostructures of BN, BCN and other inorganic materials***" is the result of investigations carried out by me under the supervision of Prof. C. N. R. Rao, FRS and Prof. M. Eswaramoorthy at the Chemistry and Physics of Materials Unit, Jawaharlal Nehru Centre for Advanced Scientific Research, Bangalore, India and that it has not been submitted elsewhere for the award of any degree or diploma.

In keeping with the general practice in reporting scientific observations, due acknowledgement has been made whenever the work described is based on the findings of other investigators.

_____

Kalyan Raidongia

CERTIFICATE

We hereby certify that the matter embodied in this thesis entitled "***Investigations of nanostructures of BN, BCN and other inorganic materials***" has been carried out by Mr. Kalyan Raidongia at the Chemistry and Physics of Materials Unit, Jawaharlal Nehru Centre for Advanced Scientific Research, Bangalore, India under our supervision and that it has not been submitted elsewhere for the award of any degree or diploma.

Prof. C. N. R. Rao, FRS

(Research Supervisor)

Prof. M. Eswaramoorthy

(Research Supervisor)

Acknowledgements

First and foremost, I owe my deepest gratitude to my advisor **Prof. C. N. R. Rao, FRS**, for his unstinted encouragement, guidance and support from the beginning till the end. The spirit and enthusiasm he embodies in science is really contagious and motivational for the scientific fraternity, myself not excepted. I am humbly intrigued by his easy grasp of scientific ideas and passion for science and that has nourished my growth as a researcher. I am grateful to him in every possible way for giving me the opportunity to work under his esteemed guidance. His kind support and guidance have never been limited to my academic career, it has always been extended to my personal growth and development. I hope I will be able to stand up to his expectations and continue to do science till the end of my life.

My special and sincere thanks go to **Prof. M. Eswaramoorthy**. It has been a great privilege to associate with him. I am particularly grateful for the discussion I had with him on various topics. His innovative ideas and constant guidance have been instrumental in completion of my work.

I wish to acknowledge my collaborators and co-authors, Prof. Umesh V. Waghmare, Prof. Swapan K Pati, Dr. M Eswaramoorthy, Prof. A. Sundaresan, Dr. Ranjan Dutta, Prof. U. Ramamoorthy, Dr. Dinesh Jagadeesan, Dr. Mousumi Upadhyay-Kahaly, Dr. Angshuman Nag, Dr. K. P. S. S. Hembram and Dr. M. S. R. N. Kiran for their valuable contributions.

I would like to express my sincere thanks to Dr. A. Govindaraj who has helped me in carrying out various experiments.

I would like to thank the past and present chairmen of CPMU for allowing me to use the facilities of the center.

I would like to extend my warmest thanks to Selvi, Anil, Vasu, Usha Madam and Dr. Basavaraj for their help with the FESEM, XRD, UV/IR, TEM and AFM studies. I thank Saikrishna, Sudeep, Kumar and Prakash for their help during gas adsorption studies and Jitesh, Malli and Dr. Bhuvana for their help with the XPS measurements. My special thanks go to Vengadesh, Pranab, Madhu and Nitesh for their help with the magnetic and dielectric measurements. I am also thankful to Nivas for FESEM studies. I am thankful to INI center, IISc for TEM facility.

I wish to express my warm gratitude to all the faculty members of JNC. Special mention should be made of Prof. Swapan K Pati, Prof. Umesh V Waghmare, Prof. Chandrabhas Narayana, Prof. A. Sundaresan, Dr. M. Eswaramoorthy, Prof. G. U. Kulkarni and Prof. K. S. Narayan for their excellence courses.

I have been blessed with a friendly and cheerful group of fellow students. I will forever be thankful to my lab mates and friends Dr. Jagadeesan, Dr. Nag, Saikrishna, Dutta, Josena, Piyush, Amrit, Dr. Biswas, Dr. Rakesh, Nivas, Sandeep, Sabyasachi, Uzma, Dr Claudy, Krishna, Dr. Late, Neenu, Bhat, Subbu, Pawan, Monojeet, Anupama, Basant, Barun, Gopalakrishna, Prakash, Radha, Rana, Dr. Gomathi, Shipra, Krishna, Dr. Sundarayya, Mosses, Pearl, Dr. Late, Dr. Prasanth, Arpan, Ani, Sudeep, Guru, Rajsekhar, Madhu, Sameer, Dr. Reji, Dr. Vivek, Dr. Kalyani, and Manjunath. Special mention should be made of Sonai, Nitesh, Urmi, Ajmala, Kumar, Josena, Pranab, Saikrishna, Matte, Piyush, Dinesh, and Claudy. Their support and encouragement have been an indispensable part in the long run my PhD life. I'll never forget the wonderful lunches and pleasant activities we have done together, including many outings.

I would also like to take the opportunity to thank my IISc Assamese friends, most importantly Debyajyoti Da, Gitish, Pranjal, Abhijit, Nilamani, Dr. Bhaskar, Dr. Bhuyan,

Tapan, Dr. Das, Dr. Diganta, Pranab and Archita. I feel lucky enough to have their support, help and encouragement in every step of my PhD life. I always admire their positive outlook and value their friendship and support as well.

My special thanks to Mrs. Indumati Rao for her encouraging words and I greatly cherish the memory of each and every occasion when I was lucky to enjoy Madam's boundless hospitality in the great ambience of her home. I also thank Mr. Sanjay for his warm hospitality.

I thank Mrs. Shashi, Mrs. Sudha, Mr. Gowda and Mr. Victor for their help. I thank Mr. Srinath for his technical help. I thank Mr. Arokiyanathan, Mr. Narsimamoorthy and Mr. Sunil for their help.

Special thanks to Ashish, Ripan, Vikas, Ravi and Nishaj and all other technical staff in computer lab for their continuous and kind assistance.

Last but not the least, I would like to thank my beloved parents, parents in law, brothers and sisters in law for their blessings and love. I also thank my next door neighbour Ashish Da and Kabita (Mattu) for their unconditional support.

I thank my wife for standing with me in every aspect of my life. Her love and care have always been the greatest strength for me.

Finally, I thank God almighty for strengthening me throughout my life.

Preface

The thesis consists of seven chapters, of which the first chapter presents a brief overview of nanomaterials. Chapter 2 deals with the transformations of elemental nanowires of metals and silicon to nanotubes of the corresponding oxides and chalcogenides through Kirkendall effect. The study includes aspects related to the mechanism and the kinetics of the nanowire-nanotube transformation. Synthesis and characterization of Al_2O_3, MoO_3 and ZnO nanorod brushes using amorphous carbon nanotubes as templates are discussed in Chapter 3.

In Chapter 4, synthesis, characterization and properties of homogeneous BC_4N nanotube brushes and mesoporous microspheres are discussed. Both nanotubes and microspheres of BC_4N are stable up to 900 °C and exhibit selective uptake of CO_2. Chapter 5 describes the synthesis, characterization and properties of graphene analogues of BCN. Graphene analogues of BCN exhibit higher electrical resistivity than graphene, but weaker magnetic features. They are microporous exhibiting large surface area and high propensity for CO_2 uptake.

Chapter 6 deals with the synthesis, characterization and properties of BN nanostructures. Single- and few-layer graphene analogues of BN have been prepared by reacting boric acid with different proportions of urea. The surface area of graphene-like BN increases with the decreasing number of layers. Mechanical properties of composites of polymethylmethacrylate with graphene-like BN have also been investigated. Improvement in mechanical properties is favored by smaller number of BN layers. This chapter also describes generation of nanopans and nanosheets of graphene-like BN by the vapor phase reaction of NH_3 and BBr_3.

Chapter 7 presents the multiferroic and magnetoelectric properties of core-shell $CoFe_2O_4$@$BaTiO_3$ nanostructures. These core-shell nanotubes exhibit 4.7% magnetocapacitance at 310 K.

Table of Contents

CHAPTER 1

Nanomaterials: A brief overview

1.1. Introduction

Materials with structural features between those of single atoms or molecules and bulk materials are known as nanomaterials. The prefix "nano", denoting a factor of 10^{-9} has derived from the Greek "nanos," meaning "dwarf". Nanomaterials have at least one dimension in the nanometer (*i.e*. a billionth of a meter) range. Properties of these materials are significantly different from those of atoms as well as bulk materials. Similar to quantum mechanics, on nanometer length scale, materials may possess new physical properties or exhibit new physical phenomena. Some of these properties are already known. For example, band gaps of semiconductors can be tuned by varying their size and shape.[1] There may be many more unique physical properties not known to us yet. These new physical properties or phenomena will not only satisfy everlasting human curiosity, but also promise new advancement in technology. For example, ultra-strong and ultra-light multifunctional materials are possible from hierarchical nanostructures. Nanomaterials also promise the possibility of the miniaturization of current and new instruments, sensors and machines that will greatly impact the world we live in.

Unwittingly, nanomaterials have been fascinating human minds over thousands of years. Brilliant red colour of gold nanoparticles was used by the Chinese in colouring their ceramic porcelains more than a thousand years ago. In the eighth century, Middle Eastern sword makers had unknowingly used

nanotechnology to give its unusual strength and sharpness to Damascus sword. Throughout Europe, metal nanoparticles have been using in stained glass windows of cathedrals since 17th century. Although nanomaterials had been used many

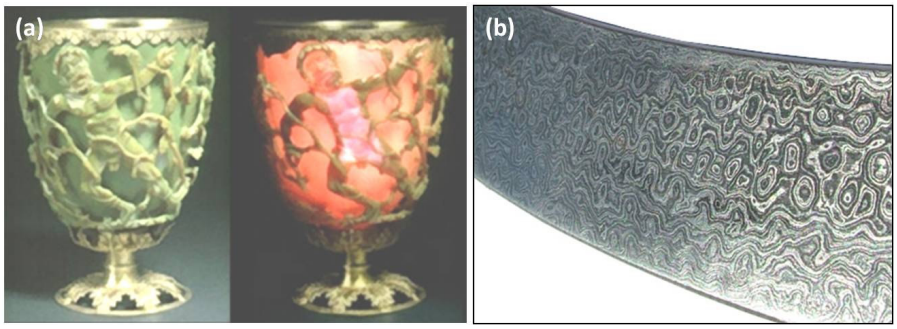

Figure 1.1: (a) The 4th century Lycurgus Cup of dichroic glass, containing gold and silver colloids. This glass changes colour when held up to light. (b) the complex surface pattern in the Damascus sword.

centuries ago, the first systematic study on these materials was carried out in the 1850s by Michael Faraday. In those groundbreaking studies, he has observed the particles size dependent colour of the gold sols. The tremendous potentials and the importance of nanotechnology were realized by Nobel laureate Richard Feynman. He had motivated the researchers towards the field of nanoscience in his often-cited lecture entitled ‘‘There is plenty of room at the bottom’’ delivered at the annual meeting of the American Physical Society at the California Institute of Technology (Caltech) in 1959. The explosive growth of the nanotechnology research started in 1981 when Binnig and Rohrer at IBM Zurich invented the scanning tunneling microscope (STM), the first instrument to generate real space images of surfaces with atomic resolution.[2] This discovery was recognized by the 1986 Nobel Prize in Physics along with the inventor of the electron microscope.

In recent years, nanotechnology has become one of the most important and exciting forefront research areas in chemistry, physics, engineering and biology. This

is primarily because of the availability of new synthetic strategies and tools for characterization and manipulation of the nanomaterials. Scanning tunneling microscope (STM) image of the quantum corral of 48 Fe atoms placed in a circle of 7.5 nm radius shows the current status of characterization tools for nanomaterials (Figure 1.2). Heinrich and his co-workers were able to probe magnetic anisotropy in individual atoms, opening up the possibility of giant magnetic anisotropy that can be engineered at the atomic scale.[3]

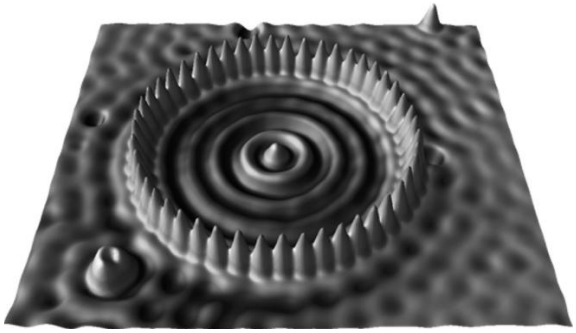

Figure 1.2: STM image of a quantum corral of 48 Fe atoms placed in a circle of 7.3 nm (IBM Research).

1.2 Properties of nanomaterials

Properties of nanomaterials are significantly different from those of atoms as well as bulk. The main feature of nanomaterials is that physical dimensions determine the properties. The changes in the properties at this length scale originate from different causes in different materials.

1.2.1 Electronic structure

The understanding of the electronic structure of a material is very important as it determines the properties and functionalities of the respective material. Materials can be divided into three broad categories metal, semiconductor and insulator. Metals possess a partially filled electronic band with a continuum of energy levels above the Fermi energy. Because of these continuum energy levels metals conduct

electrons. When size of a metal is reduced to nanometer regime the continuum of electronic states breaks down and as a result metal at nanometer size becomes insulating (Figure 1.3).[4-6] In the case of semiconductors, the Fermi energy lies in

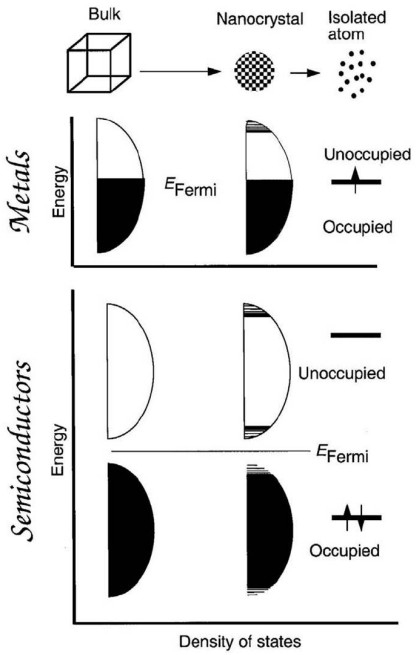

Figure 1.3: Schematic illustration of the density of states for metal and semiconductor nanocrystals (from reference 4).

between the filled and unfilled energy levels (Figure 1.3). The energy difference between the top of the valence band and the bottom of the conduction band is known as the band-gap of the material. When an electron is promoted from the valence to conduction band, an electron–hole pair (exciton) is created. The physical separation between the electron and hole (known as exciton Bohr radius (r_B)) varies depending on the semiconductor composition. In a bulk semiconductor crystal, r_B is significantly smaller than the overall size of the crystal and hence, the exciton is free to migrate throughout the lattice. However, in a nanometer size semiconductor, r_B is of the same order of magnitude as the diameter of the nanocrystal, giving rise to quantum confinement of the exciton. Exciton quantum confinement results in discrete energy levels rather than the continuous bands of a bulk semiconductor

crystal (analogous to the "particle-in-a-1D-box" model) and the energy level spacing is inversely proportional to square of the length of the nanocrystals. Nanocrystals exhibiting quantum confinement are called quantum dots. Due to the small size of a quantum dot, the addition or subtraction of a single atom significantly changes the dimension and band-gap of the nanocrystal. As a result the band-gap of quantum dots can be fine-tuned by changing the diameter of the crystal, as long as the dimensions are smaller than r_B.[4,6,7]

The density of states (DOS) of the nanostructures is sensitive to both size and shape of the crystal.[6,7] A schematic illustration of the density of states in one band of a semiconductor as a function of dimensions is shown in Figure 1.4. In case of 3D it is a continuous function while for 2D nanostructures it is a step function with steps

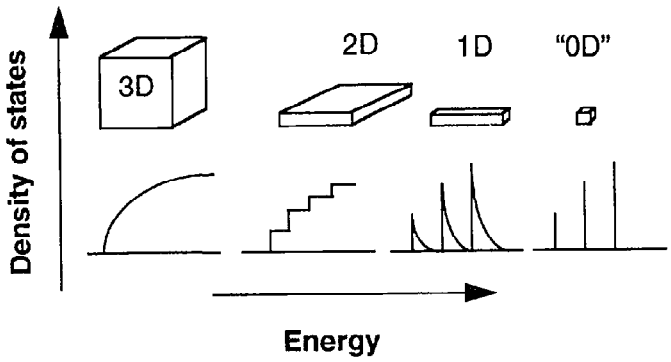

Figure 1.4: Density of states in one band of a semiconductor as a function of dimensions.[6]

occurring at the energy of each quantized level. In the case of 1D nanostructures, Van Hove singularities are observed and for 0D nanostructures, the density of states shows quantization at particular energy levels.

1.2.2 Optical properties

The electronic absorption of metal nanocrystals originates from the collective oscillation of the polarized electrons in the conduction band, induced by the electromagnetic field of the radiation.[8-11] This collective oscillation has a frequency

that resonates with the frequency of the absorbed light. This is known as surface plasmon resonance absorption. The resonance frequency of the nanocrystals increases with the decrease in the particle size. The absorption spectra of spherical Au nanoparticles of different sizes are shown in Figure 1.5.[8] As the size of the Au nanocrystals increases, the plasmon band shifts to the red. The surface plasmon absorption was theoretically explained by Mie in 1908.[12] Optical property of

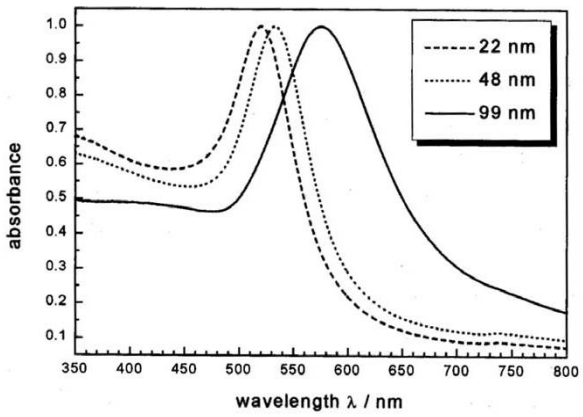

Figure 1.5: Absorption spectra of Au nanocrystals of various diameters (from reference 8).

semiconductor nanocrystals is determined by the confinement of the electronic motion to a length scale that is comparable to the mean free path of the electrons in the bulk material. The reduction of a semiconductor crystal-size beyond the bulk excitonic Bohr radius induces a larger band gap that causes blue-shifts in the absorption wavelength. The size quantization effects in semiconductor nanocrystals are described by Brus based on the effective mass approximation.[13,14] Thus bulk CdS, yellow in color exhibits an excitonic absorption around 550 nm, which gradually shifts into the UV region as the nanocrystal diameter is varied below 10 nm. The absorption band can be systematically varied in the ranges of a few 100 nm by changing the size of the semiconductor nanocrystal.[15] The excitonic nature of the absorption band permits direct correlation of the band gap of the semiconductor nanocrystal with the absorption edge. In addition to interesting absorption properties,

the semiconductor nanocrystals also exhibit luminescent behaviour.[16-19] The emission of these nanocrystals can be tuned by varying the diameter or diameter distribution of the nanocrystals.

1.2.3 Magnetic properties

Magnetic properties of the nanomaterials are very interesting from both fundamental and applied points of view. The coercivity (H_c) of the magnetic nanoparticles increases with the decrease in the diameter (D) of the particles till a particular diameter and thereafter coercivity begins to decrease. At this critical diameter (D_c), the particle changes from being a multi-domain particle to a single-domain particle.

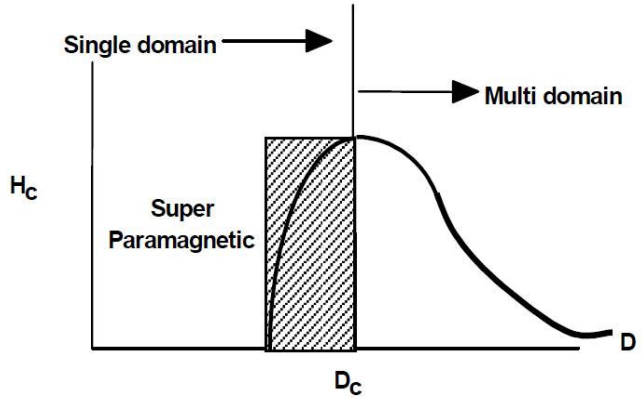

Figure 1.6: Schematic illustration of the changes in the coercivity of a magnetic particle with change in the diameter.

The value of critical diameter is normally a few tens of nanometers. If the particles size reduced further the thermal energy can overcome the anisotropy energy barrier below a critical diameter and hence the coercivity becomes zero. Nanocrystals below this critical diameter are said to be superparamagnetic. As superparamagnetic behaviour, is caused by thermal flipping of the anisotropic barrier to magnetization reversal, below a certain temperature the temperature induced flipping or relaxation can be arrested and the nanocrystals acquire a finite coercivity. This critical temperature is called blocking temperature.[20] A schematic illustration of the

changes in the coercivity of a magnetic particle with change in the diameter is shown in Figure 1.6.

Nonmagnetic oxides such as CeO_2, Al_2O_3, ZnO, In_2O_3 and SnO_2 exhibit room-temperature ferromagnetism when the particles size reduced to nanometer regime (7–30 nm diameter).[21] The origin of such ferromagnetism may be the exchange interactions between localized electron spin moments resulting from oxygen vacancies at the surfaces of nanocrystals. Thus, ferromagnetism may be a universal characteristic of nanoparticles of metal oxides.

1.2.4 Other properties

In a wide variety of materials ranging from metals to semiconductors to insulators, a decrease in melting temperature has been observed with decreasing nanocrystal size.[22] Such phenomena can be explained on the basis of large number of surface atoms in the nanostructures which are coordinatively unsaturated. The surface atoms are highly energetic and hence require less thermal energy for melting. The smaller the nanocrystal, the larger the contribution from the surface to the overall energy of the system and thus, leading to further depression of melting temperature. The nanometer size also has significant influence on the solid to solid phase transitions of materials.[23] For example, in the case of wurtzite to rock salt structural transformation of CdSe both the thermodynamics and kinetics are altered in finite size, as compared to bulk CdSe. Bulk gold is chemically inert and thus considered to be not active or useful as catalyst.[24,25] However, gold nanoparticles exhibit excellent catalytic properties.[26]

1.3 Synthesis of nanomaterials

A large number of innovative and elegant synthetic strategies have been developed to synthesize nanomaterials of almost all chemical compositions with a wide variety of morphology and size. Based on the number of dimension present in their shape nanomaterials can be classified into three broad categories: zero dimensional (0D), one dimensional (1D) and two dimensional (2D).

1.3.1 Zero-dimensional nanomaterials

Zero dimensional (0D) nanomaterials have all the three dimensions in the nanometer regime (1-100 nm). These materials are usually denoted by nanoparticles, nanoclusters, nanocrystals or quantum dots. The term nanoparticles generally encompass all the zero dimensional nanomaterials. Nanoclusters refer to a tiny chunk of the bulk measuring (1-10 nm) with well defined arrangement of a definite number of constituent atoms. The atoms arrange themselves on the basis of maximizing the

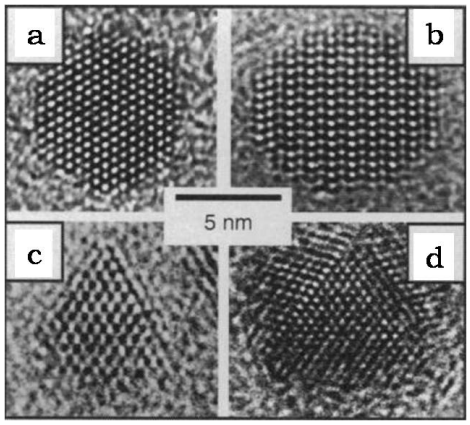

Figure 1.7: (a) and (b) TEM images of CdSe nanocrystals with hexagonal structure, (c) and (d) TEM image of CdS/HgS/CdS quantum dot quantum well (adopted from reference 27).

number of bonds and minimizing the number of atoms on the surface. They nucleate from atoms and enter into a size range where they behave electronically as molecular nanoclusters. As the number of atoms increases further they cross over into

nanocrystals where the quantum size effects dominate their electronic properties. Single-crystalline 0D nanomaterials are usually referred as nanocrystals. Figure 1.7 shows the TEM images of CdSe and CdS/HgS/CdS quantum dots prepared by Weller and co-workers.[27]

Various physical and chemical methods have been demonstrated to generate 0D nanomaterials.

Physical methods

Physical methods are usually employed for the large scale production of nanoparticles with high purity. However, the physical methods have poor control over the shape and size distributions. Most commonly used physical methods are metal evaporation, ball milling and electrodeposition. Metal evaporation is done by various techniques like arc discharge, ion sputtering, laser ablation, laser pyrolysis and spray pyrolysis.[28] All these methods involve the evaporation of a solid material to form a supersaturated vapor followed by nucleation of the nanoparticles. The size of the nanoparticles can be controlled either by choosing a proper source of evaporation, or by slowing the growth rate by introducing gas molecules to collide with the particles.

Chemical methods

Several chemical methods have been developed to achieve a good control over size, shape and composition of the nanoparticles. Commonly encountered chemical methods are the reduction of metal salts, thermal decomposition of organometallic compounds and sol-gel processes. Chemical evolution of a nanoparticle involves three distinct stages; seeding, particle growth and growth termination by capping. Control over these stages is essential to obtain monodisperse nanoparticles of a definite size and shape with a desired chemical composition. Chemical methods have

been employed to obtain nanoparticles of wide variety of materials including metals, alloys, semi-conductors, ceramics and polymers.[29,30]

1.3.2 One-dimensional nanomaterials

One-dimensional nanomaterials (1D) have one macro-scopic dimension in the micrometer range and remaining two are in the nanometer regime. Nanotubes, nanowires, nanorods, nanobelts and nanohelics are well-studied example of 1D nanomaterials. A range of unique properties such as thermal, mechanical, electronic, optoelectronic, optical, nonlinear optical and field emission are associated with 1D nanomaterials.

Most popular and widely studied 1D nanomaterials are carbon nanotubes (CNTs). The nanotubes discovered by Iijima,[31] as an electron microscopic marvel has opened up a new era in science and technology. There has been numerous research activity related to the synthesis, structure, properties and applications of CNTs. The strongest and the stiffest materials on the earth have remarkable

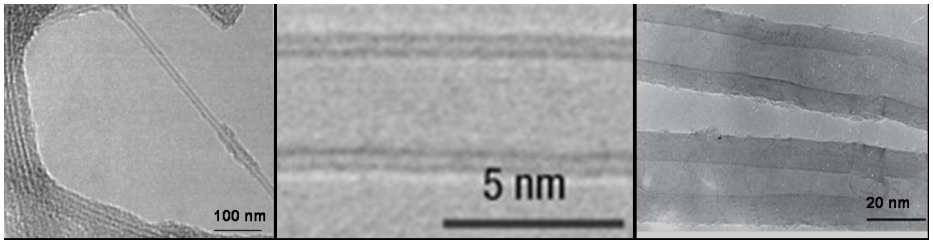

Figure 1.8: TEM images of (a) SWNTs, (b) DWNT and (c) MWNTs.[32-34]

electronic properties and many other unique characteristics. Due to their novel properties CNTs can find applications in diverse fields like materials science, medicinal chemistry and engineering. A number of techniques have been developed to produce carbon nanotubes in sizeable quantities including arc discharge, laser ablation and chemical vapor deposition. CNTs are categorized as single-walled nanotubes (SWNTs), double-walled nanotubes (DWNTs) and multi-walled

nanotubes (MWNTs), based on the number of graphene layers rolled in on themselves to form the tube shape. Figure 1.8 shows the TEM images of single-wall, double-wall and multi-wall CNTs. [32-34]

A large number of synthetic strategies have been adopted to fabricate 1D nanomaterials with different morphologies.[35] These synthetic strategies can be generally grouped into four categories:

(1) Spontaneous growth:

(a) Evaporation (or dissolution)-condensation

(b) Vapor (or solution)-liquid-solid (VLS or SLS) growth

(c) Stress-induced recrystallization

(2) Template-based synthesis:

(a) Electrodeposition route

(b) Direct template filling

(3) Electrospinning

(4) Lithography

Spontaneous growth

Spontaneous growth of materials is driven by the reduction of Gibbs free energy. The reduction of Gibbs free energy can be achieved by phase transformation, chemical reaction or release of stress. For the formation of a 1D nanomaterials, the crystals have to grow along a certain orientation faster than other directions. For 1D nanomaterials of uniform diameter the crystals have to grow only in one direction and growth along other directions has to restrict. The growth conditions, defects and the impurities on the growth surfaces can affect the morphology of the final products.

There are several mechanisms to result preferential growth in one direction for example,

(a) Different facets in a crystal have different growth rate. For example, silicon with a diamond structure, the growth rate of {1 1 1} facets is smaller than that of {1 1 0}.

(b) Presence of imperfections in specific crystal directions such as screw dislocation.

(c) Preferential accumulation or poisoning by impurities on specific facets.

The evaporation-condensation growth is one of the oldest and most widely used techniques for growing one dimensional nanomaterials. In 1955 Sears had grown fine whisker of mercury, zinc, cadmium, silver and cadmium sulphide by this method, the

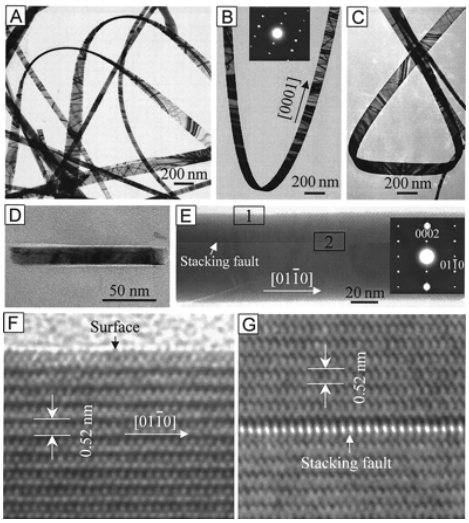

Figure 1.9 SEM and TEM pictures of ZnO nanobelts (from reference 38).

growth process was explained by axial screw dislocation induced anisotropic growth.[36,37] Wang and his co-workers have grown the single crystal nanobelts of ZnO, SnO_2, In_2O_3 and CdO, by evaporating the corresponding bulk metal oxides at high temperature under vacuum and subsequently condensing the vapour on an alumina substrate, placed at relatively lower temperature.[38] Figure 1.9 shows the SEM and TEM image of ZnO nanobelts obtained by Wang and his co-workers. Later on, number of people have employed this technique to generate wide variety of 1D

nanomaterials, these includes left-handed helical nanostructure, nanorings and nanowires of ZnO, nanowires of Ga_2O_3, MgO, Al_2O_3, CuO and Si, nanorods of SnO_2 and nanobelts of PbO_2 and Ga_2O_3.[39-42]

In dissolution-condensation process, the growth species first dissolved into a solvent, and then diffuse through the liquid to deposit on the surface of growing nanostructures. The growth medium of dissolution-condensation process is different from evaporation-condensation process. Single crystalline nanowires of Se, Se_xTe_y, ZnTe, Mn_3O_4 and $BaTiO_4$, nanorods of $CdWO_4$ and ZnO and nanotubes of $H_2Ti_3O_7$ have been obtained by this process.[43-49] In dissolution-condensation process alien nanoparticles can serve as seeds for heteroepitaxial growth of 1D nanomaterials. Ag nanowires of 30-40 nm in diameter with lengths of several tens of microns have been synthesised using platinum nanoparticles as growth seed.[50] The anisotropic growth was achieved by preferential blocking of specific facets by polyvinyl pyrrolidine (PVP).

1D nanomaterials obtained by the evaporation (dissolution)-condensation deposition usually have faceted morphology with small aspect ratios, particularly when grown in liquid medium. However, anisotropic growth induced by axial imperfections, such as screw dislocation and stacking faults, or by impurity poisoning, can result in the growth of nanowires with very large aspect ratios.

In vapor-liquid-solid (VLS) growth the evaporated growth species diffuses and dissolves into a liquid droplet. The surface of the liquid has a large accommodation coefficient and is therefore a preferred site for deposition. Saturated growth species in the liquid droplet will diffuse to interface and precipitate at the interface between the substrate and the liquid. The precipitation will first follow nucleation then crystal growth. Continuous precipitation and growth will separate the substrate and the

liquid droplet, resulting 1D growth of the nanomaterial. Figure 1.10 shows a schematic illustration showing the growth of a nanowire via VLS mechanism. The

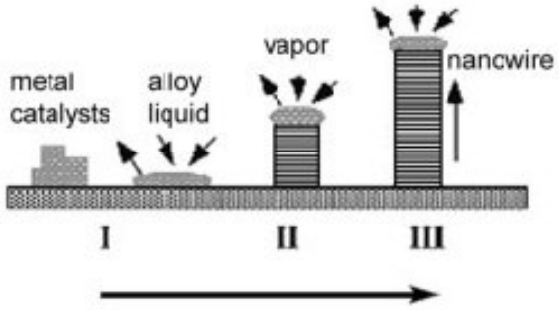

Figure 1.10: Schematic illustration showing the growth of nanowires via VLS mechanism.[35]

growth of Si and Ge nanowires with liquid gold droplets as catalyst are typical examples of VLS growth.[51,52] Semiconductor nanowires of III-V materials (such as GaAs, GaP, GaAsP, InAs, InP, InAsP) and II-VI materials (such as ZnS, ZnSe, CdS, CdSe) and IV-IV materials of SiGe have been grown using VLS method.[53]

Solution-liquid-solid (SLS) growth is similar to VLS growth but the reaction take place at solution phase and at relatively lower temperatures then VLS process. The SLS method was applied for the synthesis of InP, InAs, GaAs and Si nanowires.[54-57] The diameter and the lengths of nanowires grown by VLS and SLS methods can be controlled by controlling the size of the liquid catalysts and the growth time.

1D nanomaterials can also be synthesized by stress-induced recrystallization. Nanowires with diameter as small as 50 nm have been synthesised by applying pressure on solids at elevated temperature.[58] The growth rate of the nanowires was found to be proportional to applied pressure. Unlike other spontaneous growth processes, here growth proceeds from the base, not from the tip. Dislocations at the base direct the uni-directional growth of the nanostructure.[59]

Template-based synthesis

Template-based synthesis is the most straightforward and versatile method in generating a wide range of nanomaterials. In this approach the template serve as a scaffold within which the required materials loaded and shaped into morphology complimentary to that of template. This method has been used to fabricate a wide variety of nanomaterials like, nanorods, nanotubes, nanowires, nanohelics, nanospheres, naonobelts etc. Various templates have been explored for the growth of 1D nanomaterials. The most commonly used templates are anodized alumina membrane, radiation track-etched polymer membrane, mesoporous materials, zeolites and carbon nanotubes. These templates can be loaded with desired materials using either an electrodeposition route or by direct template filling.

Electrodeposition involves diffusion of precursors into the pores of the templates by applying an external electric field. In the next step, decomposition of the precursors and the deposition of growth species take place simultaneously. The resultant nanostructures can be harvested by removing the templates using a post-

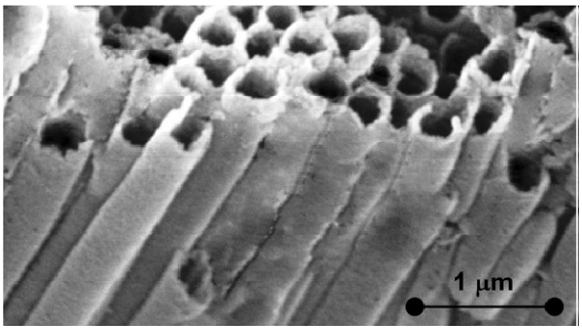

Figure 1.11: SEM image of the cross-sectional view of CeO_2 nanotubes (from reference 60).

synthetic treatment such as chemical etching or calcination. A variety of 1D nanomaterials have been obtained by using this technique, the examples include metals, semiconductors, ceramics and organic polymers. Figure 1.11 shows an SEM

image of CeO_2 nanotubes array obtained by the electrodeposition of $CeCl_3 \cdot 7H_2O$ into the pores of anodic alumina membranes.[60]

Direct template filling is the most popular method in the preparation of 1D nanomaterials. The template can be filled with a liquid precursor or precursor mixture using techniques like sol-gel processing, melt and solution filling, chemical vapour deposition, centrifugation etc. In sol-gel processing the templates are placed in a stable sol for various periods of time to drive the sol into the pores by making use of capillary force. Good wet-ability of the templates surface for the sol is essential for this technique. After filling the pores templates are withdrawn and dried prior to the firing at elevated temperature. Nanotube arrays of $InVO_4$ and $InVO_4$–acac grown in polycarbonate templates by means of capillary force induced filling.[61]

Metals with relatively low melting points such as Bi, In, Sn and Al could be directly injected as liquids into the pores of anodic alumina membrane and subsequent solidification results into highly crystalline nanowires.[62,63] Polymer fibrils were prepared by filling a monomer solution with a polymerization reagent into the pores of a template and then polymerizing the solution. Some researchers have also used chemical vapour deposition (CVD) to grow nanowires inside the pores of templates. For example, Ge nanowires were grown by diffusing Ge_2H_6 gas into the mesoporous silica at high temperature.[64] Template filling assisted with centrifugation is another inexpensive method for mass production of nanorod arrays. Nanorod arrays of lead zirconate titanate (PZT), silica and tiatania have been grown by this method.[65] Although nanowires synthesized using these methods are usually polycrystalline, single crystal nanowires have also been obtained under carefully controlled conditions. Compound 1D nanomaterials can also be obtained using

consumable templates. In this method first nanowires or nanorods of a constituent element is prepared and then reacted with suitable reagents to form the compound nanomaterials.

Electrospinning

Electrospinning uses electrical force to produce polymer fibers with nanometre scale dimensions. Electrospinning occurs when the electrical forces at the surface of polymer solution or melt overcome the surface tension and causes an electrically charged jet to be ejected. More than 30 polymer fibers with diameters ranging from 40 nm to 500 nm have been successfully produced by electrospinning.[66,67]

Lithography

Lithography represents another route to the synthesis of 1D nanomaterials. Various lithographic techniques such as electron beam lithography, ion-beam lithography, STM lithography, X-ray lithography, proxial-probe lithography and near-field photolithography have been explored in the fabrication of nanomaterials.

1.3.3 Two-dimensional nanomaterials

Two-dimensional (2D) nanomaterials such as nanowalls and nanosheets have at least one dimension in nanometer region. Unlike layered materials, nanosheets should be free from electrical and chemical interaction with other materials. The 2D nanomaterials are very exciting from the fundamental physics point of view and led to the discovery of new phenomena like quantum Hall effect[68,69] and giant magneto-resistance.[70,71] New devices such as high electron mobility transistors,[72] inter-sub-band infra-red detectors and quantum cascade lasers in semiconductor systems,[73] spin-valves in metallic systems[74] have been created based on these nanomaterials.

Several methods are being used for the preparation of two-dimensional nanomaterials that includes thermal exfoliation of layered materials, chemical vapour

deposition (CVD), atomic layer deposition, physical vapour deposition, sol-gel processing and exploitation of the liquid-liquid interface.

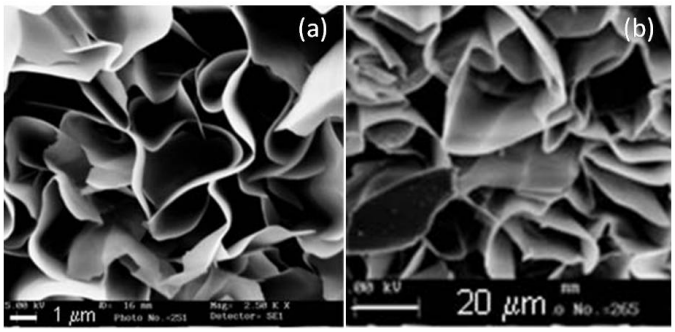

Figure 1.12: SEM image of the (a) GaS nanowalls and (b) GaSe nanowalls.[75]

Thermal exfoliation method involves direct heating of the corresponding layered materials at required temperature. SEM image of GaS and GaSe nanowalls obtained by the thermal treatment of corresponding powder is shown in Figure 1.12.[75]

In chemical vapour deposition a volatile compound of the material to be deposited chemically reacts with other gases to produce a non-volatile solid that deposits atomistically on a substrate. A variety of CVD methods have been developed, depending on the types of precursors used, the deposition conditions applied and the forms of energy introduced to activate the chemical reactions. For example, when metal-organic compounds are used as precursors, the process is generally referred to as MOCVD (metal-organic CVD), when plasma is used to promote chemical reactions, this is a plasma enhanced CVD or PECVD and when low pressure applied this is called a low pressure CVD (LPCVD). Carbon nanowalls of thickness one to several nanometers have been grown on various substrates using microwave plasma-enhanced chemical vapour deposition.[76] Later on, this carbon nanowalls have been used as templates to obtain nanowalls of other inorganic materials, including Au, Cu, Zn, ZnO and TiO_2.

Atomic layer deposition (ALD) is a unique method for 2D nanomaterials having a self-limiting growth nature. In this method each time only one atomic or molecular layer can grow and so offers the best possibility of controlling the thickness and the surface smoothness.

Physical vapour deposition involves transformations of the growth species to gaseous state followed by atomistic deposition on a suitable substrate. The process involves no chemical reactions. The thickness of the deposits can vary from angstroms to millimetres. In general, PVD methods can be divided into two groups: evaporation and sputtering. In evaporation, the growth species are removed from the source by thermal means. In sputtering, atoms or molecules are dislodged from solid target through the impact of gaseous ions (plasma).

Sol-gel processing, a widely used technique in the synthesis of inorganic and organic-inorganic hybrid materials are capable of producing nanomaterials of all dimensions. Most commonly used sol-gel methods for 2D nanomaterials are spin-

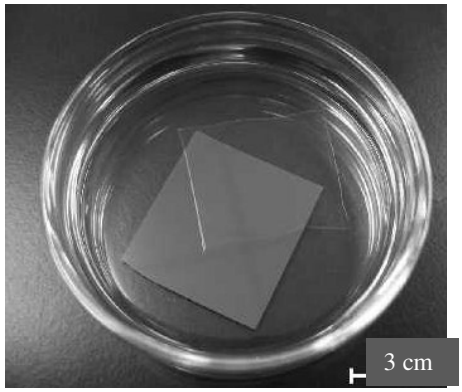

Figure 1.13: Optical micrograph of an IPN hybrid nanofilm detached from the substrate and floating in ethanol (from reference 77).

coating and dip-coatings. In dip-coating, a substrate is immersed in a solution and then withdrawn at a constant speed. A spin coating consists of four stages: delivery of solution to the substrate centre, driving of the liquid across the substrate (spin-up),

removal of the excess liquid from the substrate (spin-off) and evaporation. Number of polymer and polymer-composite thin-films have been grown by spin-coating.[77,78] Figure 1.13 shows the optical micrograph of an ultrathin organic–inorganic hybrid films with an interpenetrating network (IPN) structure detached from the substrate and floating in ethanol, obtained by spin-coating method.

The liquid-liquid interface has also been exploited for the fabrication of 2D nanomaterials. The method involves dissolving an organic precursor of the relevant metal in the organic layer and the appropriate reagent in aqueous layer. The product formed by the reaction at the interface contains ultrathin nanocrystalline films. This simple technique has shown to yield nanocrystalline films of metals such as Au, Ag, Pd, Cu and chalcogenides like CdS, CdSe, ZnS, CoS, NiS, CuS, PbS and oxides such as γ-Fe_2O_3, ZnO and CuO.[79-88]

Among all classes of nanomaterials, graphene, the strictly two dimensional (2D) flat monolayer of carbon atoms, has become the most promising candidate for the next generation nanoelectronic devices and other nanomaterials based applications.[89-96] Due to its unique chemical, physical and mechanical properties, graphene has become one of the most exciting topics of research in the last few years.[90,97-99] Unlike other materials, its charge carriers follow Dirac equation rather than the Schrodinger equation. It also exhibits unusual fractional quantum Hall effect and conductivity behaviour. Graphene is opening up a new research area for materials science and condensed-matter physics. Despite the theoretical prediction of the thermodynamic instability of a graphene sheet, a good number of efforts have been devoted to obtain good quality graphene samples.[100] Single-layer graphene was first prepared by micromechanical cleavage from highly ordered pyrolyitc graphite (HOPG) by using scotch tape and then transferred on to a silicon

substrate.[89] A chemical method to prepare graphene involves oxidation of graphite to graphitic oxide followed by exfoliation and reduction of graphene oxide.[101-103] Graphene layers have been grown on different transition metal substrates by

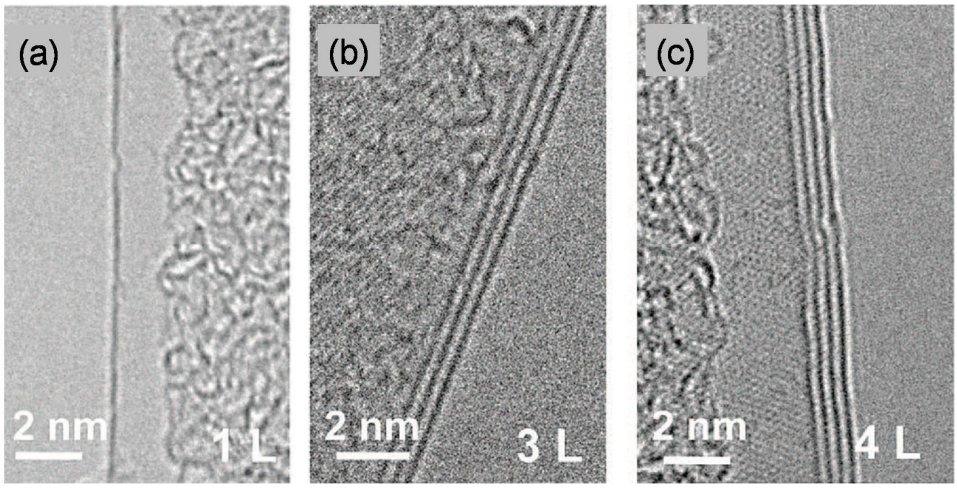

Figure 1.14: TEM images of the edges of graphene consisting of (a) one, (b) three and (c) four layers (adopted from reference 104).

decomposing a variety of hydrocarbons such as methane, ethylene, acetylene and benzene; the number of layers varying with the hydrocarbon and reaction parameters.[104] Figure 1.14 shows TEM images of single and few layer graphene deposited on polycrystalline Ni films by CVD method. Graphene can also be prepared by heating nanodiamond in an inert or a reducing atmosphere.[105] Two-three layers of graphene have been obtained by arc evaporation of graphite in the presence of hydrogen.[106]

1.4 Characterization of nanomaterials

The tremendous growth in nanoscience and nanotechnology in the past few years has been possible due to the increased availability of sophisticated methods to characterize nanomaterials.[107] These techniques include electron microscopy and

scanning probe microscopies, in addition to standard techniques such as X-ray and neutron diffraction, X-ray scattering and various spectroscopies. Characterization of nanomaterials includes the determination of the atomic and electronic structures and other important properties along with size and shape. Some of the important methods employed for characterization of nanostructures are described below.

1.4.1 Electron microscopies

An electron microscope is a type of microscope that uses a particle beam of electrons instead of photons to illuminate the specimen and creates a magnified image of it. Electrons have a wavelengths of about 100,000 times shorter than visible light and hence can achieve a magnifications of up to 2,000,000x, whereas, non-confocal light microscopes are limited to 2000x magnification. There are two general types of electron microscopes complementary in style and operation, transmission electron microscope (TEM) and scanning electron microscope (SEM). In a TEM a

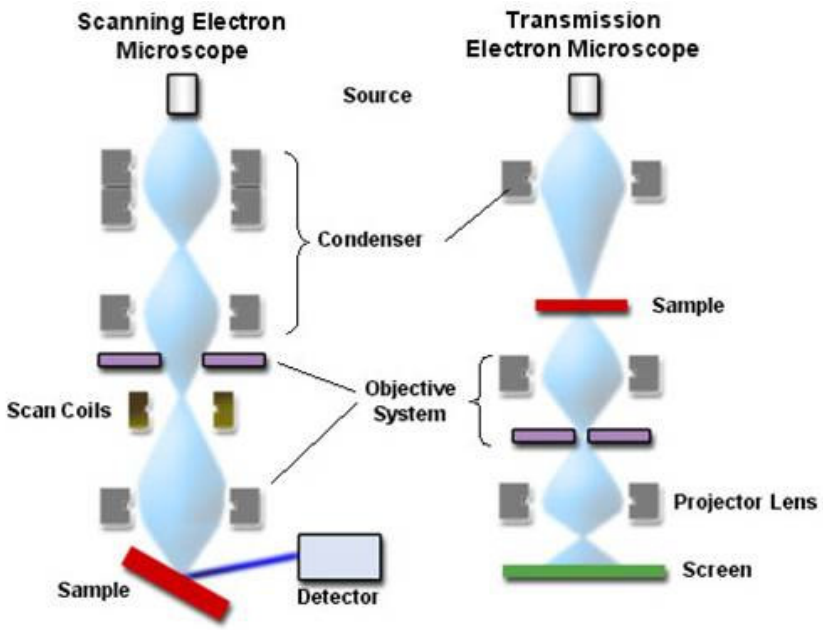

Figure 1.15: Instrumental diagram of TEM and SEM

beam of electron is transmitted through an extremely thin specimen.[108,109] The changes in the electron beam arising from scattering by the specimen carries information about the structure of the specimen that is magnified by the objective lens system of the microscope. The basic principle of TEM is same as optical microscope. Electromagnetic lenses are used here to focus the electrons in a thin beam similar to glass lenses of optical microscope. SEM produce images by scanning the surface of the sample with a high-energy electron beam, then detecting signals from the interaction of the incident electrons with the sample's surface.[110] At each point on the specimen the incident electron beam loses some energy and that lost energy is converted into other forms, such as heat, emission of low-energy secondary electrons, light emission (cathodoluminescence) or x-ray emission. The varying intensity of any of these signals in a position corresponding to the position of the beam on the specimen is transformed into an SEM image. Simplified diagrams of TEM and SEM are shown in Figure1.15.

1.4.2 Atomic force microscopy

Atomic force microscopy (AFM) is one of the scanning probe microscopes employed for real topographical images of the sample surfaces.[111] In a typical AFM setup, the deflection of a microfabricated cantilever with a sharp tip is measured by reflecting a laser beam from the back side of the cantilever as it scans over the surface of the sample (see Figure 1.16). Several variants of AFM are used to investigate surface forces and measure topography on the nanoscale, for example, contact mode, tapping or intermittent contact mode and non-contact mode. AFM techniques are used to measure surface properties on the nanometer scale such as frictional force, hardness, surface charge distribution, surface magnetization, yield stress, elastic and plastic deformation dynamics etc. AFM is also used as a

lithographic technique like dip-pen lithography. Using the conducting cantilever probe in contact mode AFM can be used to obtain current (I) versus voltage (V) measurements of a given nanomaterial. AFM has a typical vertical distance resolution of 0.01 nm.

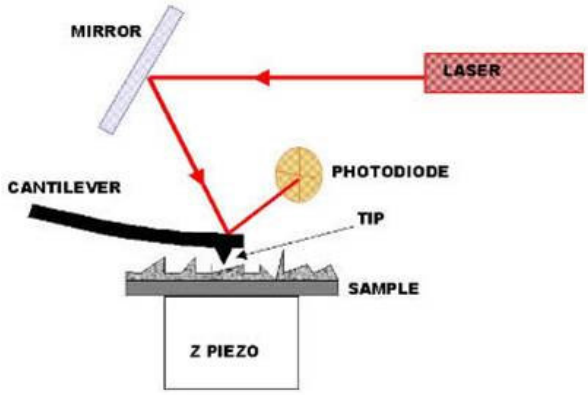

Figure 1.16: Instrumental diagram of AFM.

1.4.3 Scanning tunneling microscopy

Scanning tunneling microscopy (STM) is a technique used for viewing surfaces at the atomic level.[111] Using a tunneling current, STM probes the density of the states of a material. When a conducting tip is brought near a metallic or semiconducting surface, a bias allows electrons to tunnel through the vacuum between them. For low voltages, this tunneling current is a function of the local density of states at the Fermi level of the sample. Variations in the current as the probe passes over the surface are transformed into an image. STM is useful for obtaining information about the electronic states and the morphology of nanomaterials of different dimensionalities.

1.5 Nanotoxicology

Nanotechnology has virtually unlimited potential for technological development but researchers should also be concerned about the potential harm it can cause to people and the environment. A new branch of toxicology known as nanotoxicology has arisen to address the adverse health effects caused by nanomaterials.[112] Humans have always been exposed to various tiny particles via dust storms, volcanic ash and other natural processes, and our bodily systems are well adapted to protect us from these potentially harmful intruders. The reticuloendothelial system actively neutralizes and eliminates foreign matter in the body, including both biological and non-biological particles. But the explosive growth of science and technology has changed the character of pollution, increasing the proportion of nanometer-sized materials of variety of chemical compositions. There is heightened concern about the development of nanotechnology. It is indisputable that engineered nanomaterials can be a source of pollution when not safely manufactured, handled and disposed or recycled. The current knowledge of the toxicology of "bulk" materials may not suffice in reliably predicting toxic forms of nanomaterials. Adverse effects of nanomaterials on human health depend on both individual factors such as genetics and existing disease, as well as nanomaterials chemistry, size, shape, agglomeration state and electromagnetic properties. A rational science-based approach is necessary to understand and minimize harm caused by these materials, while supporting continued study and appropriate industrial development. Studies on animal and human show that inhaled nanomaterials are less efficiently removed by the macrophage clearance mechanisms in the lungs than larger particles, causing lung damage.[112] Nanomaterials can also translocate through the circulatory, lymphatic and nervous systems to many tissues

and organs, including the brain. The key to understanding the toxicity of nanomaterials is that their minute size allows them to penetrate through cells and cellular organelles and they can influence basic cellular processes, such as proliferation, metabolism and death. These tiny intruders can cause tissue

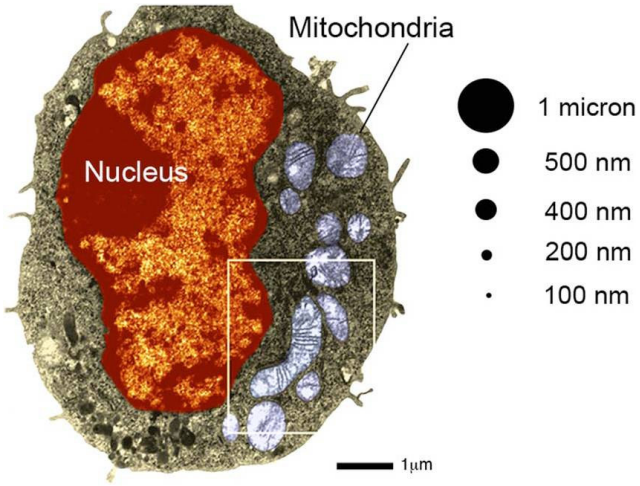

Figure 1.17: Comparison of rat macrophage cells size to nanoparticles size. Human macrophages are up to two times larger than rat macrophages (adopted from reference 112).

inflammation and alter cellular redox balance toward oxidation, causing abnormal function or cell death. Figure 1.17 illustrates the size of a cell and its organelles compared to nanoparticles of different sizes, to show why nanoparticles are able to enter cells and interact with various cell components such as nucleus, mitochondria, etc.

Toxic effect of nanomaterials on human and animal can be significantly reduced through identifying creation-exposure pathways of toxins. A large body of research is required to study nanomaterials toxicity, comprising epidemiological, animal and human cell culture studies. Exposure monitoring and control strategies are necessary for workers in nanotechnology related industries to avoid exposure to materials with new sizes, shapes and physicochemical properties. Again the

misapprehension of nanotoxicity may create a general fear that all nanomaterials are toxic. Many synthetic nanomaterials produce positive health effects, for example, functionalized fullerene chemicals that act as antioxidants. Several types of nanoparticle are known to have an antimicrobial effect, such as silver,[113] titanium dioxide,[114] fullerenes,[115] zinc oxide[116] and magnesium oxide. Few nanostructured materials often exhibit beneficial properties, from UV absorbance in sunscreen to oil-less lubrication of motors. The development of nanotechnology and the study of nanotoxicology should always go hand in hand. The field of nanotechnology and nanoscience has yet to have a significant public health hazard, but it is a real possibility that can and should be prevented.

References

1. T. Vossmeyer, L. Katsikas, M. Giersig, I. G. Popovic and H. Weller, *J. Phys. Chem.,* **98,** *7665*, 1994.

2. G. Binnig and H. Rohrer, *Rev. Mod. Phys*., **59**, *615*, 1987.

3. C. F. Hirjibehedin, C. Y. Lin, A. F. Otte, M. Ternes, C. P. Lutz, B. A. Jones and A. J. Heinrich, *Science,* **317,** *1199,* 2007.

4. C. N. R. Rao, A. Mueller and A. K. Cheetham, *The Chemistry of Nanomaterials*. Wiley-VCH, Weinheim, **1**, 2004.

5. C. N. R. Rao, G. U. Kulkarni, P. J. Thomas and P. P. Edwards*, Chem. Soc. Rev.,* **29***, 27*, 2000.

6. A. P. Alivisatos, *Science,* **271,** *933*, 1996.

7. S. M. Reimann and M. Manninen, *Rev. Mod. Phys.*, **74,** *1284*, 2002.

8. S. Link and M. A. El-Sayed, *Int. Rev. Phy. Chem*., **19**, *409,* 2000.

9. S. Link and M. A. El-Sayed*, J. Phys. Chem. B*, **105**, *1,* 2001.

10. P. Mulvaney, *Langmuir,* **12**, *788,* 1996.

11. G. C. Papavassilliou, *Prog. Solid State Chem.,* **12**, *185,* 1980.

12. G. Mie, *Ann. Phys.* **25**, *377*, 1908.

13. L. E. Brus, *J. Chem. Phys.,* **79,** *5566,* 1983.

14. L. E. Brus, *J. Chem. Phys.,* **80,** *4403,* 1984.

15. L. Liu, Q. Peng and Y. Li, *Inorg. Chem.,* **47**, *5022*, 2008.

16. T. Trindade, P. O. Brien and N. L. Pickett, *Chem. Mater.,* **13,** *3843,* 2001.

17. A. J. Sutherland, *Curr. Opin. Solid State Mater. Sci.,* **6**, *365,* 2002.

18. M. Bruchez, J. M. Moronne and P. Gin, *Science,* **281,** *2013,* 1998.

19. X. Peng, J. Wickham and A. P. Alivisatos, *J. Am. Chem. Soc.,* **120**, *5343*, 1998.

20. Q. A. Pankhurst and R. J. Pollard, *J. Phys. Condens. Matter,* **5**, *8487*, 1993.

21. A. Sundaresan, R. Bhargavi, N. Rangarajan, U. Siddesh and C. N. R. Rao, *Phys. Rev. B* **74**, *161306 (R),* 2006.

22. M. Sastry, A. Gole and V. Patil. *Thin Solid Films*, **384**, *125*, 2001.

23. S. H Tolbert and A. P Alivisatos, *Science* **265**, *373*, 1994.

24. G. C. Bond, *Catal. Today* **72**, *5,* 2002.

25. R. Grisel, K. J. Weststrate, A. Gluhoi and B. E. Nieuwenhuys, *Gold Bull.* **35**, *39,* 2002.

26. M. Haruta, *Catal. Today,* 36, *153*, 1997.

27. A. Mews, A. Eychmuller, M. Giersig, D. Schooss and H. Weller, *J. Phys. Chem.,* **98,** *934,* 1994

28. G. U. Kulkarni, P. J. Thomas and C. N. R. Rao, *The Chemistry of Nanomaterials*, Wiley-VCH, Weinheim, **2**, 2004.

29. J. Park, J. Joo, S. G. Kwon, Y. Jang and T. Hyeon, *Angew. Chem. Int. Ed.,* **46,** *4630*, 2007.

30. C. Burda, X. Chen, R. Narayanan and M. A. El-Sayed, *Chem. Rev*., **105**, *1025*, 2005.

31. S. Iijima, *Nature,* **354**, *56*, 1991.

32. D. S. Bethune, C. H. Klang, M. S. D. Vries, G. Gorman, R. Savoy, J. Vazquez and R. Beyers, *Nature*, **363**, *605*, 1993.

33. W. A. D. Heer, *Nature Mater.*, **1**, *153*, 2002.

34. A. Srivastava, O. N. Srivastava, S. Talapatra, R. Vajtai and P. M. Ajayan, *Nature Mater.,* **3,** *610*, 2004.

35. G. Cao, *Nanostructures and Nanomaterials: Synthesis, Properties and Applications*, Imperial College Press, 2003.

36. G. W. Sears, *Acta Metal.,* **3,** *361*, 1955.

37. G. W. Sears, *Acta Metal.,* **3,** *367,* 1955.

38. Z. W. Pan, Z. R. Dai and Z. L. Wang, *Science,* **291**, *1947* 2001.

39. X. Y. Kong and Z. L. Wang, *Nano Lett.,* **3**, *1625*, 2003.

40. X. Jiang, T. Herricks and Y. Xia, *Nano Lett.,* **2**, *1333*, 2002.

41. P. Yang and C. M. Lieber, *Science*, **273,** *1836*, 1996.

42. W. Shi, H. Peng, Y. Zheng, N. Wang, N. Shang, Z. Pan, C. Lee and S. Lee, *Adv. Mater.,* **12,** *1343*, 2000.

43. B. Gates, Y. Yin and Y. Xia, *J Am. Chem. Soc.,* **122,** *12582*, 2000.

44. B. Mayers, B. Gates,Y. Yin and Y. Xia, *Adv. Muter.,* **13,** *1380*, 2001.

45. Y. Li, Y. Ding and Z. Wang, *Adv. Mater.,* **11**, *847,* 1999.

46. W. Wang, C. Xu, G. Wang, Y. Liu and C. Zheng, *Adv. Mater.,* **14***, 837,* 2002.

48. J. J. Urban, W.S. Yun, Q. Gu and H. Park, *J. Am. Chem. Soc.,* **124,** *1186*, 2002

49. Q. Chen, W. Zhou, G. Du and L. M. Peng, *Adv. Mater.,* **14,** *1208,* 2002.

50. Y. Sun, B. Gates, B. Mayers and Y. Xia, *Nano Lett.,* **2,** *165,* 2002.

51. J. Hu, T. W. Odom, and C. M. Lieber, *Acc. Chem. Res.,* **32,** *435*, 1999.

52. A. M. Morales and C. M. Lieber, *Science*, **279**, *208* 1998.

53. X. Duan and C. M. Lieber, *Adv. Mater.,* **12**, *298*, 2000.

54. T. J. Trentler, K. M. Hickman, S. C. Goel, A. M. Viano, P. C. Gobbons, and W. E. Buhro, *Science*, **270**, *1791* 1995.

56. W. E. Buhro, *Polyhedron,* **13**, *1131* 1994.

57. H. Yu and W. E. Buhro, *Adv. Mater.,* **15**, *416*, 2003.

58. J. Franks, *Acta Metal.,* **6**, *103*, 1958.

59. J. D. Eshelby, *Phys. Rev.,* **91**, *775* 1953.

60. R. Inguanta, S. Piazza and C. Sunseri, *Nanotechnology*, **18**, *485605*, 2007.

61. Y. Wang and G. Cao, *J. Mater. Chem.*, **17**, *894*, 2007.

62. Z. Zhang, D. Gekhtman, M. S. Dresselhaus, and J. Y. Ying, *Chem. Mater*., **11,** *1659*, 1999.

63. E. G. Wolfe and T. D. Coskren, *J. Am. Ceram. Soc.,* **48**, *279* 1965.

64. X. Duan and C. M. Lieber, *Adv. Mater*., **12**, *298,* 2000.

65. T. Wen, J. Zhang, T. P. Chou, and G. Z. Cao, *J. Sol-Gel Sci. Technol.,* **33**, *193*, 2005.

66. H. Fong, W. Liu, C. S. Wang, and R. A. Vaia, *Polymer*, **43,** *775*, 2002.

67. J. A. Mathews, G. E. Wnek, D. G. Simpson, and G. L. Bowlin, *Biomacromolecules*, **3**, *232*, 2002.

68. K. V. Klitzing, G. Dorda, and M. Pepper, *Phys. Rev. Lett.,* **33**, *827*, 1980.

69. D. Tsui, and H. Stormer, *IEEE J. Quantum Electron.,* **22**, *1711*, 1986.

70. M. N. Baibich, J. M. Broto, A. Fert, F. Nguyen V. Dau, F. Petroff, P. Etienne, G. Creuzet, A. Friederich and J. Chazelas, *Phys. Rev. Lett.,* **61**, *2472*, 1988.

71. G. Binasch, P. Grunberg, F. Saurenbach and W. Zinn, *Phys. Rev. B*, **39**, *4828*, 1989.

72. M. Abe, T. Mimura, K. Nishiuchi, A. Shibatomi and M. Kobayashi *IEEE J. Quantum Electron.,* **22**, *1870*, 1986.

73. J. Faist, F. Capasso, D. L. Sivco, C. Sirtori, A. L. Hutchinson, and A. Y. Cho, *Science,* **264,** *553,* 1994.

74. B. Dieny, V. S. Speriosu, S. S. P. Parkin, B. A. Gurney, D. R. Wilhoit and D. Mauri, *Phys. Rev. B,* **43,** *1297,* 1991.

75. U. K. Gautam, S. R. C. Vivekchand, A. Govindaraj and C. N. R. Rao, *Chem. Commun., 3995*, 2005.

76. Y. Wu, B. Yang, B. Zong, H. Sun, Z. Shen and Y. Feng, *J. Mater. Chem.,* **14**, *469*, 2004.

77. R. Vendamme, S. Onoue, A. Nakao and T. Kunitake, *Nat. Mater.*, **5**, *494*, 2006.

78. H. Watanabe and T. Kunitake, *Adv. Mater.,* **19**, *909*, 2007.

79. C. N. R. Rao, G. U. Kulkarni, V. V. Agrawal, U. K. Gautam, M. Ghosh and U. Tumkurkar, *J. Colloid Interface Sci.*, **289**, *305*, 2005.

80. C. N. R. Rao, G. U. Kulkarni, P. J. Thomas, V. V. Agarwal and P. Saravanan, *Curr. Sci.*, **85**, *1041*, 2003.

81. Y. Lin, H. Skaff, T. Emrick, A.D. Dinsmore and T. P. Russell, *Science*, **299**, *226*, 2003.

82. C. N. R. Rao, G. U. Kulkarni, P. J. Thomas, V. V. Agarwal and P. Saravanan, *J. Phys. Chem. B*, **107**, *7391*, 2003.

83. V. V. Agrawal, G. U. Kulkarni and C. N. R. Rao, *J. Phys. Chem. B*, **109**, *7300*, 2005.

84. V. V. Agrawal, P. Mahalakshmi, G. U. Kulkarni and C. N. R. Rao, *Langmuir*, **22**, *1846*, 2006.

85. U. K. Gautam, M. Ghosh and C. N. R. Rao, *Chem. Phys. Lett.*, **381**, *1*, 2003.

86. U. K. Gautam, M. Ghosh and C. N. R. Rao, *Langmuir*, **20**, *10775*, 2004.

87. K. P. Kalyanikutty, U. K. Gautam and C. N. R. Rao, *Solid State Sci.*, **8**, *296*, 2006.

88. K. P. Kalyanikutty, U. K. Gautam and C. N. R. Rao, *J. Nanosci. Nanotechnol.*, **7**, *1916*, 2007.

89. K. S. Nonoselov, A. K. Geim, S. V. Morozov, D. Jiang, Y. Zhang, S. V. Dubonos, I. V. Grigorieva and A. A. Firsov, *Science*, **306**, *666*, 2004.

90. A. K. Geim and K. S. Novoselov, *Nat. Mater.*, **6**, *183*, 2007.

91. A. H. C. Neto, F. Guinea, N. M. R. Peres, K. S. Novoselov, and A. K. Geim, *Rev. Mod. Phys.*, **81**, *109*, 2009.

92. M. I. Katsnelson, *Mater. Today*, **10**, *20*, 2007.

93. C. Berger, Z. Song, X. Li, X. Wu, N. Brown, C. Naud, D. Mayou, T. Li, J. Hass, A. N. Marchenkov, E. H. Conrad, P. N. First and W. A. D. Heer, *Science*, **312**, *1191*, 2006.

94. M. Y. Han, B. Ozyilmaz, Y. Zhang and P. Kim, *Phys. Rev. Lett.*, **98**, *206805*, 2007.

95. F. Schedin, A. K. Geim, S. V. Morozov, E. W. Hill, P. Blake, M. I. Katnelson and K. S. Novoselov, *Nat. Mater.*, **6**, *652*, 2007.

96. B. Huard, J. A. Sulpizio, N. Stander, K. Todd, B. Yang and D. G. Gordon, *Phys. Rev. Lett.*, **98**, *236803*, 2007.

97. C. N. R. Rao, K. Biswas, K. S. Subrahmanyam and A. Govindaraj, *J. Mater. Chem.*, **19**, *2457*, 2009.

98. C. N. R. Rao, A. K. Sood, K. S. Subrahmanyam and A. Govindaraj, *Angew. Chem. Int. Ed*, **48**, *7752*, 2009.

99. C. N. R. Rao, A. K. Sood, R. Voggu, and K. S. Subrahmanyam, *J. Phys. Chem. Lett.*, **1**, *572*, 2010.

100. K. S. Subrahmanyam, S. R. C. Vivekchand, A. Govindaraj and C. N. R. Rao, *J. Mater. Chem.,* **18**, *1517*, 2008,

101. S. Park, J. An, I. Jung, R. D. Piner, S. J. An, X. Li, A. Velamakanni and R. S. Ruoff, *Nano Lett.*, **9**, *1593*, 2009.

102. W. Hummers and R. E. Offeman, *J. Am. Chem. Soc*., **80**, *1339*, 1958.

103. H. C. Schniepp, J. L. Li, M. J. Mcallister, H. Sai, M. H. Alonso, D. H. Adamson, R. K. Prudhomme, R. Car, D. A. Saville, and I. A. Aksay, *J. Phys. Chem. B*, **110**, *8535*, 2006.

104. A. Reina, X. Jia, J. Ho, D. Nezich, H. Son, V. Bulovic, M. S. Dresselhaus, and J. Kong, *Nano Lett.*, **9**, *30,* 2009.

105. B. L. V. Prasad, H. Sato, T. Enoki, Y. Hishiyama, Y. Kaburagi, A. M. Rao, P. C. Eklund, K. Oshida and M. Endo, *Phys. Rev. B*, **62**, *11209,* 2000.

106. K. S. Subrahmanyam, L. S. Panchakarla, A. Govindaraj and C. N. R. Rao *J. Phys. Chem. C*, **113,** *4257*, 2009.

107. C. N. R. Rao and K. Biswas, *Annu. Rev. Anal. Chem*., **2**, *435*, 2009.

108. E. N. Kaufmann, *Characterization of Materials*, Hoboken, NJ:Wiley, **2**, 2003.

109. B. Williams and C. B. Carter, *Transmission Electron Microscopy*. New York: Plenum, 1997.

110. J. Goldstein, D. Newbury, D. Joy, C. Lyman and P. Echlin, *Scanning Electron Microscopy and X-Ray Microanalysis*. New York: Springer. 3rd ed, 2003.

111. P. Samori, *Scanning Probe Microscopies Beyond Imagining: anipulation of Molecules and Nanostructures*. Weinheim, Wiley-VCH Verlag, 2006.

112. C. Buzea, I. I. Pacheco and K. Robbie, *Biointerphases,* **2,** *M17,* 2007.

113. A. Panacek, L. Kvıtek, R. Prucek, M. Kolar, R. Vecerova, N. Pizurova, V. K. Sharma, T. Nevecna and R. Zboril, *J. Phys. Chem. B*, **110**, *16248*, 2006.

114. Y. Li, P. Leung, L. Yao, Q. W. Song and E. Newton, J. Hosp. *Infect*. **62**, *58*, 2006.

115. S. Bosi, T. D. Ros, G. Spalluto and M. Prato, *Eur. J. Med. Chem*. **38**, *913*, 2003.

116. R. Brayner, R. F. Iliou, N. Brivois, S. Djediat, M. F. Benedetti and F. Fievet, *Nano Lett*. **6**, *866*, 2006.

CHAPTER 2

Transformation of elemental nanowires to nanotubes of metal oxides and chalcogenides through Kirkendall effect*

Summary

This chapter deals with the transformation of elemental nanowires of metals and silicon to nanotubes of the corresponding oxides and chalcogenides through Kirkendall effect. The metal nanowires were prepared by nebulized spray pyrolysis of metal acetates in an inert atmosphere and silicon nanowires by carbon-assisted synthesis. The formation of ZnO nanotubes by the oxidation of Zn nanowires has been studied as a function of time observing the intermediate structures during the oxidation. Nucleation of Kirkendall voids in the nanowires during the oxidation leads to the formation of the ZnO nanotubes. The kinetics of the Zn nanowire-ZnO nanotube transformation has been studied and the activation energy for the transformation found to be 12.2 kcal/mol. $ZnCr_2O_4$ nanotubes are formed by the reaction of Zn nanowires with CrO_2Cl_2 in an oxygen atmosphere. We have obtained nanotubes of Co_3O_4, starting

---

*A paper based on this work has been published in *J. Phys. Chem. C* (**2008**).

from Co nanowires and SiO_2 (cristobalite) nanotubes starting from Si nanowires. Nanotubes of ZnS, CdS and CdSe have been obtained by the reaction of the metal nanowires with the chalcogens. The activation energy for the formation of CdS nanotubes from Cd nanowires is found to be 8.5 kcal/mol. The present study establishes Kirkendall effect as a novel means of preparing nanotube structures of several inorganic materials.

2.1 Introduction

Kirkendall effect is a classical phenomenon which refers to a nonreciprocal mutual diffusion process through an interface of two metals so that vacancy diffusion occurs to compensate for the inequality of the material flow.[1–5] This phenomenon was observed and established more than half a century ago.[1,2] In 1942, Kirkendall performed an experiment on copper and brass in order to understand the solid state diffusion process in metals and alloys.[1] A couple of copper and brass was welded together with an inert marker placed at the welded junction and subjected to elevated temperature. If the diffusivities of copper and zinc are same and there is no change in volume during diffusion or reaction, the marker should not move and stay at the original position. But they observed a movement of the initial interface towards brass concluding that the rate of diffusion of zinc is much greater than that of copper in alpha brass. When zinc diffuses away, the corresponding vacant sites are not occupied by the opposite flow of Cu and therefore, vacant sites are left unoccupied. In other words, there is a flow of vacancies opposite to the faster diffusing Zn (intrinsic diffusivity of Zn being ≈ 2.5 times that of Cu at 1058 K) to compensate for the difference between the Zn and Cu flux. This result was confirmed in a repeated experiment in 1947[2] by Kirkendall and Smigelskas. A schematic of Kirkendall effect is shown in Figure 2.1. These experiments established that atomic diffusion occurs through vacancy exchange, not by the direct interchange of atoms. Initially, this work was highly criticized but later this phenomenon was confirmed from experiments on many other systems.[6]

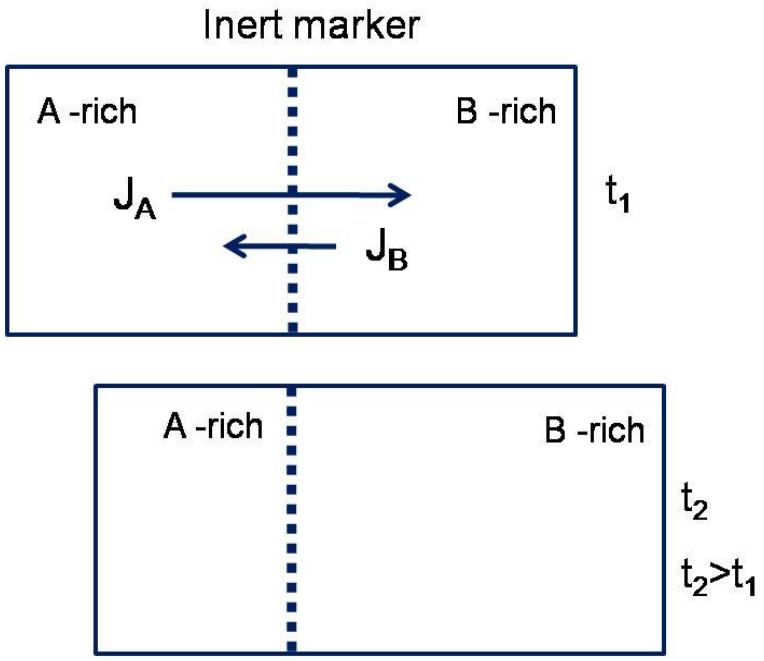

Figure 2.1: Schematic of Kirkendall effect. A diffusion couple of A and B was welded together, with an inert marker placed at the welded junction. The diffusion rates of the two species are different ($|J_A| > |J_B|$). Since the diffusion fluxes are different, there will be a net flow of matter past the inert marker, causing the couple to shift bodily with respect to the marker.

Kirkendall effect type directional material flows can also result from coupled reaction-diffusion phenomena at solid/gas or solid/liquid interfaces during the growth of metal oxide or sulfide films.[7,8] This directional flow of matter is balanced by an opposite flow of vacancies which can then condense into pores or annihilate at dislocations leading to void formation. Usually, outward transport of fast-moving cations through the oxide or sulfide layer and a balancing inward flow of vacancies to the vicinity of the metal-oxide/sulfide interface yield voids. These voids are known as Kirkendall voids.

The interface motion and pore formation due to Kirkendall effect have been widely studied in the past because of their impact on the reproducibility and reliability of solders, passivation layers, diffusion barriers, etc. Formation of the Kirkendall voids also deteriorates the bonding strength of the bond–pad interface and causes wire bond failure in integrated circuits.[9,10] There are several efforts to avoid this effect by introducing diffusion barrier layers, for example, Ta as a diffusion barrier between Cu and bronze in the multifilamentary superconducting composite.[11] Kirkendall effect was not used as a method of preparing porous materials. The pores produced at metal-metal diffusion couple or near the metal-oxide/sulfide interface do not yield monodisperse homogenous ordered arrays, but instead form a very heterogeneous ensemble.[12] The volume fraction of pores formed by this method is also much smaller to find some useful applications.

After more than sixty years, Kirkendall effect received scientific attention once again when chemists used this destructive effect in a constructive way for the fabrication of hollow nanostructures. In 2004, Alivisatos and his co-workers have demonstrated that this effect can be an interesting synthesis route to nanoscale hollow structures of various materials.[12] When nanostructure of a fast-diffusing species reacts with a slower-diffusing species, large number of vacancies are created because of the high surface to volume ratio and the absence of defects at the core. Inside the small volume of the growing nanostructure, the vacancies coalesce into large voids giving rise to products which are hollow as explained in the schematic of Figure 2.2. Synthesis of hollow nanostructures employing the Kirkendall effect would have several advantages.[5]

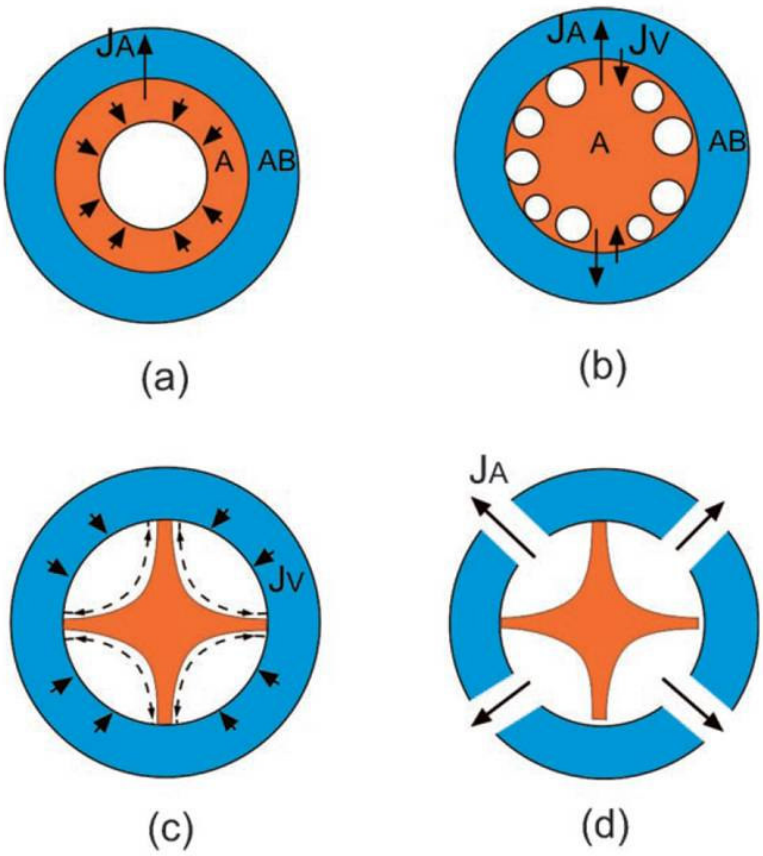

Figure 2.2: Schematic to show the growth of hollow nanostructures induced by the Kirkendall effect (adopted from reference 5). A stands for the core component and AB for the product phase. (a) A continuous bulk diffusion of core and shell components through a continuous A/AB interface and condensation of excess vacancies at the center of the core. (b) At an early stage, small Kirkendall voids are generated via bulk diffusion at the interface. c) In a later stage, when the voids contact the inner surface of the product layer, the enlargement of the hollow core could be contributed by surface diffusion of atoms of the core material along the skeletal bridges. (d) If gaps are present in the shell layer, or appear during the growth, the material exchange can proceed via direct dissolution (in solution phase) or evaporation (in gas phase) through the gaps, leading to hollowing of the NPs.

2.2 Scope of the present investigations

Nanotubes are nanomaterials of great importance due to their novel properties and potential applications in diverse areas as high-efficiency catalysts, drug delivery systems, nanoelectronics, nano-optics, light weight structural materials and energy storage and conversion.[13,14] Compared to nanowires, nanotubes provide access to three different contact regions: the inner surface, the outer surface and the tube ends. Several methods of synthesizing carbon as well as inorganic nanotubes have been described in the literature.[13,14] Typical of the synthetic methods are template-assisted growth, arc discharge, laser ablation, chemical vapour deposition, plasma enhanced vaporization and hydrothermal or solvothermal processes. Hollow nanostructures can also be created by making use of the Kirkendall effect. Hollow spherical nanostructures of cobalt oxides, sulphides and selenides have been obtained by making use of the Kirkendall effect.[12] Nanotubes of Ag_2Se have been prepared by UV photodissociation of CSe_2 adsorbed on the surface of Ag nanowires.[15] While Ga doped ZnS nanowires have been converted into ZnO-$ZnGa_2O_4$ composite nanotubes,[16] $ZnAl_2O_4$ nanotubes were obtained by the interfacial solid state reaction of core-shell ZnO-Al_2O_3 nanowires.[17] Formation of Co_3S_4 nanotubes starting from 1D $Co(CO_3)_{0.35}Cl_{0.20}(OH)_{1.10}$ nanowires appear to involve Kirkendall effect.[18] In spite of these literature reports, there is no detailed investigation of the structures as well as the formation kinetics of 1D hollow nanostructure of oxides and other materials formed by the transformations of metallic or elemental nanowires through Kirkendall effect. We have, therefore, carried out a systematic study of the formation of ZnO nanotubes from Zn nanowires by employing X-ray diffraction and electron microscopy, paying attention to the process of

transformation. $ZnCr_2O_4$ nanotubes have been formed by the reaction of Zn nanowires with CrO_2Cl_2. We have obtained nanotubes of Co_3O_4, ZnS, CdS and CdSe starting with the corresponding metallic nanowires, besides SiO_2 (cristobalite) nanotubes starting from Si nanowires. Kinetics of formation of the CdS nanotubes from Cd nanowires has also been examined.

2.3 Experimental and related aspects

2.3.1 Synthesis of metal nanowires

Nanowires of Zn, Co and Cd were synthesized by the nebulised spray pyrolysis of methanolic solutions of the metal acetates in an inert atmosphere.[19] In a typical experiment, 50 mL methanolic solution of acetate of zinc, cadmium or cobalt was prepared with a concentration of 40 gL^{-1}. The solution was nebulized and the spray carried into a preheated silicon carbide furnace maintained between 1093 and 1123 K using Ar as a carrier gas. Typical flow rates of Ar used was 1000 standared cubic centimetre per minute (sccm). All the experiments were performed using a quartz tube with an inner diameter of 25 mm. The reaction was typically carried out for 1 h. The shiny deposits obtained at the outlet of quartz tube was characterized to be metal nanowires and used for the further experiments.

2.3.2 Synthesis of silicon nanowires

Si nanowires were obtained by heating an intimate mixture of silicon powder and activated charcoal in nitrogen environment.[20] In a typical experiment, silicon powder was finely ground with activated charcoal keeping the weight ratio of Si to C at 1:3 and the mixture was heated at 1473 K for 3 h in N_2 atmosphere. The grey colour powder

obtained as the final product was identified as Si nanowires and used for further experiments.

2.3.3 Synthesis of oxides nanotubes

The Zn nanowires were heated at around 703 K for 4 h in air to transform them to ZnO nanotubes. The progress of the reaction was followed by recording electron microscopy images as well as X-ray diffraction patterns at intermediate stages of the transformation. The kinetic data were obtained by recording X-ray diffraction patterns at different stages of the conversion in the 653-703 K range. We have carried out the reaction of Zn nanowires with CrO_2Cl_2 at 673 K for 3h to obtain $ZnCr_2O_4$ nanotubes. CrO_2Cl_2 was produced in a gas trap by adding a mixture of KCl and $K_2Cr_2O_7$ to concentrated H_2SO_4. In a typical experiment, a mixture of 1 g KCl and 1 g $K_2Cr_2O_7$ was added to 25 mL of conc H_2SO_4. Oxygen gas was passed through the trap to carry the CrO_2Cl_2 vapour towards the Zn nanowires placed in a tube furnace. In order to prepare Co_3O_4 nanotubes, Co nanowires were heated in air at 773 K for 5 h. The intermediate structures during Co_3O_4 nanotubes formation was examined at 723 K/5 h. To prepare SiO_2 nanotubes, oxidation of Si nanowires was carried out at 1598 K for 5 h in air.

2.3.4 Synthesis of chalcogenides nanotubes

Zn nanowires (30 mg) were mixed thoroughly with sulphur powder (150 mg) and the mixture was heated in an Ar atmosphere at 773 K for 3 h to obtain ZnS nanotubes. CdS nanotubes were synthesised by heating a finely ground mixture of Cd nanowires and sulphur powder (1:9 molar ratio) at 773 K for 3 h in an Ar atmosphere. The kinetics of the reaction was studied by recording XRD patterns at different time intervals. CdSe

nanotubes were obtained by heating a mixture of Cd nanowires and selenium powder (1:5 molar ratio) at 673 K for 3 h in an Ar atmosphere.

2.3.5 Characterization techniques

X-Ray diffraction (XRD): XRD patterns were recorded at 298 K with a Rich-Siefert 3000-TT diffractometer employing Cu Kα radiation.

Electron Microscopy: Field emission scanning electron microscopy (FESEM) and scanning tunnelling electron microscopy (STEM) images were recorded with a field emission scanning electron microscope (FESEM, FEI Nova-Nano SEM-600, Netherlands). TEM images were recorded with a JEOL JEM 3010 instrument (Japan) operated at an accelerating voltage of 300 kV.

2.4 Results and discussion

2.4.1 Zn nanowires to ZnO nanotubes

A low-magnification FESEM image of Zn nanowires obtained by nebulized spray pyrolysis of a methanolic solution of zinc acetate is shown in Figure 2.3 (a). The nanowires with zigzag morphology have lengths of several tens of micrometers. The higher magnification FESEM image in Figure 2.3 (b), shows that the nanowires have a smooth surface with an average diameter of 50 nm. The TEM image in Figure 2.3 (c), along with the selected area electron diffraction (SAED) pattern shown as an inset, confirms the nanowires to be single crystalline. The X-ray diffraction (XRD) pattern of the nanowires is shown in Figure 2.3 (d). The XRD pattern confirms the formation of pure phase of the hexagonal zinc (JCPDS card: No. 04-0831, a = 2.67 Å and b = 4.95 Å).

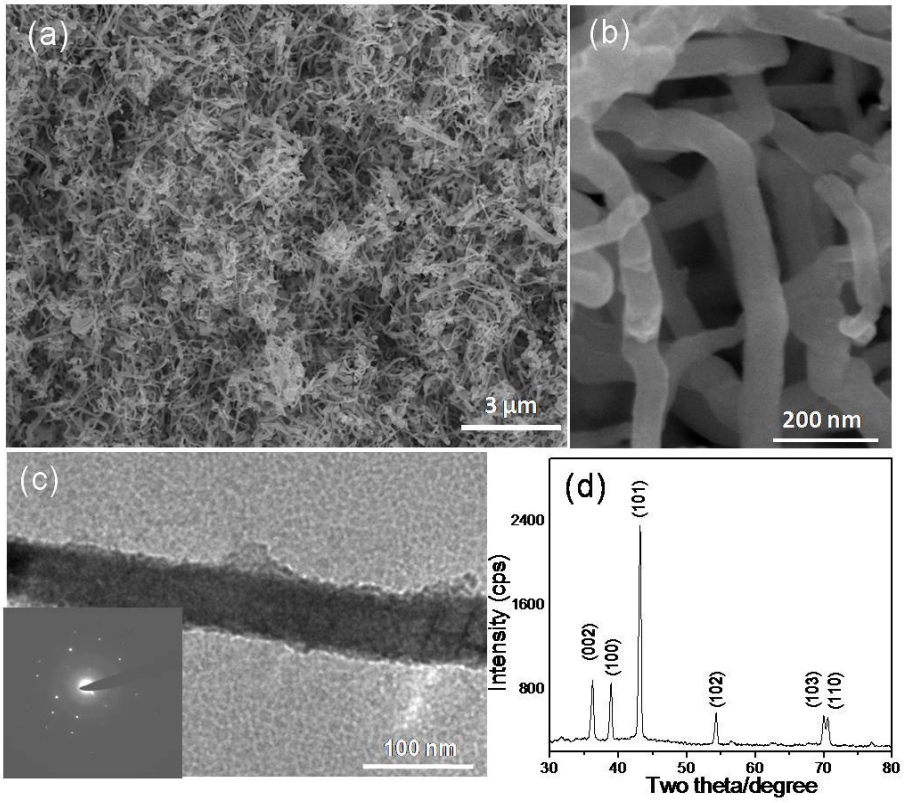

Figure 2.3: (a) Low-magnification and (b) higher-magnification FESEM images of Zn nanowires, (c) TEM image of a Zn nanowire (the inset is the SAED pattern) and (d) XRD pattern of Zn nanowires.

Thermal oxidation of Zn nanowires in air in the temperature range 653 - 703 K for 2 – 4 hours was found to yield ZnO nanotubes. The tubular structure of ZnO nanotubes is clearly seen in the FESEM image (Figure 2.4 (a)). The outer diameters of the nanotubes go up to 90 nm with lengths varying from 400 nm to few microns. The TEM image of a ZnO nanotube shown in Figure 2.4 (b) demonstrates the wall thickness to be around 20 nm. Thus, the inner diameter of the nanotubes works out to be close to the diameter of the starting metal nanowires. The SAED pattern of the ZnO nanotube (Figure 2.4 (c)) shows ring patterns with prominent Bragg spots. The XRD pattern

shown in Figure 2.4 (d) could be indexed for the hexagonal unit cell of ZnO (JCPDS card: No. 36-14151, $P6_3mc$, a = 5.25 Å and c = 5.21 Å).

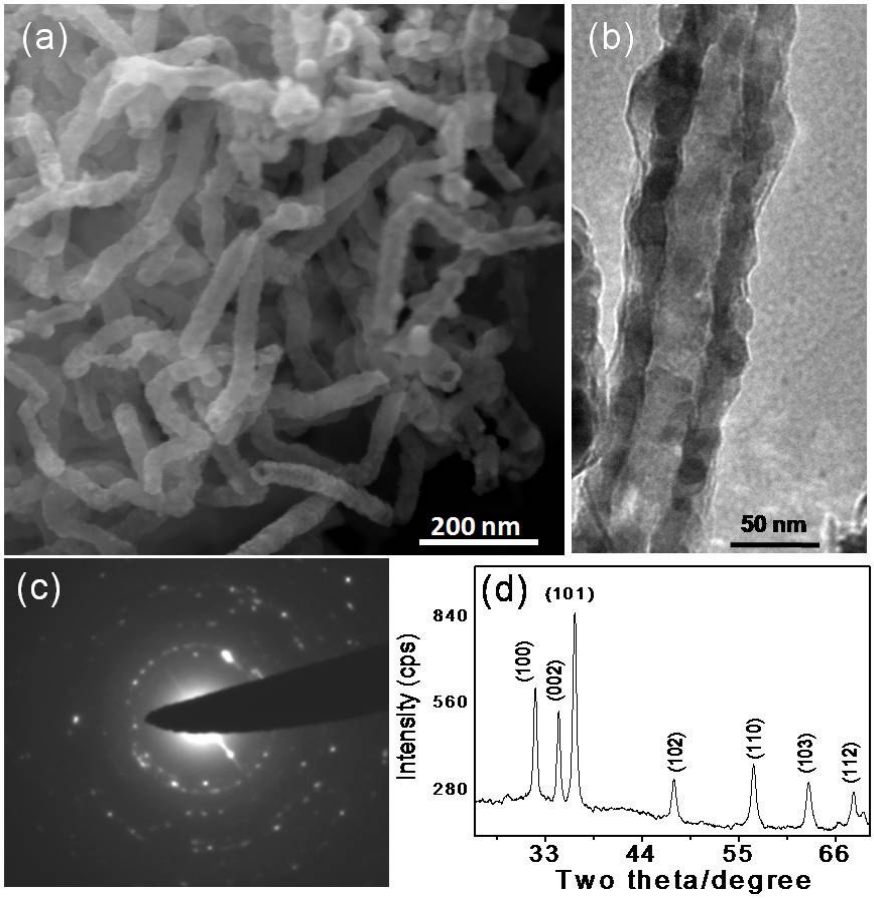

Figure 2.4: (a) FESEM image of ZnO nanotubes, (b) TEM image of a ZnO nanotube, (c) SAED pattern of ZnO nanotubes and (d) XRD pattern of ZnO nanotubes.

The formation of ZnO nanotubes by the oxidation of Zn nanowires was studied as a function of time, observing the intermediate structures during the oxidation of the metal nanowires. A FESEM image of Zn nanowires after oxidation for 15 min is shown in Figure 2.5 (a). We see the rough surface of the 1D nanostructure compared to the initial smooth surface of Zn nanowires. A TEM image in Figure 2.5 (b) reveals the porous nature of nanostructure. After oxidation for one hour, the surface roughness of

the nanostructure decreases and openings of tube-like structures begin to appear as can be seen from the FESEM image in Figure 2.5 (c). The pores formed after oxidation for

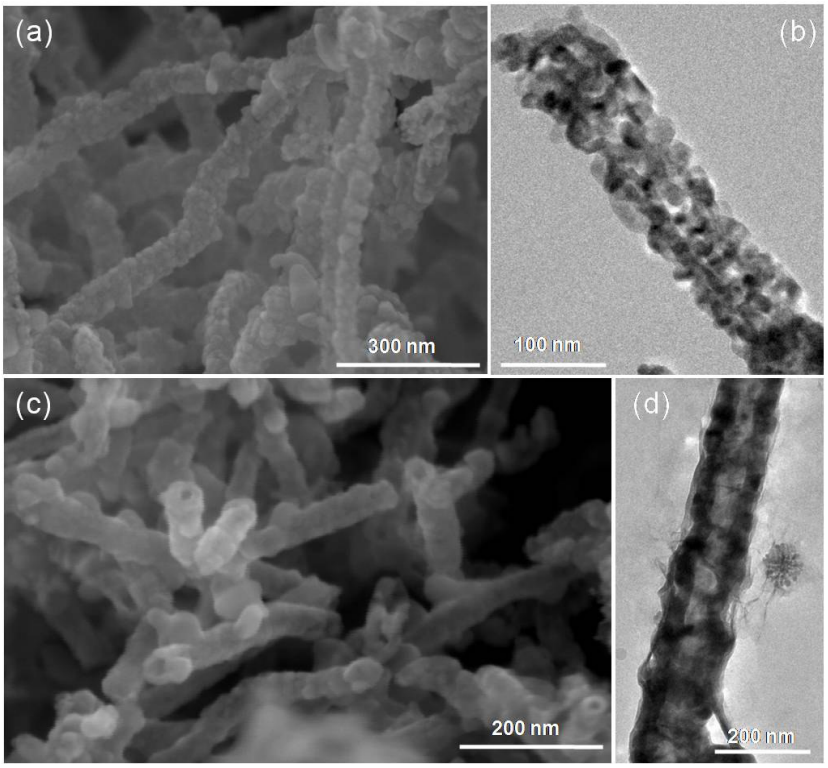

Figure 2.5: (a) FESEM image and (b) TEM image of the nanostructure obtained after oxidation for 15 min, (c) FESEM image and (d) TEM image obtained after 1 h of oxidation.

15 minutes coalesce to form bigger pores resulting in a bamboo type nanotube structure after 1 h, as shown in the TEM image in Figure 2.5 (d). After 4 h of oxidation, well-defined nanotubes of ZnO are formed as shown in Figure 2.4.

The porous nature of the intermediate nanostructures and the polycrystalline nature of the product nanotubes suggest that the conversion of Zn nanowires into ZnO nanotubes involves nano-scale Kirkendall effect.[5,12,15-18, 21] The faster outer diffusion of zinc atoms compared to the slower inner diffusion of the oxygen atoms through the

initially formed ZnO layer is compensated by the opposite flow of vacancies, the vacancies coalesce together to form larger Kirkendall voids. The Kirkendall voids then condense to form bigger holes in the nanostructures, giving rise to bamboo-like morphology. After this stage, it takes another 2 to 3 hours to form perfect tubular nanostructures, since the increasing thickness of the ZnO layer hinders the outer diffusion of Zn atoms.

The kinetics of formation ZnO nanotubes was studied by recording XRD patterns at different time intervals at 653, 673, 683 and 703 K. The reflections correspond to both Zn and ZnO coexist in all the patterns shown in Figure 2.6, but the reflections corresponding to ZnO increase in intensity with time, accompanied by a decrease in the intensity of the reflections due to Zn metal. We have determined the areas under the

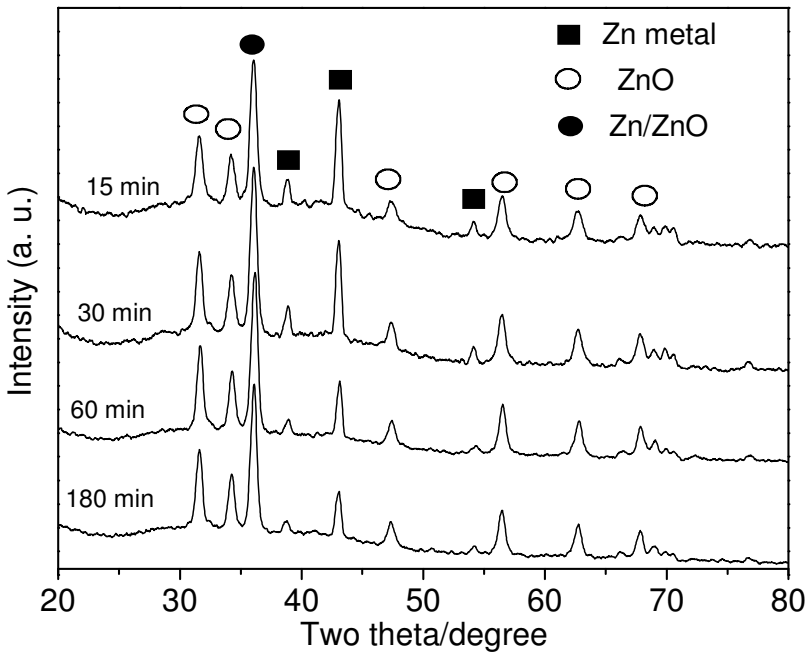

Figure 2.6: XRD patterns recorded at different time intervals of the Zn nanowires-ZnO nanotubes transformation.

(100) reflection of ZnO and the (101) reflection of Zn and plotted the ZnO:Zn ratio of areas against the reaction time in Figure 2.7 (a) (open symbols) at different temperatures. These experimental data could be fitted to the logarithimic rate law.

$$y = k \log (a\,t + 1) + b \qquad (1)$$

where t is time in minutes, k is the rate constant, a and b are temperature-dependant constants and y is the ZnO/Zn ratio. The logarithmic rate law is widely used to explain the oxidation of metals.[21-27] It arises from the mechanism proposed by Caberra and Mott, Grimley and Trapwell, and Eley and Wilkinson, where either cation or anion

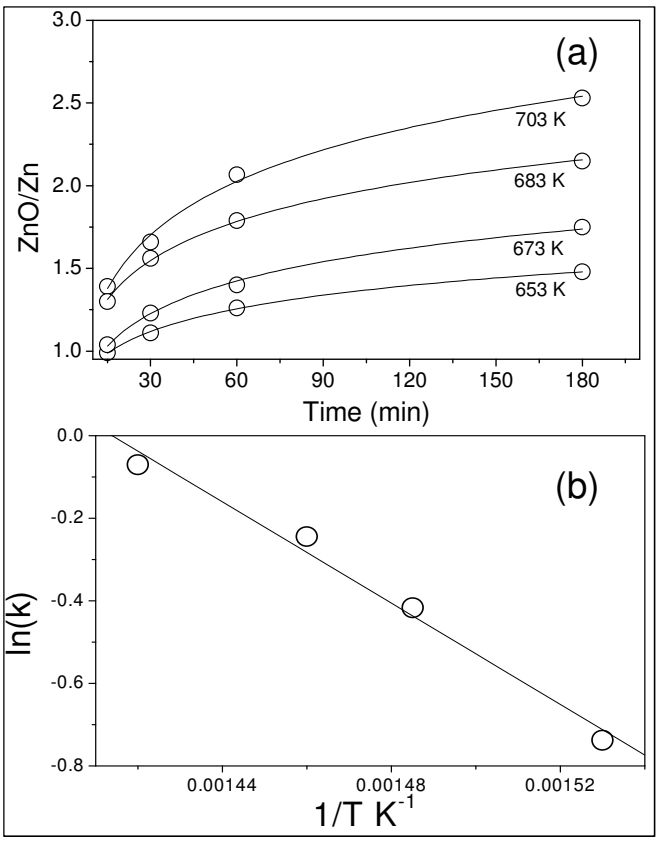

Figure 2.7: (a) Plots of the ratios of areas under ZnO (100) and Zn (101) reflections against reaction time at different temperatures (open symbols). Solid curves represent the logarithimic rate law fit to the experimental data. (b) Arrhenius plot of ln(k) against 1/T.

diffusion limits the rate of oxide growth.[25-29] There is an initial period of rapid oxidation followed by a virtual cessation of the reaction and the formation of a stable film of few nanometers in thickness. The goodness of the fits of the experimental data to Equation (1) can be seen by the solid curves shown in Figure 2.7 (a). From these data we have derived the value of k in Equation (1). A plot of ln(k) against inverse of absolute temperature is given in Figure 2.7 (b). This plot yields activation energy for the nanotube formation to be 12.2 kcal/mol. The activation energy for the oxidation of bulk Zn is reported to be 28.1 kcal/mol.[30,31] Thus oxidation by Kirkendall effect involving diffusion process is associated with lower activation energy as compared to bulk oxidation.

2.4.2 Zn nanowires to $ZnCr_2O_4$ nanotubes

We have obtained nanotubes of $ZnCr_2O_4$ by the reaction of Zn nanowire with CrO_2Cl_2. A low magnification FESEM image of the $ZnCr_2O_4$ nanotubes is shown in Figure 2.8 (a). The nanotubes replicate the zigzag morphology of the starting Zn

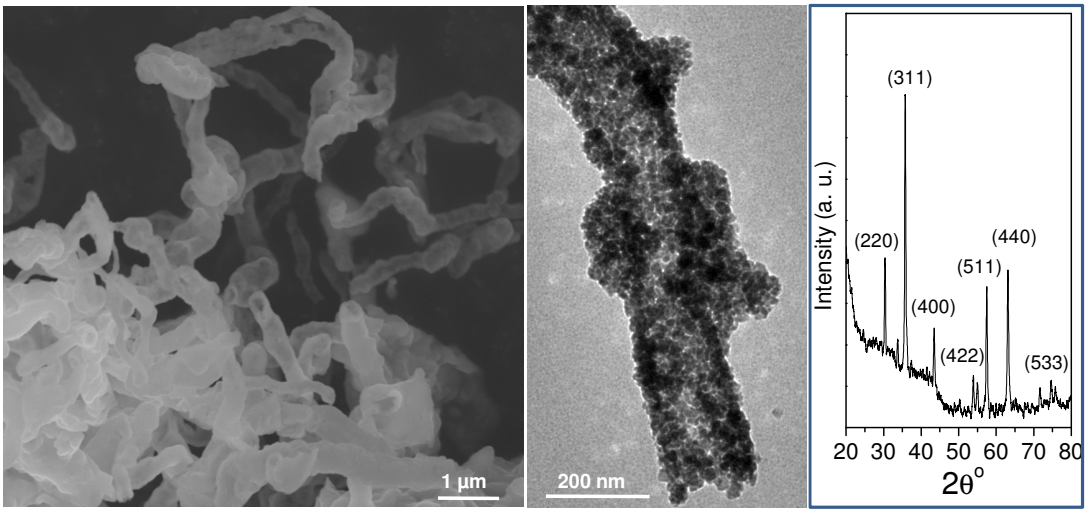

Figure 2.8: (a) FESEM image (b) TEM image and (c) XRD pattern of $ZnCr_2O_4$ nanotubes

nanowires. The nanowires have lengths of several micrometers while the diameter varies between 150 and 500 nm. Open ends of the nanotubes are clearly seen in the FESEM image in Figure 2.8 (a). The TEM image of $ZnCr_2O_4$ nanotube in Figure 2.8 (b) reveals the porous nature of nanotubes. The nanotubes have a granular wall, with a thickness of 20-30 nm. The SAED pattern shows rings, due to the polycrystalline nature of the $ZnCr_2O_4$ nanotubes. The XRD pattern of the nanotubes shown in Figure 2.8 (c) is characteristic of the cubic structure of $ZnCr_2O_4$ (JCPDF card: No. 22-1107, a = 8.32 Å).

2.4.3 Co nanowires to Co_3O_4 nanotubes

Figure 2.9 (a) shows a FESEM image of Co nanowires with a necklaces-like structure obtained by the nebulized spray pyrolysis of a methanolic solution of Co acetate. The nanowires have a narrow diameter distribution (20-25 nm range) with lengths of several micrometers. The TEM image in Figure 2.9 (b) reveals that the nanowires are formed by head to tail fusion of linearly arranged spindle-shaped nanoparticles. A TEM image of a Co_3O_4 nanotube obtained by the thermal oxidation of Co nanowires at 773 K in air is shown in Figure 2.9 (c). The outer diameter of the nanotube is around 40 nm, with a wall thickness of 10 nm. The inner diameter of the nanotube is similar to the diameter of starting Co nanowires indicating that the nanotube is formed by the dominant outer diffusion of cobalt atoms through the initially formed oxide layer on the surface of nanowires. As the starting nanowires have necklace-like morphology, the walls of the product nanotubes are not parallel and there are some humps at the fusion points. The intermediate stage of the Co_3O_4 nanotubes formation was examined by transmission electron microscopy. The TEM image in Figure 2.9 (d) reveals that the Kirkendall holes localized inside the interconnected nanoparticles during

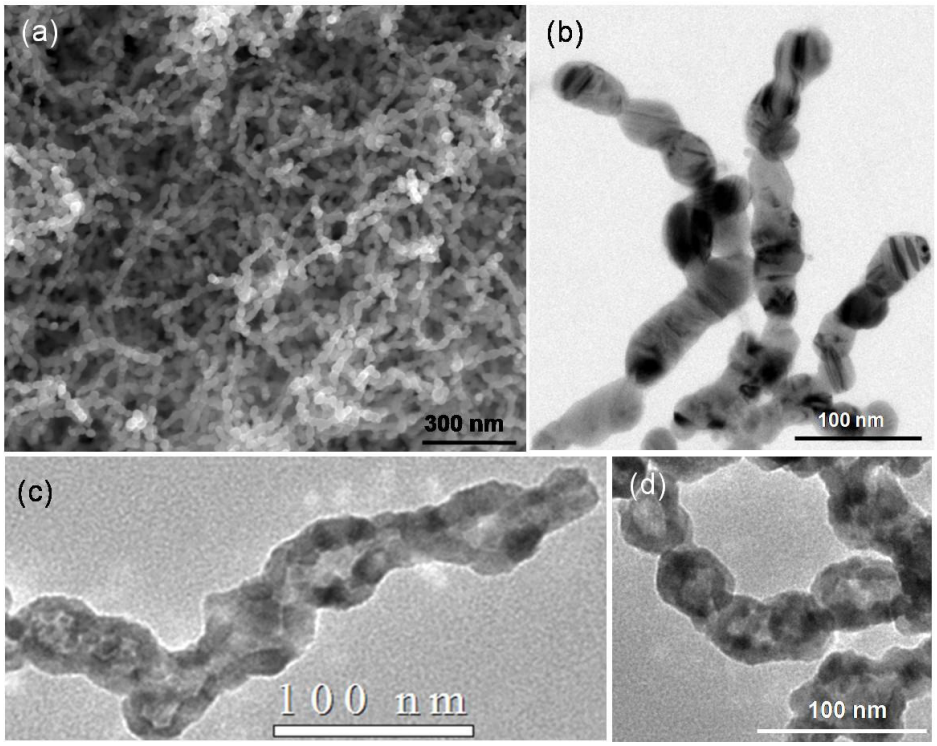

Figure 2.9: (a) FESEM image and (b) TEM image of Co nanowires, (c) TEM image of a Co_3O_4 nanotube, (d) TEM image of the intermediate stage of a Co_3O_4 nanotube formation

intermediate stage of oxidation. When heated at higher temperature the localized holes get interconnected to form the continuous tubular structure.

2.4.4 Si nanowires to SiO_2 nanotubes

In Figure 2.10 (a), we shows a STEM image of Si nanowires obtained by heating an intimate mixture of silicon powder and activated charcoal in a nitrogen environment. The nanowires have diameters ranging from 100 to 400 nm and lengths of several micrometers. The XRD pattern of the nanowires shown in Figure 2.10 (c) matches with that of cubic silicon (JCPDF card: No. 03-0544, a = 5.42 Å). Si nanowires were heated up to 1598 K to obtain nanotubes of SiO_2, shown in the STEM image in Figure 2.10 (b). The diameter of the nanotubes is around 700 nm with wall thickness of around 100 nm.

Figure 2.10 (c) shows the XRD pattern of the nanotubes, the strong intensity of the peaks indicates high crystallinity of the nanotubes. All the peaks could be indexed on the tetragonal SiO_2 structure of cristobalite with the lattice parameters, a = 4.9 Å and c = 6.9 Å (JCPDF card: No. 04-0379). The SiO_2 nanotubes obtained here are unusual in sense that they are crystalline, unlike most silica nanotubes which are amorphous.

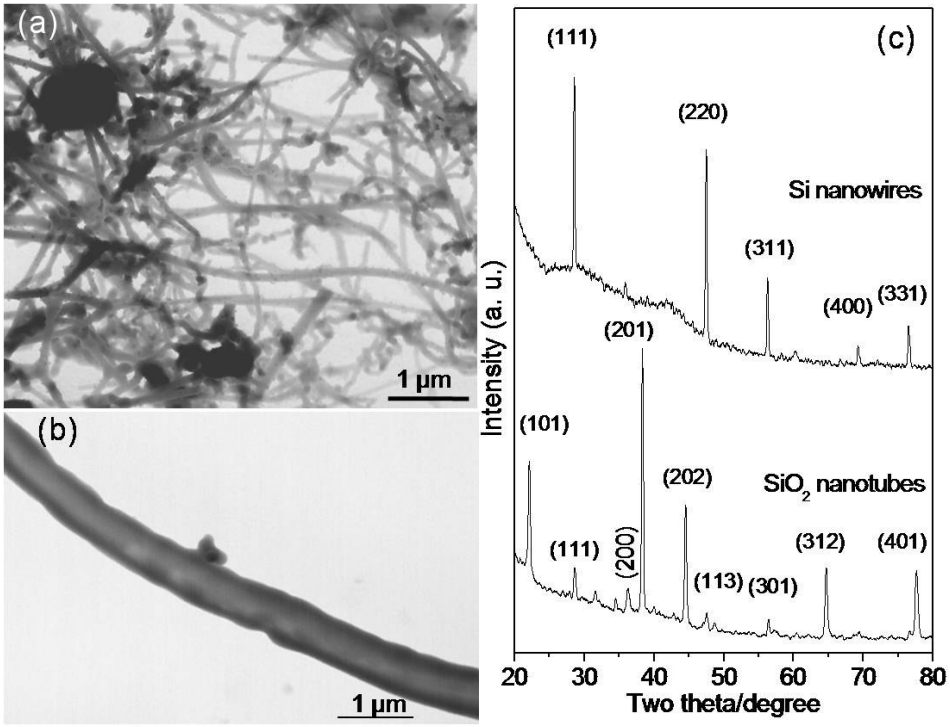

Figure 2.10: STEM image of (a) Si nanowires and (b) SiO_2 nanotube, (c) XRD patterns of Si nanowires and SiO_2 nanotubes.

2.4.5 Zn nanowires to ZnS nanotubes

Reaction of Zn nanowires with sulphur powder yields abundant quantities of ZnS nanotubes. The FESEM image in Figure 2.11 (a), shows that ZnS nanotubes have lengths of few microns with zigzag morphology similar to the starting Zn nanowires. A low magnification TEM image of ZnS nanotubes is shown in Figure 2.11 (b). The outer

diameter of the nanotubes is around 100 nm with wall thickness of 20-25 nm. The SAED pattern of the ZnS nanotubes in Figure 2.11 (c) shows ring patterns. The three

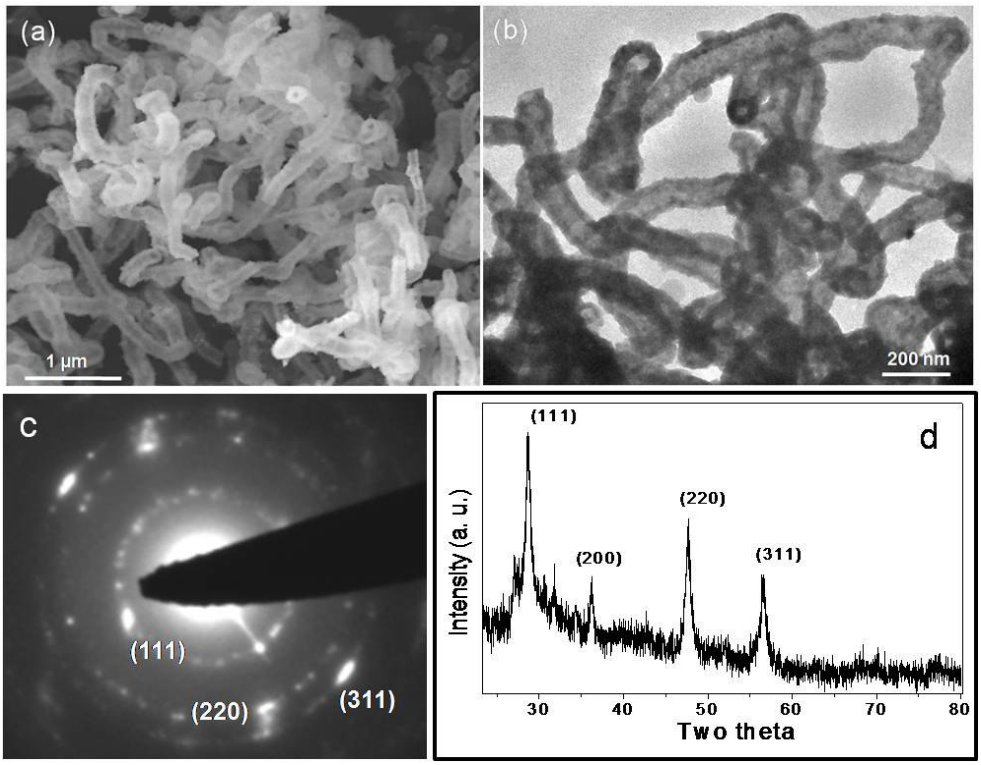

Figure 2.11: (a) FESEM image, (b) TEM image (c) SAED pattern and (d) XRD pattern of ZnS nanotubes.

rings of the SAED pattern can be index to (111), (220) and (311) reflections of ZnS. The XRD pattern of the as prepared nanotubes shown in Figure 2.11 (d) confirms the formation of ZnS with the cubic structure (JCPDF card: No. 01-0792, a = 5.4 Å).

2.4.6 Cd nanowires to CdS and CdSe nanotubes

Cd nanowires prepared by nebulized spray pyrolysis (see the FESEM and TEM images in Figure 2.12 (a) and (b)) had diameters varying from 80 to 400 nm, with lengths of several micrometers. The Cd nanowires have a smooth surface with zigzag

morphology. The XRD pattern of the nanowires is characteristic of the hexagonal structure of cadmium (JCPDF card: No. 85-1328, a = 2.97 Å, c = 5.61 Å) (See Figure 2.13). Cadmium nanowires were transformed into CdS nanotubes by heating with sulphur powder in an Ar atmosphere at 773 K for 3h. In Figure 2.14 (a), we show a

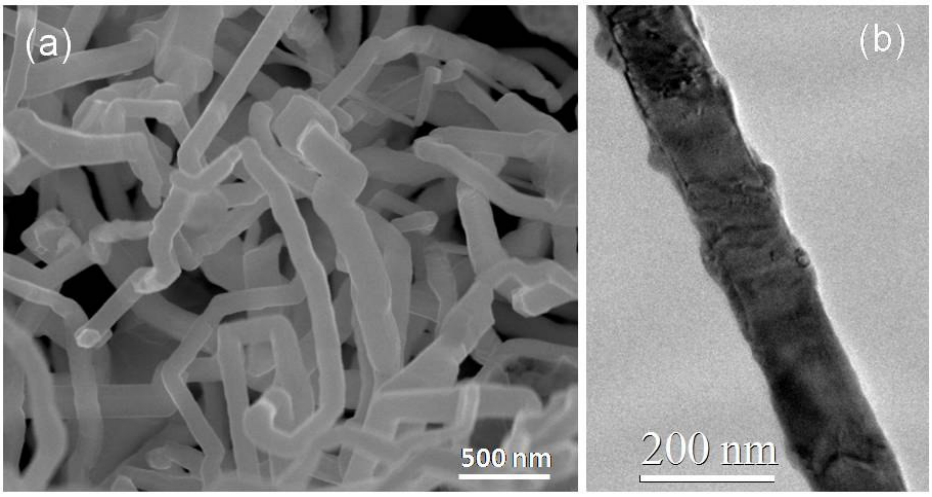

Figure 2.12: (a) FESEM image Cd nanowires and (b) TEM image of a Cd nanowire

FESEM image of the CdS nanotubes. The nanotubes have a smooth surface with diameter in the range of 100 to 500 nm. The length of nanotubes goes up to several

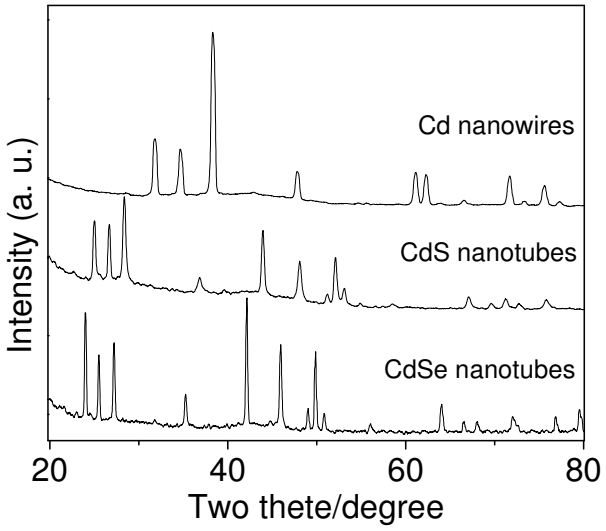

Figure 2.13: XRD patterns of Cd nanowires, CdS nanotubes and CdSe nanotubes

microns just as the starting Cd nanowires. A TEM image of an individual CdS nanotube is shown in Figure 2.14 (b). The diameter of this nanotube is around 200 nm with a wall thickness of 30-40 nm. The XRD pattern of the CdS nanotubes establishes the hexagonal structure with lattice parameters of a = 4.1 Å and c= 6.7 Å (JCPDF card: No. 01-0783).

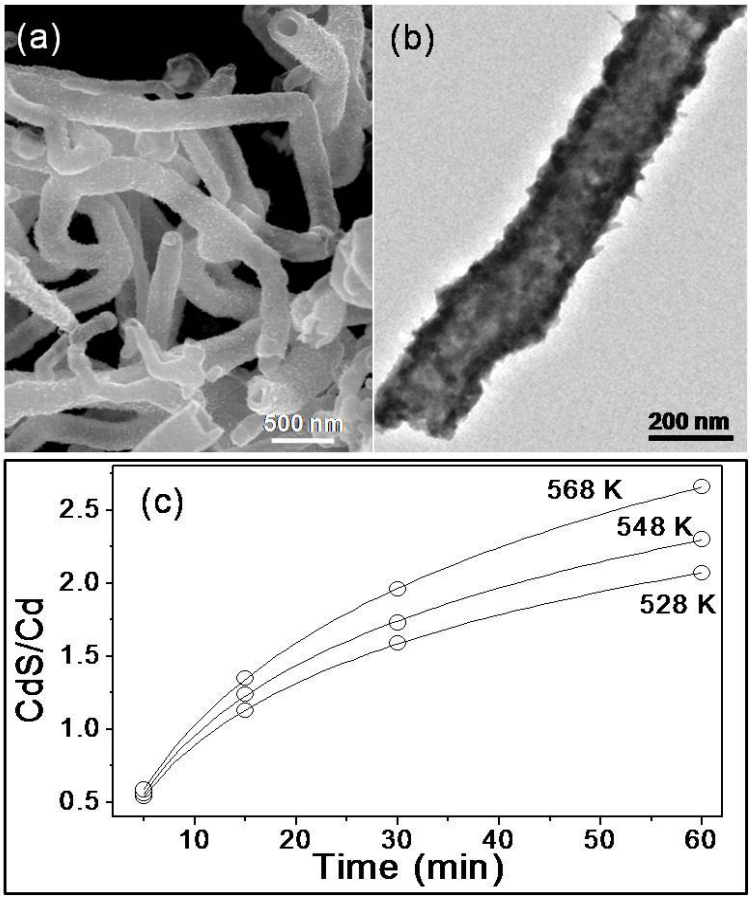

Figure 2.14: (a) FESEM image, (b) TEM image of a CdS nanotube, (c) Plots of the ratios of areas under CdS (110) and Cd (101) reflections against reaction time at different temperatures (open symbols). Solid curves represent the logarithimic rate law fit to the experimental data.

The kinetics of the transformation of the Cd nanowires to CdS nanotubes was studied by recording the XRD patterns after different periods of the reaction at 528, 548 and 568 K. These XRD patterns clearly show increase in the intensity of the CdS reflections with

time. The ratios of areas under the (110) reflection of CdS and the (101) reflections of Cd are plotted against time in Figure 2.14 (c). The solid lines in Figure 2.14 (c) show the fits of the experimental data to logarithimic rate law as given by Equation (1). From the rate constants so obtained, we estimate the activation energy for the conversion to be 8.5 kcal/mol. The activation energy reported for the formation of an anodic film of CdS on a Cd electrode is 10.6 kcal/mol.[32] Formation of CdS nanocrystals starting from Cd-stearate and tributylphosphine sulfide in a paraffin hot matrix involves an activation energy of 51.9 kcal/mol.[33] Thus, the conversion of Cd nanowires to CdS nanotubes involves a lower activation energy than that for bulk conversions.

It has also been possible to obtain CdSe nanotubes starting from Cd nanowires. In Figure 2.15 (a), we show a FESEM image of a single CdSe nanotube obtained by

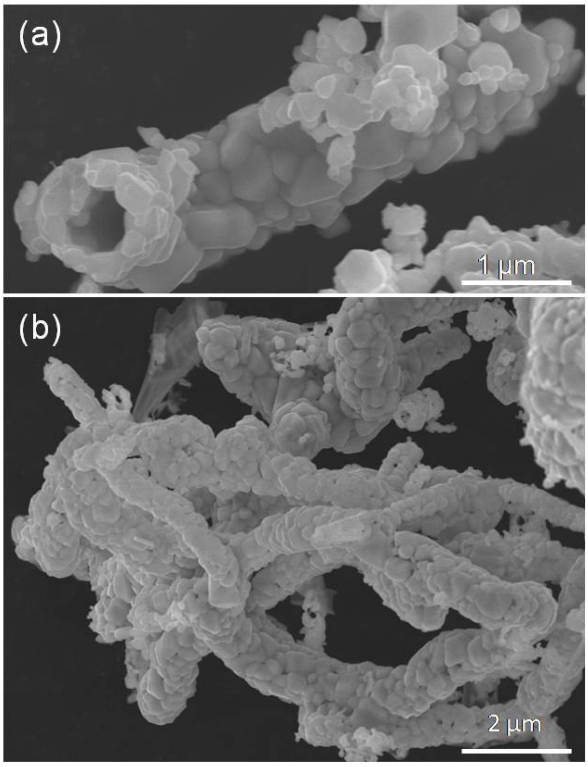

Figure 2.15: (a) and (b) FESEM image of CdSe nanotubes.

heating an intimate mixture Cd nanowires and Se powder. The nanotubes have a diameter of around 800 nm with a wall thickness in the range of 200 to 250 nm. The granular wall of the nanotube is made up of CdSe nanocrystals. A low magnification FESEM image of CdSe nanotubes is shown in Figure 2.15 (b). The XRD pattern of the nanotubes (Figure 2.13) is shown to have the cubic structure. (JCPDF card: No. 03-0544, a = 5.42 Å).

2.5 Conclusions

We have investigated the structures as well as the formation kinetics of 1D hollow nanostructure of oxides and other materials formed by the transformation of elemental nanowires through Kirkendall effect. A detailed study of the formation of ZnO nanotubes starting from Zn nanowires has been carried out by employing X-ray diffraction and electron microscopy. The transformation requires only a small activation energy of 12.2 kcal/mol. Nanotubes of $ZnCr_2O_4$ are obtained by the reaction of Zn nanowires with CrO_2Cl_2 in oxygen. It has been possible to obtain nanotubes of SiO_2, Co_3O_4, ZnS, CdS and CdSe by the reaction of the corresponding elemental nanowires with oxygen or the chalcogen. In the case of SiO_2, the nanotubes are crystalline with the cristobalite structure. The activation energy of formation of CdS nanotubes is also small. The present study demonstrates how Kirkendall effect can be exploited as a novel means of producing nanotubes of a variety of inorganic materials. Furthermore, the study throws light on the mechanism of the Kirkendall effect in forming hollow nanotubes from nanowires.

References

1. E. O. Kirkendall, *Trans. AIME*, **147**, *104,* 1942,

2. A. D. Smigelskas and E. O. Kirkendall, *Trans. AIME*, **171**, *130*, 1947.

3. H. Nakajima and J. Miner. *Met. Mater.Soc*., **49**, *15,* 1997.

4. A. Paul, PhD thesis, Technische Universiteit Eindhoven, The Netherlands, 2004.

5. H. J. Fan, U. Gcsele and M. Zacharias, *small*, **3**, *1660*, 2007.

6. L. C. C. D. Silva and R.F. Mehl, *Trans. AIME,* **191,** *155*, 1951.

7. C. E. Birchenall, *J. Electrochem. Soc.,* **103**, *619*, 1956.

8. J. C. Colson, M. Lambertin and P. Barret, in *Proc. 7th Int. Symp. Reactivity of Solids,* (Ed: J. S. Anderson, F. S. Stone and M. W. Roberts), Chapman & Hall, London, 1972.

9. D. L. Anton and A. G. Giamei, *Mater. Sci. Eng.*, **76**, *173,* 1985.

10. D. Tomus, K. Tsuchiya, M. Inuzuka, M. Sasaki, D. Imai, T. Ohmori and M. Umemoto, *Scr. Mater.*, **48**, *489*, 2003.

11. J. D. Kelin, G. Warshaw, N. Duziak, S. F. Cogan and R. M. Rose, *IEEE Trans. Magn*., **17**, *380,* 1981.

12. Y. Yin, R. M. Rioux, C. K. Erdonmez, S. Hughes, G. A. Somorjai and A. P. Alivisatos, *Science,* **304,** *711*, 2004.

13. C. N. R. Rao and A. Govindaraj, *Nanotubes and nanowires;* RSC publishing: Cambridge, 2005.

14. C. N. R. Rao, S. R. C. Vivekchand, K. Biswas and A. Govindaraj, *Dalton Trans.,* **34,** *3728,* 2007.

15. C. H. B. Ng, H. Tan and W. Y. Fan, *Langmuir,* **22**, *9712,* 2006.

16. U. K. Gautam, Y. Bando, J. Zhan, P. M. F. J. Costa, X. Fang and D. Golberg, *Adv. Mater.,* **20**, *810,* 2008.

17. H. J. Fan, M. Knez, R. Scholz, K. Nielsch, E. Pippel, D. Hesse, M. Zacharias and U. Gosele *Nat. Mater.,* **5**, *627*, 2006.

18. X. Chen, Z. Zhang, Z. Qiu, C. Shi and X. Li, *J. Colloid Interface Sci.,* **308**, *271*, 2007.

19. S. R. C. Vivekchand, G. Gundiah, A. Govindaraj and C. N. R. Rao, *Adv. Mater.,* **16**, *1842*, 2004.

20. G. Gundiah, F. L. Deepak, A. Govindaraj and C. N. R. Rao, *Chem. Phys. Lett.,* **381**, *579,* 2003.

21. D. Kim, J. Park, K. An, N. K. Yang, J. G. Park and T. Hyeon, *J. Am. Chem. Soc.,* **129**, *5812,* 2007.

22. V. O. Nwoko and H. H. Uhlig, *J. Electrochem. Soc.,* **112**, *1181,* 1965.

23. W. H. J. Vernon, E. A. Calnan, C. J. B. Clews and T. Nurse, *J. Proc. R. London A,* **216**, *375,* 1953.

24. R. A. Konetzki and Y. A. Chang, *J. Mater. Res.,* **4**, *1421*, 1989.

25. N. F. Mott, *Trans. Faraday Soc.,* **43,** *429,* 1947.

26. A. T. J. Formhold, *J. Phys. Chem. Solids,* **24**, *1081,* 1963.

27. D. J. Young and M. J. Dignam, *Oxid. Met*., **5**, *241*, 1972.

28. B. L. Maschhoff and N. R. Armstrong, *Langmuir,* **7**, *693*, 1991.

29. N. Cobrera and N. F. Mott, *Rep. Prog. Phys.,* **12,** *163,* 1949.

30. W. J. Moore and J. K. Lee, *Trans. Faraday Soc.,* **45**, *501*, 1951.

31. W. J. J. Moore, *Chem. Phys.,* **20**, *764*, 1952.

32. L-S. R. Yeh, P. G. Hudson and A. Damjanovic, *J. Appl. Electrochem.,* **12**, *153*, 1982.

33. G. G. Yordanov, E. Adachi and C. D. Dushkin, *Colloids Surf. A,* **289**, *118*, 2006.

CHAPTER 3

Synthesis and characterization of metal oxide nanorod brushes*

Summary

This chapter describes the synthesis and characterization of metal oxides nanorod brushes. Nanorod brushes of α-Al_2O_3, MoO_3 and ZnO have been synthesized using amorphous carbon nanotube (a-CNT) brushes as the starting material. Nanobrushes of α-Al_2O_3 and MoO_3 are made up of single crystalline nanorods. In the case of ZnO nanobrushes, the nanorod bristles are made by the fusion of 15 to 25 nm size nanoparticles and are porous in nature. Metal oxide nanorod brushes thus obtained have been characterized by XRD, FESEM, TEM and Raman spectroscopy. Single crystalline ruby nanorods were obtained by introducing chromium ions during the synthesis of alumina rods.

---

*A paper based on this study has been published in *Bull. Mater. Sci.*, (**2008**).

3.1 Introduction

Avid attention has been paid to the synthesis of nanomaterials with different morphologies, such as nanoparticles, nanotubes, nanosheets and nanohelices, because the properties of nanomaterials are strongly dependent on their size and shape. [1-3] Among different shapes, one-dimensional nanostructures caught special attention due to its unique properties and potential applications.[4-6] One-dimensional nanostructures are good candidate for the application in mesoscopic physics and fabrication of nanoscale devices.[4,7] It also provides a good system to study dependence of electrical and thermal transport or mechanical properties on dimensionality and quantum confinement. They are also important as both interconnect and functional units in fabricating electronic, optoelectronic, electrochemical and electromechanical devices in nanometer scale. Several synthetic strategies have been developed for achieving large quantity of 1D nanostructures from a wide range of materials, rapidly at reasonably low cost. These synthetic strategies include dictation of anisotropic crystallographic structure of a solid, direction through a template, self-assembly, introduction of a liquid-solid interface to reduce symmetry of a seed and kinetic control provided by a capping agent. Out of these strategies, template based methods provide a simple, high-through-put and cost effective procedure.[6,8] It also allows duplicating complex topology present at the surface of template in a single step for a diversified range of materials like metal oxides, metal chalcogenides, pure metals and ceramics. Special attention has been paid to the metal oxide nanorods because of their improved properties compared to their bulk-counterparts.[8-10] For many technological applications, it is highly desirable to produce nanorods in brush morphology covering a large area. These

nanorod brushes are also important for understanding of fundamental physical concepts.

Aluminium oxides are remarkable materials with broad applicability in the chemical and petrochemical industry as adsorbents, catalyst supports or as a part of bifunctional catalysts. These oxides have also been utilised as capacitor dielectrics and gate oxides in memory device owing to its high dielectric constant, very low permeability and high thermal conductivity.[11-13] Aluminium oxide crystallises in a number of different modifications. The three most important crystal structures are alpha (stable), kappa (metastable) and gamma (metastable). Alpha alumina is the most stable aluminium oxide phase at all temperatures. It has a trigonal structure (R-3c) with ABAB... stacking of oxygen planes with Al ions in 2/3 of the octahedral interstitial positions (see Figure 3.1).

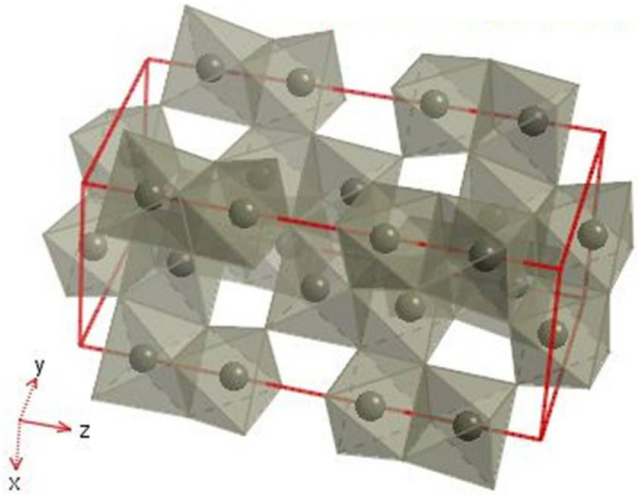

Figure 3.1: Crystal structure of alpha alumina

Currently different nano-structure of α-alumina like nanowires, nanotubes and nanorods are in the focus of both academic and industrial research because of their

interesting one-dimensional characteristics and possible applications in nanomaterials-based electronics.

Orthorhombic molybdenum trioxide (α-MoO_3), a wide-gap, n-type semiconductor material, has attracted considerable interest due to its layered crystal structures and wide applications in electronic display systems, solid state micro-batteries, gas sensors and recording materials.[14-16] It is one of the most widely used catalysts for selective oxidation reactions in petroleum refinery, chemical production and pollution control industries.[17]

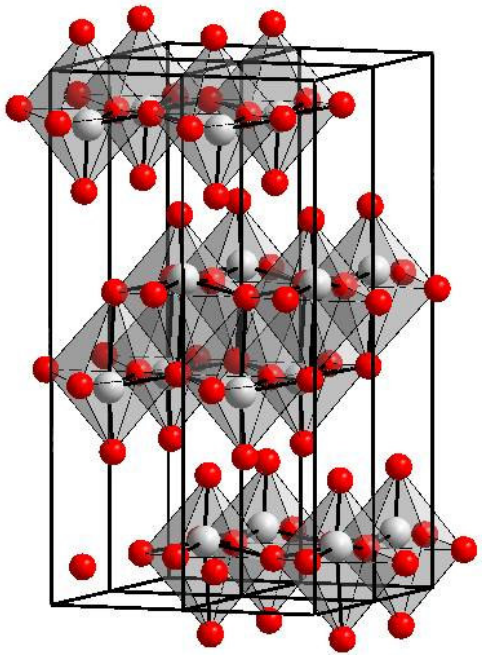

Figure 3.2: Crystal structure of orthorhombic molybdenum trioxide (α-MoO_3)

In α-MoO_3, the asymmetrical MoO_6 octahedra are interconnected through corner-linking along [100] direction and edge-sharing along [001] direction to form double-layer sheets parallel to the (010) plane as shown in Figure 3.2. The weak interactions between the double-layer sheets are mostly van der Waals forces.[18] Nanostructures of MoO_3 can find applications in lubricants,[19,20] sensors,[21,22] rechargeable lithium-ion batteries [23] and field emission nanodevices.[24-26]

Zinc oxide is a direct and wide band gap (3.37 eV) semiconductor with a large exciton binding energy (60 meV). It is one of the most interesting functional materials with a number of unique properties like transparent conductivity, near-UV emission,[27] UV absorption,[28] field-emission capabilities[29] and piezoelectricity. Zinc oxide crystallizes in three different forms: wurtzite (hexagonal), zincblende (cubic) and the rarely observed rocksalt (cubic). Figure 3.3 shows wurtzite and zincblende structure of ZnO. The wurtzite structure is the most stable at ambient conditions and thus most common. The zincblende form can be stabilized by growing ZnO on substrates with cubic lattice structure. In both the cases, the zinc and oxide centres are tetrahedral as seen from Figure 3.3. The rocksalt (NaCl-type) structure is observed only at relatively high pressure of about 10 GPa.[30] As in most group II-VI materials, the bonding in ZnO is largely ionic, which explains its strong piezoelectricity.

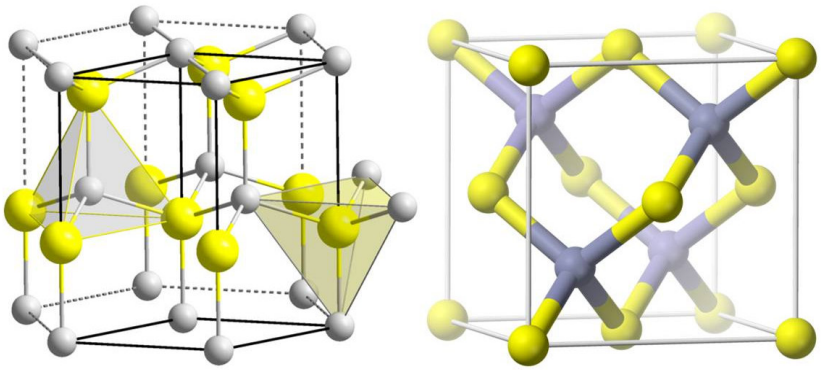

Figure 3.3: Wurtzite and zincblende structures of ZnO

Due to its unique properties, nanomaterials of ZnO stimulate a wide range of research interest. As a result, ZnO has been synthesized in variety of attractive morphologies including nanotubes, nanowires, nanohelices, nanonails, nanobowls and nanoflowers. One-dimensional nanostructures of ZnO are promising materials in

number of potential applications, which include gas sensors,[31,32] solar cells,[33] nanolasers[34] and transparent ultraviolet protection film.

3.2 Scope of the present investigations

Synthesis of one dimensional metal oxide nanostructures is getting enormous attention in recent years due to their potential applications in nanoelectronics, photonics, data recording media, gas sensing and gas storage.[3] Though several transition metal oxides in the form of wires, tubes and rods were reported using various chemical and physical methods, synthesis of Al_2O_3 and MoO_3 nanorods has generated a great deal of interest owing to their improved mechanical and catalytic behaviour, nonlinear optical characteristics and unusual optical luminescence properties. Various approaches to synthesize these metal oxide nanorods involve vapour-liquid-solid growth, vapour-solid growth, laser ablation, solvothermal, electrochemical and carbothermal methods.[3,35] Al_2O_3 nanowires were obtained by vapor-liquid-solid growth in presence of SiO_2 and Fe act as catalyst.[36-39] Rao et al[40,41] synthesized crystalline γ-Al_2O_3 and MoO_3 nanotubes through carbothermal route by coating the functionalized carbon nanotubes with aluminium iso-propoxide. In a similar approach, Li et al[42] reported the formation of single crystalline alumina nanofibers using mesoporous carbon aerogels as substrate and aluminium nitrate as the source. Short alumina nanotubes have also been fabricated by controlling anodization process of aluminium in dilute sulfuric acid.[43,44] Xiao et al,[45] electrodeposited alumina inside the pores of alumina membrane and finally etched out the membrane using aqueous NaOH solution to obtain alumina nanotubes and nanowires. Lee et al,[46] synthesized alumina nanowires by hydrothermal method in presence of surfactants. α-Al_2O_3 nanobelts and nanosheets with different

morphologies and size have been prepared by a chemical route from H_2O and Al in argon atmosphere at high temperature.[47] Kim and co-workers synthesized amorphous Al_2O_3 nanotubes by atomic layer deposition of alumina on ZnO core followed by etching the ZnO.[48] Indeed, similar methods were adopted for the preparation of MoO_3 nanowires and nanotubes by several researchers.[49-52] In all these cases, the one-dimensional morphologies obtained for Al_2O_3 and MoO_3 were mostly restricted to tubular and fibrous structures. Formation of aligned, single-crystalline nanorods was not reported so far by any chemical route. In this report, we have synthesized crystalline Al_2O_3, MoO_3 and ZnO nanorod brushes using amorphous carbon nanotube (a-CNT) brushes as the starting materials. Amorphous carbon nanotube brushes[53] were derived from the carbonization of glucose within the polycarbonate membranes. By introducing chromium during the synthesis of alumina nanorods we have also obtained single crystalline ruby nanorod brushes.

3.3 Experimental and related aspects

3.3.1 Synthesis of a-CNT brushes

Amorphous carbon nanotube (a-CNT) brushes were prepared by the following procedure.[53] Polycarbonate membranes with a pore diameter of 220 nm were soaked in 22 mL of 0.5 M aqueous solution of glucose in a 25 mL Teflon-lined autoclave. The temperature of the autoclave was maintained at 453 K for 6 h after which it was allowed to cool to room temperature. The brownish liquid, rich in carbon spheres was discarded. The membranes that had turned brown were washed with deionized water and ethanol several times and dried at 313 K for 1 h.

3.3.2 Synthesis of metal oxide nanorod brushes

To obtain Al_2O_3 nanorods, the brown coloured membrane was first soaked in 0.5 M solution of aluminium nitrate nonahydrate for 12 h and then dried at 318 K for 5 h. The composite was further heated at 1373 K for 3 h to give white coloured Al_2O_3 nanorods. Pink coloured ruby nanorods were prepared by introducing 0.25 g (Cr/Al = 0.025) chromium nitrate nonahydrate along with the aluminium nitrate precursor during the synthesis. For MoO_3 rods, the membrane was soaked in the 0.028 M solution of ammonium heptamolybdate tetrahydrate for 12 h followed by drying at 318 K for 5 h. In the case of ZnO nanorods, 0.5 M solution of zinc nitrate was used. The Zn and Mo precursor loaded composite membranes were thermally treated at 703 K for 3 h to obtain bluish coloured MoO_3 and white coloured ZnO nanorod brushes. The products were investigated by electron microscopy and other physical techniques.

3.3.3 Characterization Techniques

X-ray diffraction (XRD): X-ray diffraction patterns of nanorod brushes were recorded at 298 K with a Rich-Siefert 3000-TT diffractometer employing Cu Kα radiation.

Scanning Electron Microscopy (SEM): The morphology of the nanotubes was examined by a Field Emission Scanning Electron Microscope (FESEM, FEI Nova-Nano SEM-600, Netherlands) and scanning electron microscope (SEM) Leica S-440I instrument (U.K).

Transmission Electron Microscopy (TEM): TEM images were recorded with a JEOL JEM 3010 instrument (Japan) operated at an accelerating voltage of 300 kV.

Raman spectroscopy: Raman spectra were recorded with a LabRAM HR with 633 nm line from HeNe laser.

Photoluminescence: Photoluminescence studies were done by using Perkin Elmer LS 50B instrument using a Xe lamp source.

3.4 Results and discussion

In Figure 3.4 (a), we show a FESEM image of a-CNTs, after dissolution of polycarbonate membrane using dichloromethane. All these nanotubes are well aligned and packed together as brushes. The length of the nanotube is around 15 µm. The outer diameter of the nanotube is around 250 nm with the wall thickness of 45 nm (Figure 3.4 (b)).

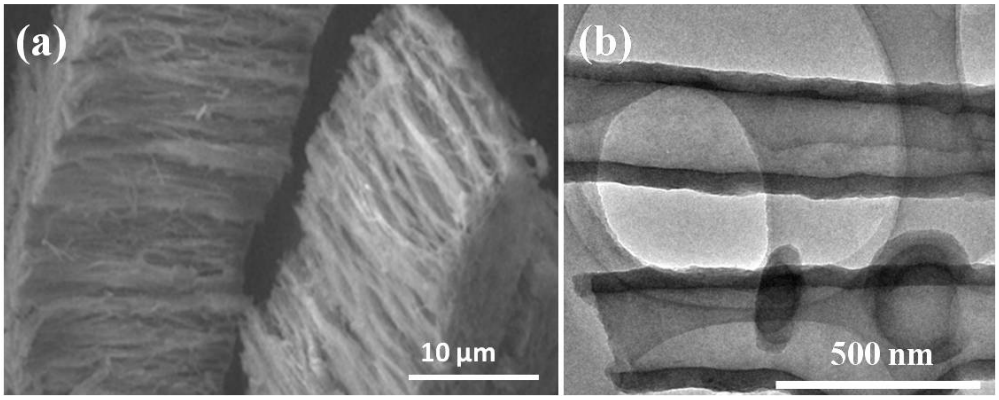

Figure 3.4: (a) FESEM image of a-CNTs (b) TEM image of a-CNTs

3.4.1 α-Al_2O_3 nanorod brushes

Calcination of amorphous carbon membrane filled with aluminium precursor at high temperature (1373 K) yields crystalline alumina nanorods with brush like morphology analogous to a-CNT brushes. Figure 3.5 (a) shows a low magnification FESEM image of α-Al_2O_3 nanorods in which all the nanorods are well aligned and packed together covering a large area. The high magnification FESEM image of the rods in Figure 3.5 (b), viewed perpendicular to the rod axis, shows a smooth surface with occasional joints all along their length indicating the end to end fusion of

alumina nanorods of 1 μm length. A TEM image of an individual nanorod shown in Figure 3.5 (c) reveals that the diameter of the tube is around 150 nm. Inset of Figure 3.5 (c) is the corresponding electron diffraction pattern revealing the single

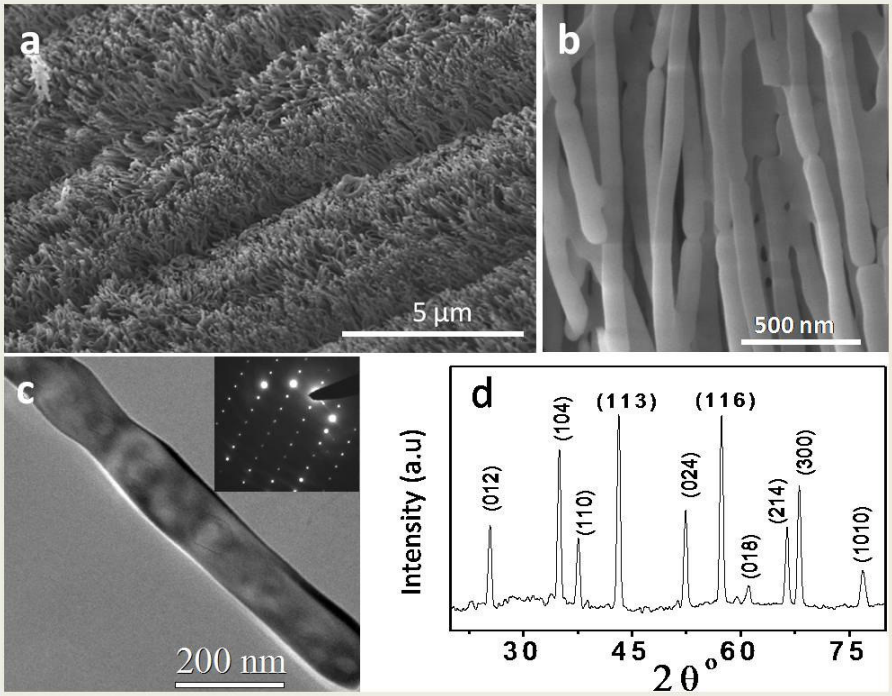

Figure 3.5: (a) FESEM image, (b) Higher magnification FESEM image of α-Al_2O_3 nanorods (c) TEM image of a nanorod (inset shows corresponding ED pattern) (d) XRD of α-Al_2O_3 nanorods

crystalline nature of the nanorods. The XRD pattern of the Al_2O_3 nanorods shows all the reflections indexed to pure α-Al_2O_3 corundum structures with cell parameter a = 4.758 Å and b = 12.99 Å (JCPDF card No: 461212). The sharp peaks in the XRD pattern reflect the crystalline nature of the nanorods, supporting the electron diffraction pattern.

Ruby nanorod brushes

Cr doped single crystalline α-Al_2O_3, (ruby) is the first solid state laser invented in 1960.[54] Ruby is still used in number of applications where short pulse of

red light is required. Ruby produces a pulse of visible light with a wavelength of 694 nm. Nanorods of ruby were not reported hitherto. We have obtained single crystalline ruby nanorods by introducing chromium ions during the synthesis of

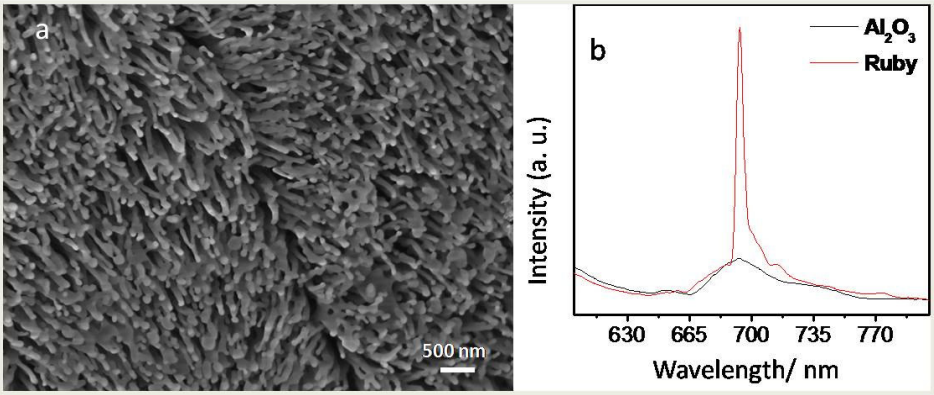

Figure 3.6: (a) FESEM image of ruby nanorods (b) PL spectra of ruby and alumina nanorods

single crystalline alumina rods. A FESEM image of well-aligned ruby nanorods is shown in Figure 3.6 (a). In Figure 3.6 (b), the photoluminescence property of the ruby nanorods is compared with the α-Al_2O_3 nanorods. The intense PL peak of ruby nanorods at 693.5 nm is several times stronger than the α-Al_2O_3 nanorods. In addition, it shows a very sharp emission peak, with narrow bandwidth as against the broad emission peak for alumina. The characteristic R1 and R2 peaks of ruby merge to a single peak due to temperature broadening and low-resolution power of the instrument.

3.4.2 MoO_3 nanorod brushes

In Figure 3.7 (a), we show a FESEM image of MoO_3 nanorods exhibiting brush like morphology similar to that of a-CNTs brush template. The average diameter of the nanorods is around 190 nm. The length of these nanorods is less than

2 μm and is not up to the thickness of the membrane suggesting the discontinuity in the structure. TEM image shown in Figure 3.7 (b) confirms the rod like morphology of MoO_3. The electron diffraction pattern shown in the inset of Figure 3.7 (b) indicates that the nanorods were single crystalline. Figure 3.7 (c) shows the XRD

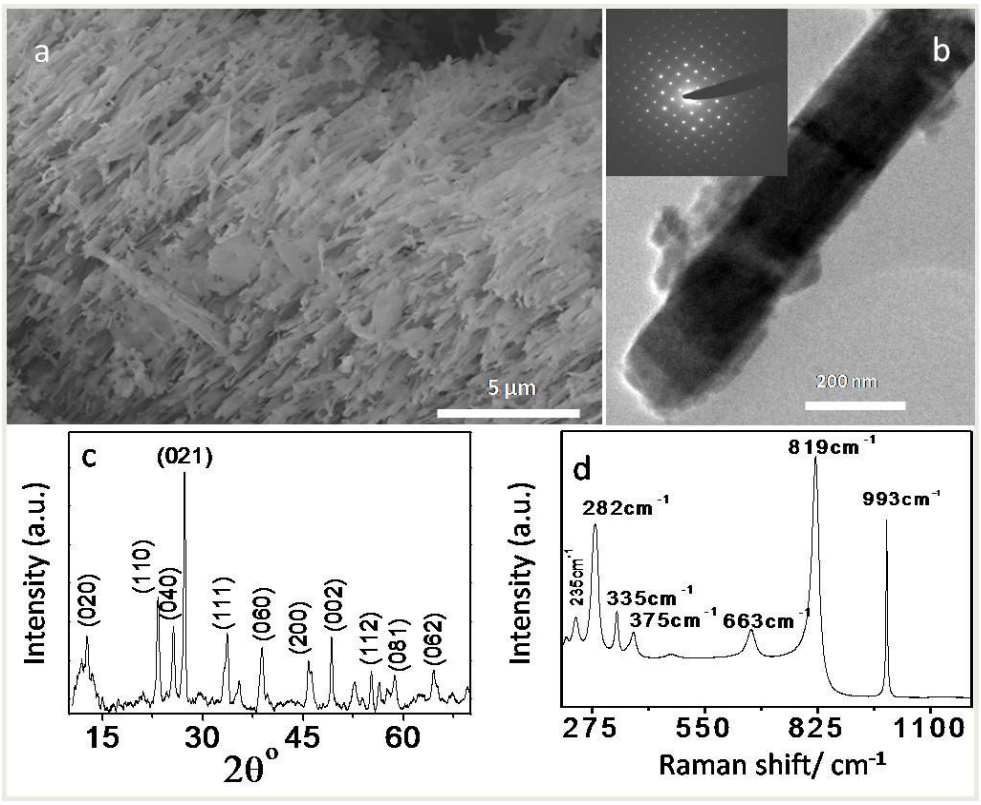

Figure 3.7: (a) FESEM image of MoO_3 nanorods (b) TEM image of an individual MoO_3 nanorod (inset shows corresponding SAED pattern) (c) XRD pattern of MoO_3 nanorods (d) Raman spectra of MoO_3 nanorods

pattern of MoO_3, the strong intensity of the peaks indicates the high crystallinity of the nanorods. All the peaks can be indexed to the pure phase of α-MoO_3 with the orthorhombic structure and lattice parameters are a = 3.96 Å, b = 13.86 Å and c = 3.7 Å (JCPDS card number 05-0508). The nanorods show the characteristics Raman bands for the MoO_3 crystal (Figure 3.7 (d)) at 235(B_{3g}), 282(B_{2g}, B_{3g}), 335(B_{1g}, A_g), 375(B_{1g}), 663(B_{2g}, B_{3g}), 819(A_g, B_{1g}) and 993(A_g, B_{1g}) cm^{-1}.

3.4.3 ZnO nanorod brushes

Figure 3.8 (a) shows a FESEM image of aligned ZnO nanorods obtained through the a-CNT template. In contrast to Al_2O_3 and MoO_3, ZnO nanorods are made up of small nanoparticles of around 15 to 25 nm diameter. The diameter of the

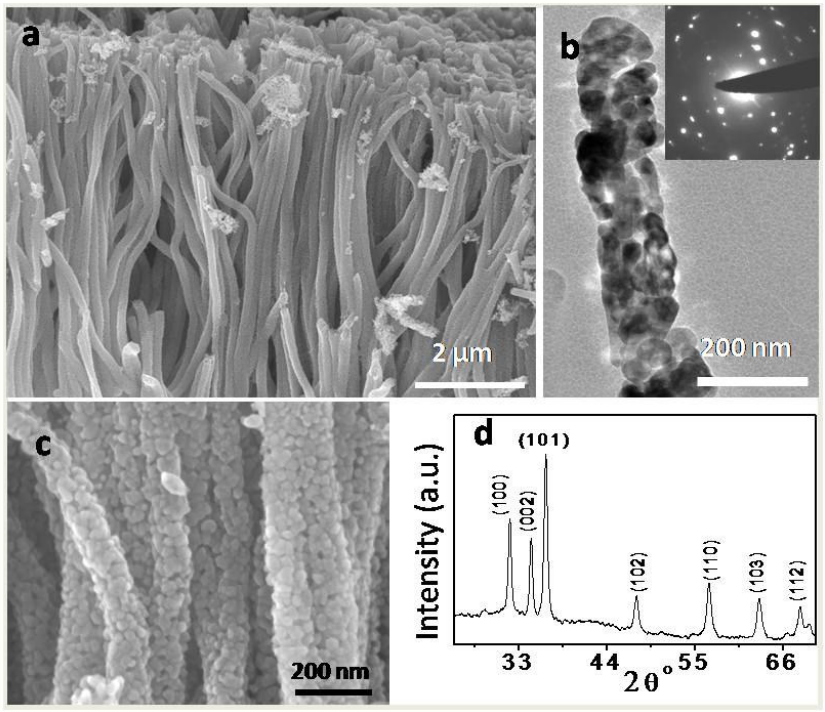

Figure 3.8: (a) FESEM image of ZnO nanorods (b) TEM Image of an individual ZnO nanorod (inset ED pattern on the nanorod) (c) Higher magnification FSESEM image of ZnO nanorods (d) XRD pattern of ZnO nanorods

nanorods is in the range of 150 to 180 nm with lengths of about 15 µm. TEM image shows that nanoparticles are fused randomly to form a nanoporous rod. The Electron diffraction pattern shown in the inset of Figure 3.8 (b) confirms the polycrystalline nature of the nanorods. The broad peaks observed in the XRD pattern further support our observation that the nanorods are composed of ZnO nanoparticles. These porous nanostructures might have high surface area with good potential applications.

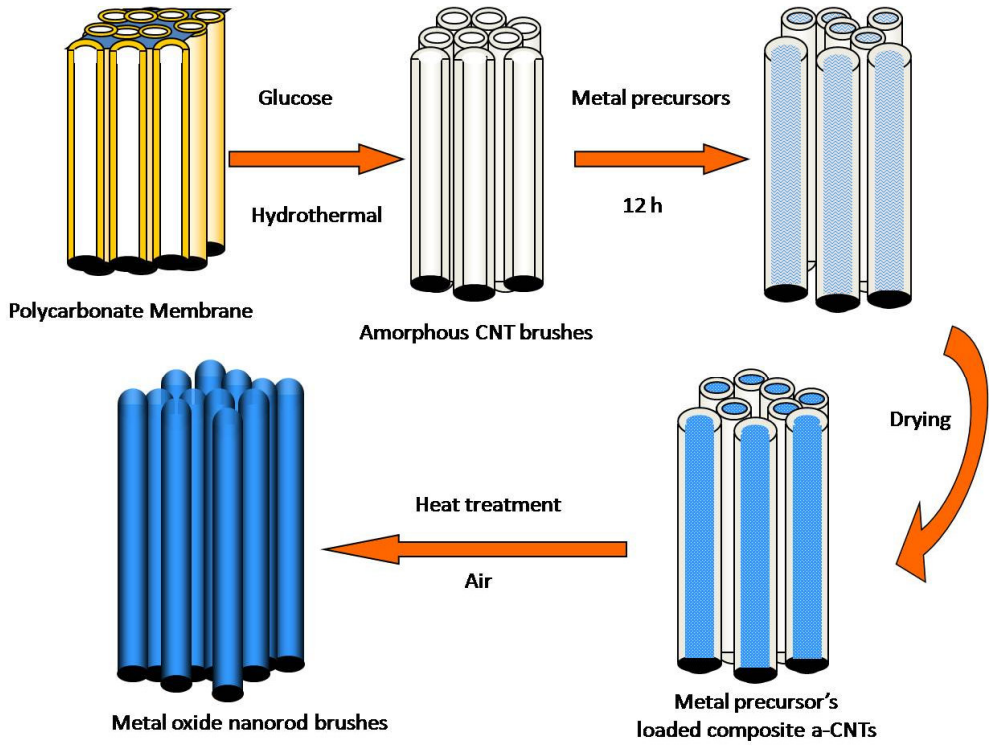

Scheme 1. Scheme showing the synthesis of metal oxide nanorod brushes.

3.5 Conclusions

In conclusion, we have utilized the amorphous carbon nanotube brushes as template to prepare single crystalline nanorod brushes of Al_2O_3 and MoO_3 and polycrystalline brushes of ZnO. We believe that the presence of carboxylic and phenolic functional groups present on the surface of the a-CNT helps to hydrolyze the metal precursors within the voids of the membrane which would subsequently form a polymer network (Scheme 1). Further calcination at high temperatures, coupled with the exothermic heat generated by the combustion of carbon facilitates the formation of crystalline nanorods of metal oxides.

References

1. A. P. Alivisatos, *Science*, **271**, *933,* 1996.

2. C. N. R. Rao, G. U. Kulkarni, P. J. Thomas and P. P. Edwards, *Chem. Eur. J.* **8**, *29,* 2002.

3. C. N. R. Rao and A. Govindaraj, *Nanotubes and Nanowires*, Cambridge RSC Publishing, 2005.

4. J. Hu, T. W. Odom and C. M. Lieber, *Acc. Chem. Res*. **32***, 435,*1999.

5. C. N. R. Rao and M. Nath*, DaltonTrans*., *1*, 2003.

6. Y. Xia, P. Yang, Y. Sun, Y. Wu, B. Mayers, B. Gates, Y. Yin, F. Kim and H. Yan, *Adv. Mater*. **15**, *353,* 2003.

7. Z. L. Wang, *Adv. Mater*, **12**, *1295,* 2000.

8. J. C. Hulteen and C. R. Martin, *J. Mater. Chem.*, **7**, *1075,* 1997.

9. E. Comini, L. Yubao, Y. Brando and G. Sberveglieri, *Chem. Phys. Lett.* **407**, *368,* 2005.

10. J. Rajeswari, B. Viswanathan and T. K. Varadarajan, *Mater. Chem. Phys.,* **106**, *168,* 2007.

11. Y. Kim, S. M. Lee, C. S. Park, S. I. Lee and M. Y. Lee, *Appl. Phys. Lett.,* **71**, *3604*, 1997.

12. W. S. Jeon, S. Yang, C. S. Lee and S. W. Kang, *J. Electrochem. Soc.,* **149,** *C306,* 2002.

13. E. P. Gusev, M. Copel, E. Cartier, I. J. R. Baumvol, C. Krug and M. A. Gribelyuk, *Appl. Phys. Lett.,* **76**, *176*, 2000.

14. Z. Hussain, *J. Mater. Res.,* **16**, *2695,* 2001.

15. M. Ferroni, V. Guidi, G. Martinelli, M. Sacerdoti, P. Nelli and G. Sberveglieri, *Sens. Actuators B,* **48**, *285*, 1998.

16. H. C. Zeng, *Inorg. Chem.,* **37**, *1967*, 1998.

17. H. F. Liu, R. S. Liu, K. Y. Liew, R. E. Johnson and J. H. Lunsford, *J. Am. Chem. Soc.*, **106**, *4117*, 1984.

18. X. W. Lou and H. C. Zeng, *Chem. Mater.*, **14**, *4781***,** 2002.

19. P. E. Sheehan and C. M. Lieber, *Science*, **272,** *1158,* 1996.

20. J. Wang, K. C. Rose and C. M. Lieber, *J. Phys. Chem. B*, **103**, *8405*, 1999.

21. E. Comini, L. Yubao, Y. Brando and G. Sberveglieri, *Chem. Phys. Lett.,* **407**, *368,* 2005.

22. A. M. Taurino, A. Forleo, L. Francioso, P. Siciliano, M. Stalder and R. Nesper, *Appl. Phys. Lett.*, **88**, *15211*, 2006.

23. W. Li, F. Cheng, Z. Tao and J. Chen, *J. Phys. Chem. B,* **110**, *119*, 2006.

24. Y. B. Li, Y. Bando, D. Golberg and K. Kurashima, *Appl. Phys. Lett.,* **81**, *5048*, 2002.

25. J. Zhou, S. Z. Deng, N. S. Xu, J. Chen and J. C. She, *Appl. Phys. Lett.*, **83**, *2653*, 2003.

26. J. Zhou, N. S. Xu, S. Z. Deng, J. Chen, J. C. She and Z. L. Wang, *Adv. Mater.*, **15,** *1835,* 2003.

27. R. E. Service, *Science*, **276**, *895*, 1997.

28. E. A. Meulenkamp, *J. Phys. Chem. B*, **102**, *5566*, 1998.

29. D. Banerjee, S. H. Jo and Z. F. Ren, *Adv. Mater.*, **16**, *2028,* 2004.

30. U. Ozgur, Ya. I. Alivov, C. Liu, A. Teke, M. A. Reshchikov, S. Doğan, V. Avrutin and S. J. Cho, *J. Appl. Phys.,* **98**, *041301*, 2005.

31. J. Hu, T. W. Odom and C. M. Leiber, *Acc. Chem. Res.,* **32**, *435,* 1999.

32. N. J. Dayan, S. R. Sainkar, R. N. Karekar and R. C. Aiyer, *Thin Solid Films,* **325,** *254*, 1998.

33. Z. W. Pang, Z. R. Dai and Z. L. Wang, *Science,* **291,** *1949,* 2001.

34. M. H. Huang, S. Mao, H. Feick, H. Q. Yan, Y. Y. Wu, H. Kind, E. Weber, R. Russo and P. D. Yang, *Science,* **292**, *1897,* 2001.

35. C. N. R. Rao, S. R. C. Vivekchand, K . Biswas and A. Govindaraj, *Dalton Trans.,* **34**, *3728*, 2007.

36. V. Valcarcel, A. Souto and F. Guitian, *Adv. Mater.*, **10**, *138,* 1998.

37. C. C. Tang, S. S. Fan, P. Li, L. Chapelle, and H. Y. Dang, *J. Crystal Growth*, **224,** *117*, 2001.

38. X. S. Peng, L. D. Meng, X. F. Wang, C. Z. Wang and G. S. Wu, *J. Phys. Chem. B,* **106,** *11163*, 2003.

39. J. Zhou, S. Z. Deng, J. C. She and N. S. Xu, *Chem. Phys. Lett.*, **365**, *505*, 2002.

40. B. C. Satishkumar, A. Govindaraj, E. M. Vogl, L. Basmallick and C. N. R. Rao, *J. Mater. Res.,* **12**, *604*, 1997.

41. B. C. Satishkumar, A. Govindaraj, M. Nath and C. N. R. Rao, *J. Mater. Chem.*, **10,** *2115*, 2002.

42. W. Li, A. H. Lu, C. Weidenthaler, R. Goddard, H. J. Bongard and F. Schuth, *J. Mater. Chem.,* **15**, *2993*, 2005.

43. L. Pu, X. Bao, J. Zou and D. Feng, *Angew. Chem. Int. Ed*, **40**, *1490*, 2001.

44. J. Zou, L. Pu, X. Bao and D. Feng, *Appl. Phys. Lett.*, **80**, *1079*, 2002.

45. Z. L. Xiao, C. Y. Han, U. Welp, H. H. Wang, W. K. Kwok, G. A. Willing, J. M. Hiller, R. E. Cook, D. J. Miller and G. W. Crabtree, *Nano Lett.,* **2,** *1293,* 2002.

46. H. C. Lee, H. J. Kim, S. H. Chung, K. H. Lee, H. C. Lee and J. S. Lee, *J. Am. Chem. Soc.*, **125**, *2882*, 2003.

47. X. S. Fang, C. H. Ye, X. S. Peng, Y. H. Wang, Y. C. Wu and. L. D. Zhang, *J. Mater. Chem.*, **13,** *3040*, 2003.

48. J. Hwang, B. Min, J. S. Lee, K. Keem, K. Cho, M. Y. Sung, M. S. Lee and S. Kim, *Adv. Mater.,* **16**, *422,* 2004.

49. X. W. Lou and H. C. Zeng, *Chem. Mater.,* **14**, *4781*, 2002.

50. T. Xia, Q. Li, X. Liu, J. Meng and X. Cao, *J. Phys. Chem. B,* **110** *2006*, 2006.

51. R. Q. Song, A. W. Xu, B. Deng and Y. P. Fang, *J. Phys. Chem. B*, **109**, *22758*, 2005.

52. N. Niederberger, F. Krumeich, H. J. Muhr, M. M. Llerb and R. Nesper, *J. Mater. Chem.,* **11**, *1941*, 2001.

53. J. Dinesh, M. Eswaramoorthy and C. N. R. Rao, *J. Phys. Chem. C,* **111,** *510*, 2007.

54. T. H. Mayman, *Nature*, **187**, *493*, 1960.

CHAPTER 4

Synthesis, structure and properties of homogeneous BC_4N nanotube brushes and mesoporous microspheres*

Summary

This chapter deals with the synthesis, characterization and properties of boron carbon nitride ($B_xC_yN_z$) nanotube brushes and mesoporous microspheres. $B_xC_yN_z$ nanotube brushes have been obtained by the high temperature reaction of amorphous carbon nanotube (a-CNT) brushes with a mixture of boric acid and urea. The a-CNT brushes themselves were obtained by the pyrolysis of glucose in a polycarbonate membrane. The $B_xC_yN_z$ nanotubes have been characterized by EELS, XPS, electron microscopy, Raman spectroscopy and other techniques. The composition of these nanotubes is found to be BC_4N. The nanotubes, which are stable up to 900 °C, are insulating and nonmagnetic. They exhibit a selective uptake of CO_2 up to 23.5 wt%. In order to understand the structure and properties of nanotubes, first-principles

---

*Papers based on this work have been published in *J. Mater. Chem.* (**2008**) and *Z. Anorg. Allg. Chem.* **(2010)**.

density functional theory based calculations have been carried out on (6,0), (6,6) and (8,0) nanotubes with the composition BC_4N.

The reaction of low surface area amorphous carbon spheres with a mixture of urea and boric acid at 930 °C yields a composition close to BC_4N with a graphitic structure. BC_4N microspheres were characterized by electron energy loss spectroscopy, X-ray photoelectron spectroscopy, transmission electron microscopy, Raman spectroscopy and X-ray diffraction. BC_4N is a porous ceramic with a surface area of 428 $m^2 \cdot g^{-1}$ and shows a CO_2 uptake of 40 wt%. Similar to BC_4N nanotube brushes, the layered structure of BC_4N spheres involves a random distribution of boron, carbon and nitrogen atoms and shows high thermal stability up to 1000 °C. A comparative analysis of the structure and properties of BC_4N and graphene using first-principles pseudopotential based density functional theoretical calculations has been carried out. The calculations predict it to be an insulator.

4.1 Introduction

Materials containing boron, carbon and nitrogen ($B_xC_yN_z$) are of great importance with a variety of attractive properties and applications. The $B_xC_yN_z$ materials can be considered as a hybrid of graphite and boron nitride (h-BN).[1-4] Graphite and h-BN exhibit similar structure but quite different properties. h-BN is an insulator having limited intercalation properties while graphite is an excellant host material with semi-metallic conductivity. In the case of graphite, carbon atoms are linked to each other with one sp^2 hybridiesed C-C σ-bond and a delocalised π-overlaping involving p_z orbitals of all the carbon atoms resulting a two dimensional hexagonal network. These hexagonal sheets are stacked in an ABAB ... sequence, with a combination of orbital interactions and van der Waals bonding.[5,6] In each sheet, the combination of the p_z orbitals of the in-plane carbon atoms creates a valence band (VB) and a conduction band (CB). For an isolated graphene sheet, these bands meet at the Fermi level at the *K* point in the Brillouin zone. However, in bulk graphite the weak interaction of the sheets produces a small band overlap. This overlap of ~ 0.03 eV gives graphite its semimetallic character.[1,4,7] The electrical conductivity of highly oriented pyrolytic graphite (HOPG) is 2 x 10^4 S/cm in the ab-plane.[4] Hexagonal boron nitride sheets are similar to those of graphite with boron and nitrogen atoms occupying the alternating positions of the hexagons, but h-BN has a different stacking arrangement. The layered BN sheets are stacked in an eclipsed ABAB ... sequence with boron eclipsed by nitrogen and vice versa. In h-BN, the π-bonding orbital's which constitute the VB are dominated by the p_z orbitals of higher electronegative N atoms. This tends to localize electrons of h-BN at the N atoms and produce a corresponding deficiency at the B atoms. As a consequence, π-bonding orbitals in h-BN are more bonding and antibonding orbitals are more

antibonding compared to those in graphite giving rise to a large band-gap of ~ 5 eV.[4,8,9] There are no non-bonding or nearly non-bonding orbitals in h-BN and hence

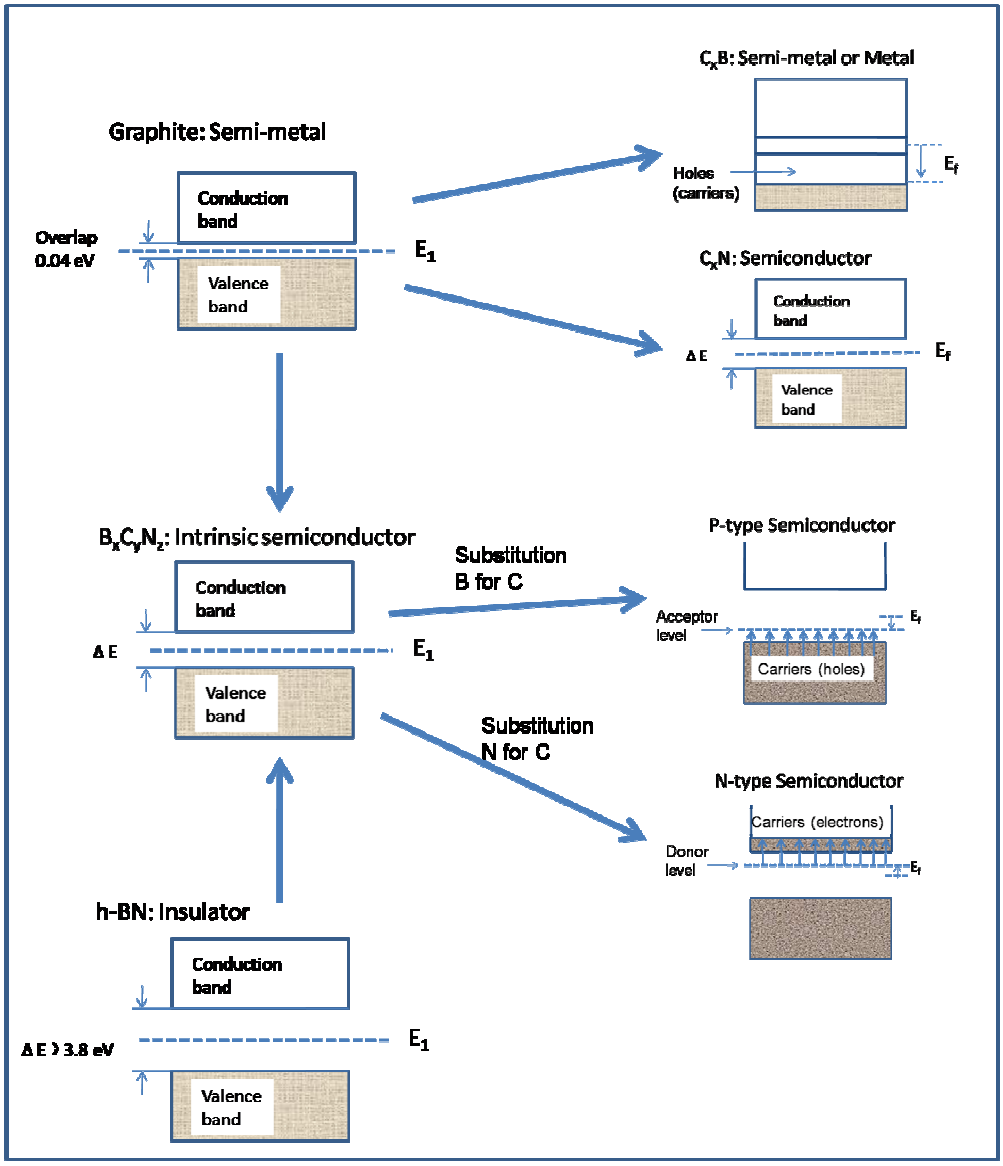

Figure 4.1: The expected band structure of BCN materials (Adopted from reference 4).

the large band-gap. The similar atomic radii and neighbouring position in the periodic table of boron, carbon and nitrogen allow hybridization between graphite and h-BN.[1,2,4] The hybridization makes $B_xC_yN_z$ materials wealthy with various

interesting properties and potential applications that lie in between those of graphite and h-BN.

Based on the composition and atomic arrangment, several types of semiconductors are possible in the case of $B_xC_yN_z$ materials, as shown in the schematic in Figure 4.1. $B_xC_yN_z$ is an intrinsic semiconductor which can be converted to a p-type or n-type extrinsic semiconductor by partial replacement of carbon with boron or nitrogen, respectively. The composition and the atomic configuration in the layers can also tune the band gap of $B_xC_yN_z$ materials. The structurally undefined film of composition $B_{0.35}C_{0.30}N_{0.35}$ deposited by the reaction

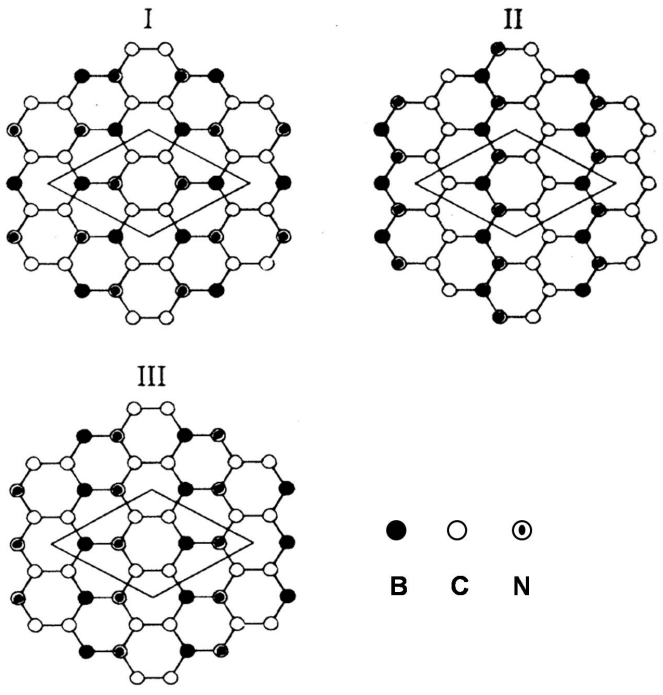

Figure 4.2: Three structural model of BC_2N (from reference 11).

of BCl_3, C_2H_2 and NH_3 at 973 K was found to have a room temperature conductivity of $\sigma = 6 \times 10^{-4}$ S/cm.[2] The logarithm of the conductivity vs inverse of the absolute temperature curve of this sample decreases linearly, leading to a thermal band-gap of

0.2 eV. Another $B_xC_yN_z$ material of similar composition, prepared by the CVD reaction of CH_3CN with $BC1_3$ in H_2 and N_2 atmosphere, behaved quite differently, with σ = 1.28 S/cm and a band-gap of 2 x 10^{-2} eV.[10] The different behaiviour of conductivity of a similar $B_xC_yN_z$ composition could be due to a different arrangement of the B, C and N atoms. Liu et al. proposed three possible atomic arrangements for BC_2N film as shown in Figure 4.2.[11] It was found that model II and III are semiconducting with indirect band gaps of 1.6 and 0.5 eV, respectively, while model I is a metal. The band gap of BC_2N films was also measured experimentally to be either 2.1 or 1.4 eV depending on the measurement method.[11]

The potential applications of $B_xC_yN_z$ materials based on its physical and chemical properties are shown in Table 4.1. While the semiconducting properties of $B_xC_yN_z$ could be widely utilised for applications like luminescence, photoenergy conversion, transistors and sensors,[3] the excellent intercalation properties could be useful as host material for Li batteries,[3,12] molecular sieves, gas storage and catalysis.[4] Nanomaterials of $B_xC_yN_z$ are expected to exhibit new properties and applications different from their bulk counterparts due to their nanometre size and unique structure.

The discovery of carbon nanotubes (CNTs)[13] were followed by a series of new nanomaterials with unique structure and properties. These new nanomaterials include BN nanotubes (BN-NTs),[14-17] carbon nitride nanotubes (CN-NTs)[18-21] and boron carbon nitride nanotubes (BCN-NTs).[22-25] Carbon nanotube can behave either as a semiconductor or a metal depending on its radius and chirality,[26-28] which displays a fascinating future for its nanodevice application. However, technologically it is still difficult to control the chirality and diameter of the CNTs.

Table 4.1: The potential applications of $B_xC_yN_z$ materials based on its physical and chemical properties

Expected properties	Potential applications
Semiconductivity Luminescence Photoluminescence Cathodohminescence Electroluminescence	Light-emitting materials
Thermoelectricity	Thermoelectric conversion materials
Rectification (p-n junction)	Transistors working at high temperature, light-emitting diodes, sensors
High conductivity	Lightweight electrical conductors
Intercalation	Electrode matrix for secondary lithium batteries, molecular sieves catalysts
Lubrication	High-temperature lubricant
Neutron absorption	Deceleration materials for nuclear reactors

On the contrary, nanomaterials of $B_xC_yN_z$ offer a large variety of mutually complementary electronic properties.[29-31] The $B_xC_yN_z$ nanotube possesses a band gap intermediate between those of BN nanotubes and C nanotubes, which can be controlled by changing their atomic compositions and arrangements. Due to the tailorable electronic properties, $B_xC_yN_z$ nanostructures are expected to play important roles in nanoelectronics.

4.2 Scope of the present investigations

Several efforts were carried out to prepare $B_xC_yN_z$ materials with different compositions. One of the objectives of such studies is to tune and alter the properties

of graphite through doping with a suitable element such as boron and nitrogen.[4] Various methods were employed to deposit $B_xC_yN_z$ films on solid substrates including CVD,[32,33] laser ablation,[34,35] ion beam assisted deposition[36] and magnetron sputtering.[37-39] A crystalline composition of B_4CN_4 is reported to occur on direct nitridation of B_4C with nitrogen in the 1873 to 2523 K range.[40,41] Amorphous B_4CN_4 was obtained by the pyrolyzation of a xerogel consist of B-trichloroborazene and bis(trimethylsilyl)carbodiimide.[42,43] Attempts have been made to prepare high surface area BCN by heating mesoporous carbon with B_2O_3 at high temperature in a nitrogen environment.[44] Porous carbon materials doped with boron and nitrogen are reported to be formed by the pyrolysis and carbonization of gels containing boric acid and citric acid in a nitrogen atmosphere,[45] the compositions varying between $BC_{16}N$ and BC_6N. A solid with the composition of BC_4N seems to be formed on the thermal decomposition of the BH_3-C_5H_5N complex at high temperatures.[46] Nitridation of boric acid and carbonization of saccharose in molten urea is reported to give a material with the bulk composition of BC_4N, but the material was not adequately characterized with respect to composition and properties.[47]

Similarly, the fascinating properties of carbon nanotubes[13] gave enormous impetus to researchers to explore nanotube morphology of $B_xC_yN_z$ materials. Stephen et al,[22] first reported carbon nanotubes containing B and N prepared through a modified electric arc-discharge method which turns out to be a mixture with graphite, boron and nitrogen. By a similar procedure, Suenaga et al,[48] produced $B_xC_yN_z$ nanotubes with well-separated layers of BN and carbon. Redlich et al,[24] synthesized $B_xC_yN_z$ nanotubes having a BC_2N outer shell and a carbon inner shell by the arc-discharge method. Nanotubes of outer BC_7N layers and pure carbon

inner layers have been obtained by laser ablation using a composite of BN and carbon as the target in the presence of nickel and cobalt.[49] Rao et al,[18] prepared $B_xC_yN_z$ nanotubes of varying compositions of carbon and nitrogen by the pyrolysis of BH_3-trimethylamine adduct. A template based approach has also been reported to prepare $B_xC_yN_z$ nanotubes using graphitic carbon nanotubes and carbon nitride nanotubes.[50,51] Single walled carbon nanotubes doped with B and N have also been prepared by a hot filament method.[52] Multiwalled nanotubes of the composition B_5CN_5 have been produced by chemical vapor deposition along with nanotubes containing BN layers sheathed with outer carbon layers.[53] While the arc-discharge and laser ablation methods have drawbacks in controlling phase separation and the diameter of the nanotubes, the template based method has the limitation in extending the diameter of the $B_xC_yN_z$ nanotubes beyond 20 nm. Furthermore, the surface of pristine carbon nanotubes is generally not reactive. In the present study, we have employed amorphous carbon nanotube (a-CNT) brushes[54] prepared by the decomposition of glucose as starting materials to prepare the $B_xC_yN_z$ nanotube brushes. We have introduced boron and nitrogen in a-CNTs by the high temperature reaction of a-CNT with boric acid-urea mixture. Interestingly, the nanotubes obtained by us, with the composition BC_4N are nonmagnetic insulators. To our knowledge, BC_4N nanotubes have not been investigated hitherto.

As the reaction of amorphous carbon nanotubes with boric acid and urea yields BC_4N nanotubes with interesting properties, it was our desire to find a means of carrying out a large scale synthesis of BC_4N with desirable properties. In order to accomplish this, we made use of amorphous carbon spheres, obtained from the hydrothermal treatment of glucose, as the starting material.[55] By the reaction of the carbon spheres with boric acid and urea at high temperature we obtained bulk

quantities of BC_4N with interesting properties. BC_4N is found to be a ceramic with high thermal stability, containing both micro and mesopores.

4.3 Experimental and related aspects

4.3.1 Synthesis of BC_4N nanotube brushes

Amorphous carbon nanotubes

Amorphous carbon nanotube (a-CNT) brushes were prepared by the following procedure.[54] Polycarbonate membranes with a pore diameter of 220 nm and 50 nm were soaked in 22 mL of 0.5 M aqueous solution of glucose in a 25 mL Teflon-lined autoclave. The temperature of the autoclave was maintained at 453 K for 6 h after which it was allowed to cool to room temperature. The brownish liquid found in the autoclave was discarded. The membranes that had turned brown due to formation of a-CNT were washed several times with deionized water and ethanol and then dried at 313 K for 1 h. The so obtained a-CNT brushes were used as the starting material for the synthesis of BC_4N nanotube brushes.

BC_4N nanotube brushes

A mixture of boric acid (1g) and urea (11.8 g) was dissolved in 40 mL of distilled water and heated at 343 K until the solution became viscous; the a-CNTs were soaked in it for nearly 2 h. They were later separated physically and dried in air at 313 K for overnight. The dried samples were thermally treated at 1243 K, 3 h for 40 nm nanotubes and 12 h for larger diameter (170 nm) nanotubes, and then cooled down to room temperature. The products were subsequently heated in NH_3 atmosphere at 1323 K in case of 170 nm nanotubes and 1173 K in case of 40 nm nanotubes for three hours to give black-coloured boron-carbon-nitride nanotube

brushes. The products were investigated by transmission electron microscopy and other physical techniques.

Coating of BC_4N brushes with metal nanoparticles

In order to obtain Au/Pt nanoparticles-covered BC_4N nanotube brushes, the nanotubes obtained by the method described earlier, were soaked in 2 mL of 5 mM aqueous solutions of hydrogen hexachloroplatinate (IV) or hydrogen tetrachloroaurate (III) for 12 h. The nanotubes were washed twice with distilled water followed by a washing with 10 mM sodium borohydride solution before drying at 313 K for an hour. The resulting products were examined by electron microscopy.

4.3.2 Synthesis of BC_4N micro-spheres

Amorphous carbon spheres

Amorphous carbon spheres were prepared by hydrothermal treatment of a saturated solution of glucose.[55] In a typical procedure, an aqueous solution of glucose (50 mL, 0.5 M) was sealed in a 50 mL Teflon-lined autoclave and heated to 453 K for 6 hours. The resulting black colored solution was centrifuged to obtain a solid that was washed with ethanol for several times by using sonication and centrifugation. The dark brown solid obtained as the final product after oven drying at 323 K for 12 h was found to contain carbon spheres. This material was used as the starting material for the synthesis of BC_4N spheres.

Mesoporous BC_4N micro-spheres

A mixture of boric acid (0.4 g), urea (4.7 g) and amorphous carbon spheres (1 g) in distilled water (40 mL) was heated to 333 K until the solution became viscous. The

product was separated by centrifugation and dried in air at 313 K for overnight. The dried sample was thermally treated at 1203 K for 10 h in a nitrogen atmosphere and cooled to room temperature. The product was subsequently heated in an NH_3 atmosphere at 1273 K for three hours to give black-colored BC_4N spheres.

4.3.3 Characterization techniques

X-ray diffraction (XRD): XRD patterns of the nanotubes were recorded at 298 K with a Rich-Siefert 3000-TT diffractometer employing Cu Kα radiation.

Scanning Electron Microscope: The morphology of the nanotubes was examined by a Field Emission Scanning Electron Microscope (FESEM, FEI Nova-Nano SEM-600, Netherlands), and Scanning Electron Microscope (SEM) Leica S-440I instrument (U.K).

Transmission Electron Microscope: TEM images were recorded with a JEOL JEM 3010 instrument (Japan) operated at an accelerating voltage of 300 kV.

X-ray Photoelectron Spectroscopy (XPS): X-ray photoelectron spectroscopy measurements were performed using ESCALAB MKIV spectrometer employing Al Kα radiation (1486.6 eV).

Electron Energy Loss Spectra (EELS): Electron energy loss spectra (EELS) were recorded with a transmission electron microscope (FEI, TECNAI F30) equipped with an energy filter for (EELS) operating at 300 kV.

Raman spectra: Raman spectra were recorded with a LabRAM HR with 633 nm line from HeNe laser.

Thermogravimetric analysis: Thermogravimetric analysis was carried out by using a Mettler Toledo Star system.

Gas adsorption: Nitrogen adsorption-desorption isotherms were measured at liquid N_2 temperature 77 K) using QUANTACHROME AUTOSORB-1C surface area

analyzer. The surface area was obtained by using the BET method. The CO_2 adsorption was carried out at 195 K (1:1 mixture of dry ice and acetone). Hydrogen adsorption was carried out at liquid nitrogen temperature (77 K).

Magnetization measurements: Magnetization measurements were carried out with a vibrating sample magnetometer in a physical property measuring system (PPMS,Quantum Design, San Diego, CA, USA).

4.4 Results and Discussion

4.4.1 BC_4N nanotube brushes

Figure 4.3 (a) shows a FESEM image of the amorphous carbon nanotubes (a-CNT). These nanotubes having a length of around 15 µm are well-aligned in a brush-like morphology. The TEM image in Figure 4.3 (b) shows the outer diameter of the a-CNT to be around 250 nm with a wall thickness of ~ 50 nm.

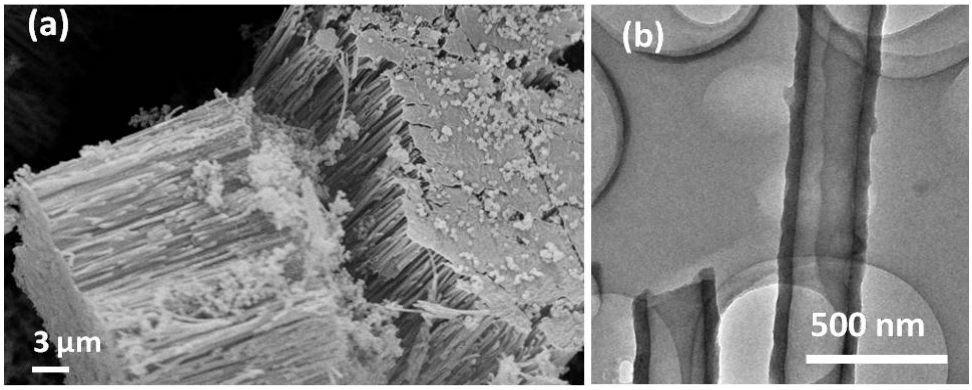

Figure 4.3: (a) FESEM Image of amorphous carbon nanotube brushes. (b) TEM Image of amorphous carbon nanotubes

The reaction of a-CNT brushes with the H_3BO_3–urea mixture yields a nanotube structure as shown in Figure 4.4 (a). These nanostructures containing B, C and N replicate the brush-like morphology of the a-CNTs. The diameter of the $B_xC_yN_z$

nanotubes is ~ 170 nm and the lengths are 15 µm. The higher magnification FESEM image in Figure 4.4 (b) shows the open ends of the $B_xC_yN_z$ nanotubes demonstrating the wall thickness to be around 50 nm. This is further supported by the TEM image of a single nanotube shown in Figure 4.4 (c). The selected area electron diffraction pattern shows faint rings with a few spots. The XRD pattern of the $B_xC_yN_z$ nanotube brushes (Figure 4.5 (a)) shows broad reflections with d spacing's of 3.43 Å and 2.13 Å corresponding to (002) and (100) planes respectively (JCPDS card: No. 35-1292).

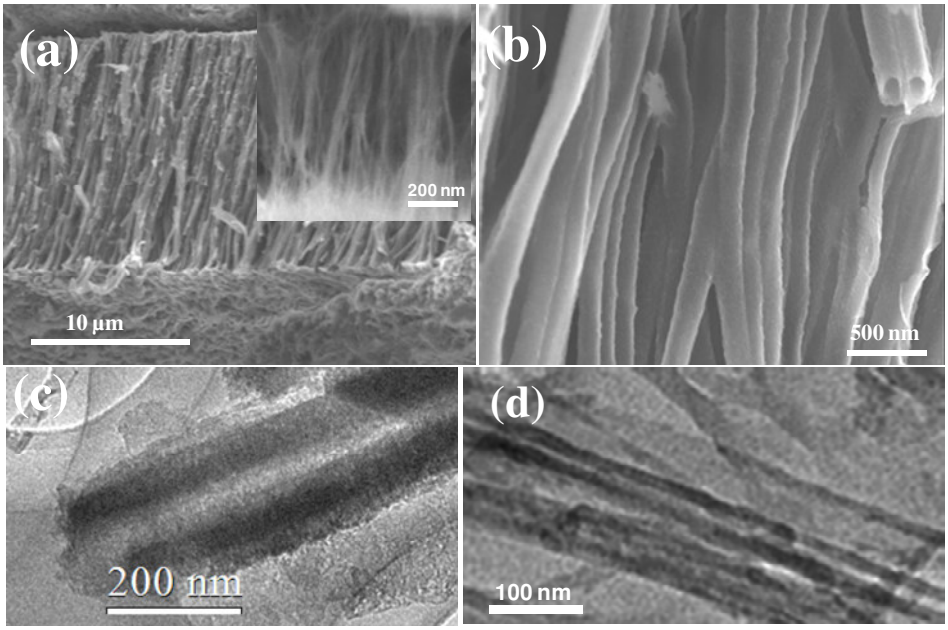

Figure 4.4: (a) FESEM image of BC_4N nanotube brushes with an average diameter of around 170 nm. Inset shows a FESEM image of BC_4N nanotube brushes of diameter 40 nm. (b) Higher magnification FESEM image of BC_4N nanotube brushes (170 nm). TEM image of BC_4N nanotubes (c) 170 nm diameter (d) 40 nm diameter.

The broad reflections in the XRD pattern and the diffused rings in electron diffraction pattern are similar to that reported earlier for the other preparations of $B_xC_yN_z$ materials.[4,41,47] We have also prepared a-CNTs of smaller size by using a polycarbonate membrane with a pore size of 50 nm. Using these a-CNTs, we have

been able to obtain $B_xC_yN_z$ nanotube brushes of smaller diameter. FESEM image of the $B_xC_yN_z$ nanotube brushes of smaller diameter is shown in the inset of Figure 4.4 (a). The TEM image in Figure 4.4 (d) reveals the diameter of these $B_xC_yN_z$ nanotubes to be around 40 nm, having a wall thickness of 12 nm.

The Raman spectra of the $B_xC_yN_z$ nanotubes were recorded with the 633 nm line from a HeNe laser. The spectra are shown in Figure 4.5 (b). The observation of two strong peaks at 1324 cm^{-1} and 1600 cm^{-1} in the Raman spectra are the signatures of D band and G bands of $B_xC_yN_z$ nanotubes.[56,57] The D bands are somewhat broad probably due to the disorder in the $B_xC_yN_z$ layers. The additional peak at around 800 cm^{-1} is similar to that found in BN nanotubes. The band around 2600 cm^{-1} may be due to the combination of D + G band or 2D overtone. Such bands have been observed in $B_xC_yN_z$ nanotubes of other compositions.[56,57]

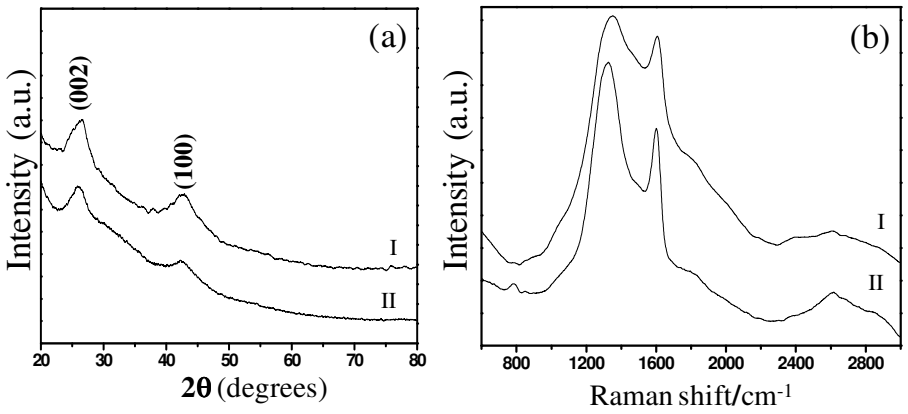

Figure 4.5: (a) XRD patterns and (b) Raman spectra of BC_4N nanotube brushes. (I) 40 nm diameter (II) 170nm diameter.

X- ray Photoelectron spectra of the $B_xC_yN_z$ nanotubes in the N, C and B (1s) regions are shown in Figure 4.6. We can analyze these data on the lines suggested by Kim et. al.[53] The N 1s spectrum of the $B_xC_yN_z$ nanotube brushes in Figure 4.6 (a) shows peaks at 397.7, 400.2 and 401.5 eV. The peak at 397.7 eV

corresponds to nitrogen bonded to boron (N–B bond), peak at 400.2 eV corresponds to nitrogen bonded with carbon in graphite like N–C structure, and the peak at 401.5 eV signifies N bonded to C in a pyridine type structure. The C 1s spectrum in Figure 4.6 (b) has two peaks with a broad shoulder. The peak at 284 eV is assigned to carbon bonded with boron atoms (C-B bond) and the peak at 286 eV corresponds to a carbon bonded to another carbon atom (C-C bond). The long tapering band extending from 286 to 289 eV is ascribed to carbon atoms bonded to nitrogen. The B 1s spectrum in Figure 4.6 (c) has two peaks centered at 191.2 and 194 eV, with a

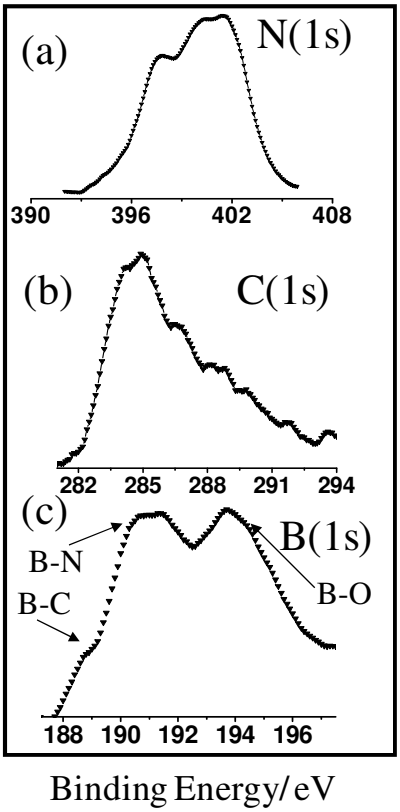

Figure 4.6: XPS of the BC_4N nanotube brushes

shoulder at 189.2 eV. The shoulder at 189.2 eV corresponds to boron bonded to carbon (B-C bond), and the peak at 191.2 eV is due to boron bonded to nitrogen (B-N bond). The peak at 194 eV is assigned to boron bonded to oxygen (B-O bond),

probably arising from the excess B_2O_3. By subtracting the contribution of the B-O part from the B 1s signal, we have estimated the composition of the nanotubes taking the capture cross sections into account. Such an analysis gave the approximate composition of the $B_xC_yN_z$ nanotube brushes to be $BC_4N_{1.5}$.

In order to obtain a more reliable elemental analysis, we have carried out electron energy loss spectroscopy (EELS) measurements on the K-edge absorption for B, C and N in a high-resolution electron microscope. The spectrum clearly shows K-shell ionization edges at 188, 284 and 401 eV for B, C and N respectively. Each core edge fine structure consists of a sharp π* peak and a well-resolved σ* band, characteristic of sp^2 hybridization.[30,53] The percentage of B and N were significantly smaller than that of carbon. EELS measurements gave an average chemical composition to be BC_4N for these nanotubes. In Figure 4.7, we show the elemental mapping of the nanotubes the red, green and blue colours representing boron, carbon and nitrogen respectively. We see that atoms are randomly distributed across the

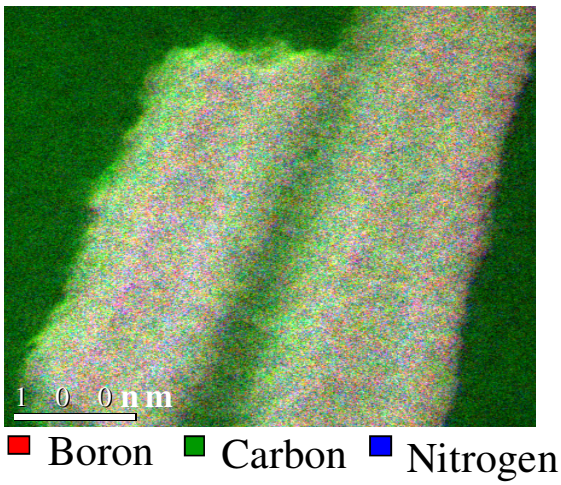

Figure 4.7: Elemental mapping of Boron, Carbon and Nitrogen of BC_4N nanotubes obtained from EELS

nanotubes, suggesting that the nanotubes are homogeneous with a uniform distribution of B, C and N atoms. The homogeneous nature of the BC_4N nanotubes is

also confirmed by the fact that we failed to obtain BN nanostructures after removal of carbon from the BC_4N nanotubes by oxidation.[58]

Reaction between H_3BO_3 and urea, a main synthesis route for pure BN has been well studied earlier.[59,60] In a similar reaction, addition of amorphous carbon to the mixture of H_3BO_3 and urea yields BC_4N, on two-phase of heating. The initial reactions involved in the formation of BC_4N are the dehydration of H_3BO_3 and decomposition of urea.

$$2B(OH)_3 \xrightarrow{\triangle} B_2O_3 + 3\,H_2O$$

$$CO(NH_2)_2 \xrightarrow{\triangle} NH_3 + HNCO$$

The overall stoichiometric reaction for the formation of BC_4N may be written as,

$$B_2O_3 + 2NH_3 + 8C \xrightarrow{\triangle} 2BC_4N + 3H_2O$$

We have carried out thermogravimetric analysis of BC_4N nanotubes in air. These nanotubes show high thermal stability and no weight loss was observed up to 1173 K (Figure 4.8). Amorphous carbon nanotubes get completely oxidized before 1023 K. The high thermal stability of BC_4N nanotubes is noteworthy.

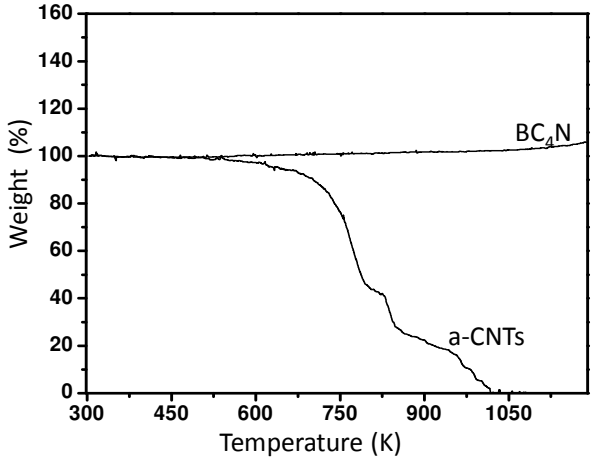

Figure 4.8: TGA of BC_4N nanotubes and a-CNT

In the literature, there have been theoretical papers describing magnetism of $B_xC_yN_z$ nanotubes. $B_xC_yN_z$ nanotubes having an approximate composition of BC_2N

have been predicted to be ferromagnetic.[61] Such itinerant ferromagnetism has also been predicted in C-BN heterostructured nanotubes.[62] $B_xC_yN_z$ ribbons of the composition $BC_{10}N$ have been predicted to be ferrimagnetic.[63] Carbon doping in BN nanotube is supposed to induce spontaneous magnetism.[64] The magnetic susceptibility measurement on BC_4N nanotube brushes shows that they are nonmagnetic. They show a very small magnetic moment (0.22 μ_B) probably due to defect in the nanotubes. The BC_4N nanotubes are highly insulating, the resistivity being in the mega-ohm region.

Adsorption properties of materials are of importance in catalysis, gas storage, selective gas recognition and separation. Zeolites and metal-organic frameworks have enjoyed high utility in gas adsorption because of the high surface area, and well defined pore shapes. We have measured the surface area of the as synthesized BC_4N nanotube brushes using nitrogen adsorption-desorption isotherms performed at 77 K

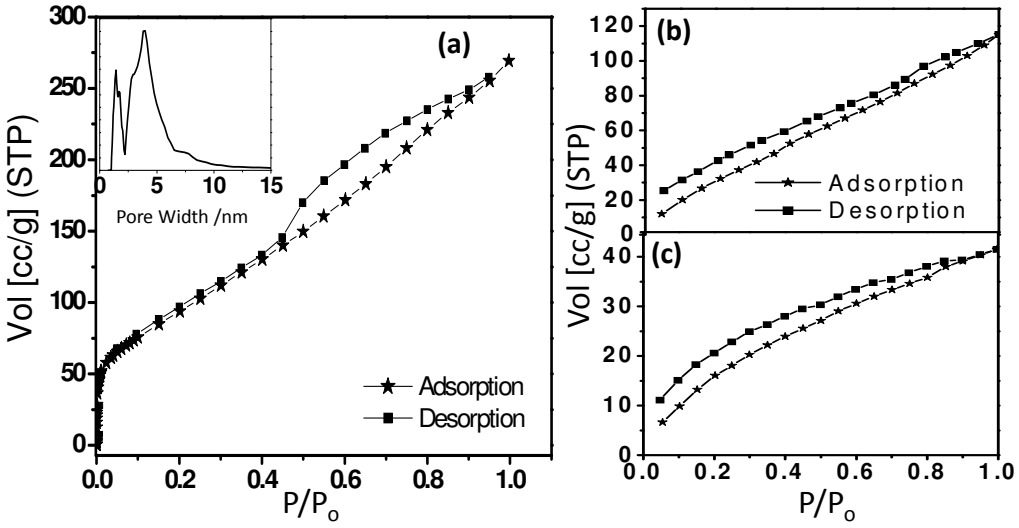

Figure 4.9: Adsorption - desorption isotherm of (a) N_2 at 77 K (Inset shows the pore size distribution) (b) CO_2 at 195 K and (c) H_2 at 77 K of BC_4N nanotube brushes

(Figure 4.9 (a)). The surface area measured by Brunauer, Emmett and Teller (BET) method was 356 m^2/g with contributions from both micropores (0.7 nm) and mesopores (4 nm) as can be seen from the inset in Figure 4.9 (a). The CO_2 adsorption on the BC_4N nanotube brushes was measured at low pressures and low temperature at 195 K. The BC_4N nanotube brushes showed remarkably high CO_2 uptake of about 23.5 wt % (Figure 4.9 (b)). The adsorption does not exhibit saturation even at $P/P_o = 1$, indicating the presence of unoccupied pores available for further uptake. The adsorption of hydrogen on the BC_4N nanotubes was only 0.4 wt % at 77 K (Figure 4.9 (c)). Thus, the BC_4N nanotubes prepared by us are selective adsorbents of CO_2. New materials having selective adsorption for CO_2 are important for environmental and industrial applications. Millward and Yaghi[65] have studied CO_2 adsorption by various metal-organic frameworks (MOF) and reported the highest value of adsorption (33.5 mmol/g) in the case of MOF-177 at ambient

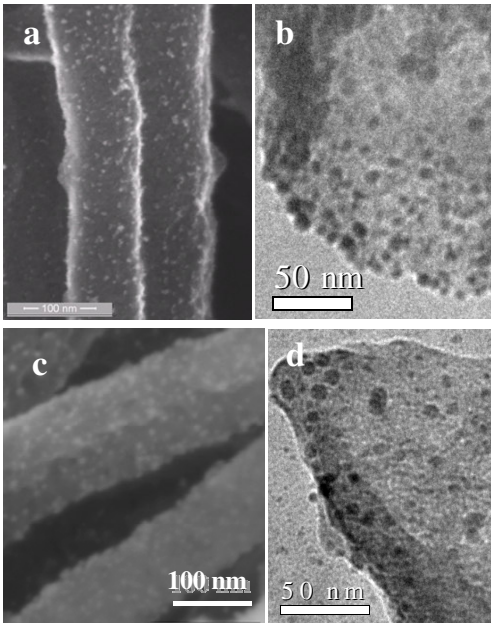

Figure 4.10: (a) FESEM image (b) TEM image of Pt decorated BC_4N nanotubes. (c) FESEM image (d) TEM image of Au decorated BC_4N nanotubes.

temperature and high pressures. Among the zeolites, the highest reported value of CO_2 adsorption is 7.4 mmol/g for Zeolite 13X at high pressure and room temperature.[66] Sudik et al,[67] measured CO_2 adsorption at 195 K and low pressure in certain iron carboxylate MOFs and reported highest CO_2 uptake for IRMOP-51 of 74 $cm^3(STP)/cm^3$.

In Figure 4.10 (a) and (c), we show the FESEM images of BC_4N nanotubes decorated with Pt and Au nanoparticles, respectively. We see a uniform distribution of nearly monodispersed metal nanoparticles on the nanotube walls. The size of the metal nanoparticles is in the range of 3-8 nm as found from the TEM images in Figure 4.10 (b) and (d). Such metal nanoparticle decorated BC_4N nanotubes could have useful applications.

Prof. U. V. Waghmare, Prof. Swapan. K. Pati and Dr. Mousumi Upadhyay-Kahaly have carried out first-principles density functional theory based calculations to understand the structure and properties of BC_4N nanotubes. A supercell of 72-atoms [$(BN)_{12}C_{48}$] have been used to facilitate comparison of energies of different structures of BC_4N nanotubes. Four types of ordering of B and N atoms on the carbon sites of a (6,6) carbon nanotube (CNT) have been considered for the calculations (see Figure 4.11). In the first structure (S_1), one C–C bond is replaced with a B–N bond in each hexagonal ring. In the second structure (S_2), local structural units of BN_3 and NB_3 are substituted in a CNT, with no linkage between them. In the structure S_3, these local structural units (BN_3 and NB_3) are link together with a B–N bond. Finally, a disordered structure (D) has been considered.

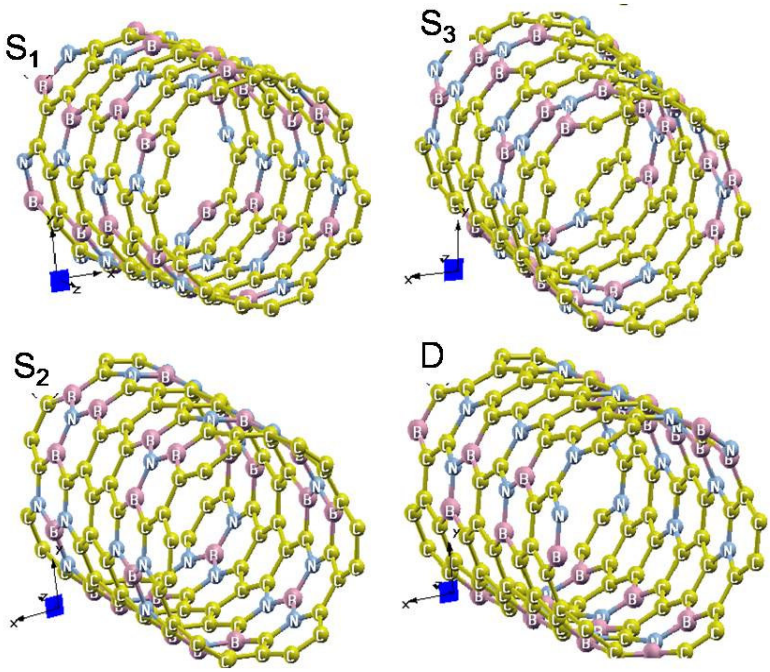

Figure 4.11 (6,6) BC_4N nanotubes: (S_1) an ordered structure, with one B–N bond present in each carbon ring, (S_2) anther ordered structure, where BN_3 and NB_3 units are distributed on alternate C_6 rings, (S_3) an ordered structure, in which BN_3 and NB_3 units are linked with one B–N bond and (D) a disordered structure, in which carbon atoms occupy B and N sites in a BNNT randomly with a probability of 2/3.

Relative energies (see Table 4.2) of these BC_4N nanotubes clearly show that BN_3 and NB_3 local units are energetically more favourable (S_2 is more stable than S_1 by almost 130 meV per B–N bond) than the diatomic BN units. The S_2 structure is further stabilized by almost 73 meV per atom through a B–N linkage between BN_3 and NB_3 local units to yield S_3. The disordered configuration D, which is consists of different types of local structural units (BN, BN_3, NB_3, BN_2, etc), has a stability intermediate to S_1 and S_2 structures. The electronic structure of the BC_4N nanotubes has been examined through their density of states. The S_3 BC_4N nanotube is found to exhibits a gap of about 1 eV in its electronic structure.

Table 4.2: Relative energies of (6,6) BC_4N nanotubes

Nanotube	Energy (eV/atom)
D	0.100
S_1	0.139
S_2	0.073
S_3	0.00

First-principles calculations have also been carried out on (6,0) and (8,0) nanotubes. The (6,0) carbon nanotube is found to be metallic as expected, but the (6,0) nanotube with the S_3 structure where BN_3 and NB_3 units are linked show a semiconducting gap. For an (8,0) carbon nanotube, the semiconducting gap is found to be 0.33 eV, while for the BC_4N (8,0) nanotube (with BN substitution in every hexagonal ring) it increases to 0.40 eV.

4.4.2 BC_4N microspheres

Amorphous carbon spheres prepared[55] by the hydrothermal treatment of aqueous glucose solution were used as the starting material for the synthesis of $B_xC_yN_z$. FESEM image of the carbon spheres is shown in Figure 4.12 (a). Diameters of these spheres were in the range of 150 nm to 500 nm A TEM image of a typical carbon sphere is shown in Figure 4.12 (b). The image reveals the smooth surface of the sphere. The BET surface area of these carbon spheres was 85 m^2/g. Reaction of the carbon spheres with urea and boric acid at 1203 K gave a product containing B, C and N. The product consisted of spherical particles as shown in the FESEM image in Figure 4.12 (c), diameters of these spheres remaining in the 150-500 nm range. From the TEM image in Figure 4.12 (d), we see that unlike the smooth surface of

carbon spheres, the $B_xC_yN_z$ spheres show contrast variations originating from the presence of pores at the surface with uneven depth.

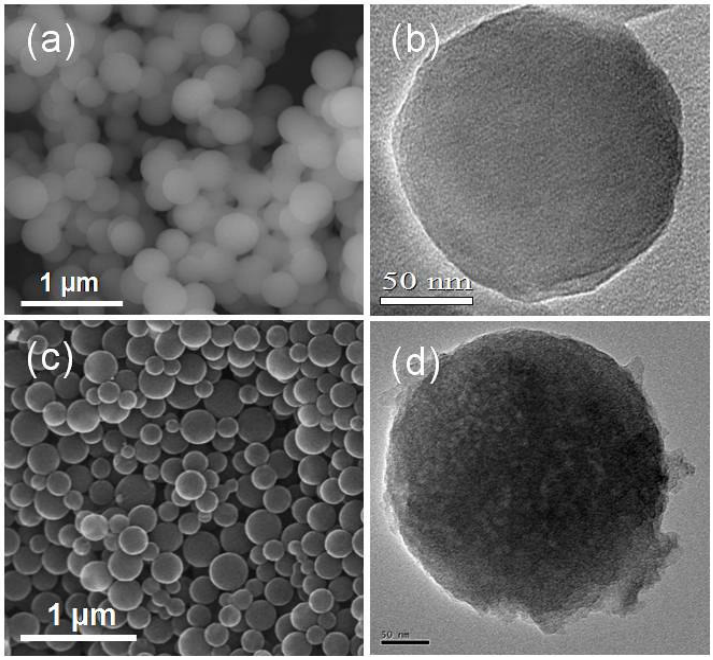

Figure 4.12: (a) FESEM image and (b) TEM image of carbon spheres. (c) FESEM image and (d) TEM image of $B_xC_yN_z$ spheres.

XPS core level spectra of the $B_xC_yN_z$ product is shown in Figure 4.13. The C 1s spectrum shows a peak centred at 286 eV which can be deconvoluted into two bands at 283 and 287 eV. The band at 283 eV is assigned to carbon atom bonded to boron and the band at 287 eV ascribed to carbon atom bonded to another carbon and nitrogen atoms.[40,41,53,68,69] The N 1s signal can be deconvoluted into two bands at 399 and 400 eV, of which the former corresponds to nitrogen atom bonded to boron and the latter to nitrogen atom bonded to carbon.[40,41,53,69,70] The B 1s signal appears as a broad feature with shoulders on either side. This band can be deconvoluted into three bands centred at 188, 190 and 193 eV, of which the first two can be assigned to boron bonded to carbon and nitrogen respectively.[40,41,53,68,70] The weak feature at 193 eV is assigned to boron bonded to oxygen, probably arising from a small amount

of unreacted B_2O_3. Based on the capture cross sections and intensities of B, C and N signal in Figure 4.13, we estimated the composition to be $B_{1.4}C_4N$ or $B_4C_{12}N_3$. While the XPS-spectra of the product obtained in the present study look somewhat different

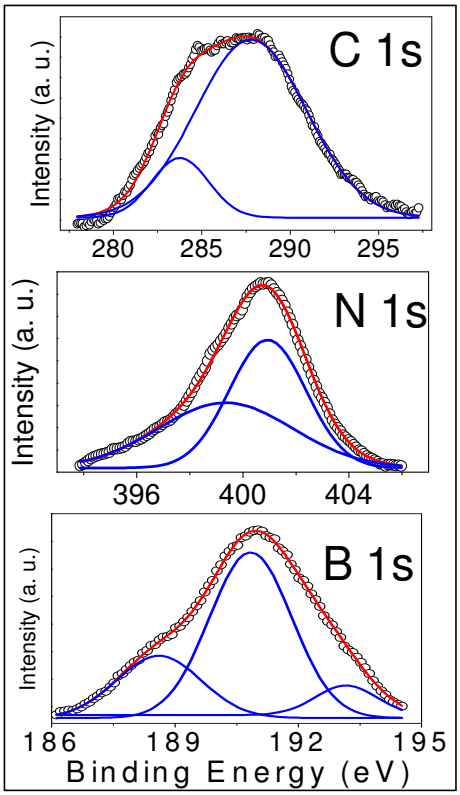

Figure 4.13: XPS of BC_4N spheres

from the corresponding spectra of the BC_4N nanotubes, the main features are comparable.

In order to establish the composition of the $B_xC_yN_z$ product, we have carried out electron energy loss spectroscopy (EELS) measurements on the K edge absorptions bands of B, C and N on the entire-sphere as well as different parts of the sphere in a high resolution transmission electron microscope. A representative spectrum in Figure 4.14 (a) shows the K-shell ionization edges around 188, 284 and 401 eV, characteristic of B, C and N respectively. Each core edge fine structure shows two peaks corresponding to the π^* and σ^* bands due to the sp^2

hybridization.[30,53] Based on the EELS data, we get an average chemical composition of $B_{1.4}C_{3.7}N$, which is consistent with the XPS results. This analysis corresponds approximately to BC_4N. In Figure 4.14 (b), we show an EELS map of a small portion of BC_4N sphere, the red, green and blue colours representing boron,

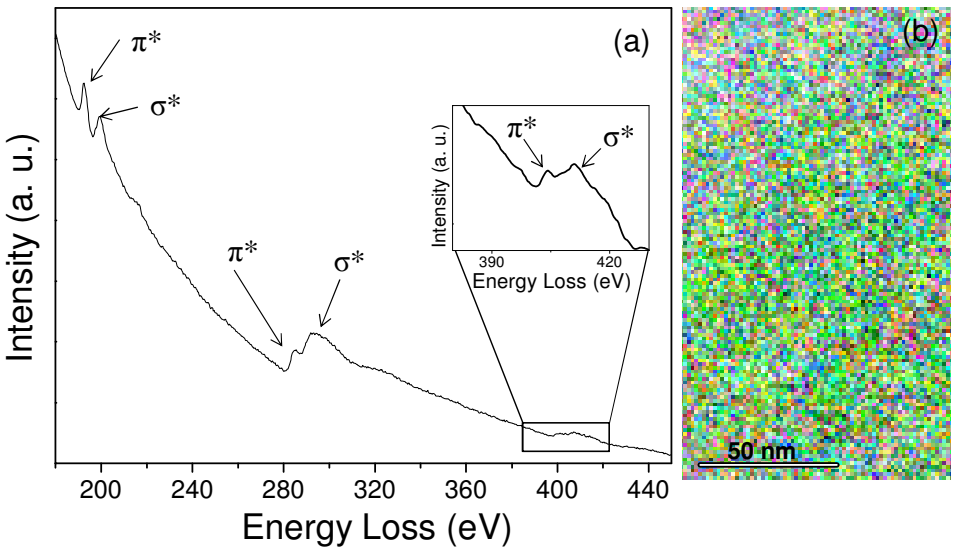

Figure 4.14: (a) EEL spectrum (inset core edge fine structure of nitrogen) and (b) EELS map of boron (red), carbon (green), and nitrogen (blue) of a small portion of a BC_4N sphere.

carbon and nitrogen atoms respectively. The colours are uniformly distributed suggesting a homogeneous nature of BC_4N. The random distribution of atoms throughout the sphere is more clear from the individual map of boron, carbon and nitrogen atoms as shown in the Figure 4.15. The homogeneity of BC_4N is also indicated by the fact that oxidation of BC_4N at 923 K in an oxygen environment does not yield BN as it was the found in the case of $B_xC_yN_z$ nanotubes with separate layers of BN and carbon.[58] The XRD pattern and Raman spectrum of BC_4N do not change significantly on oxygen treatment at high temperatures.

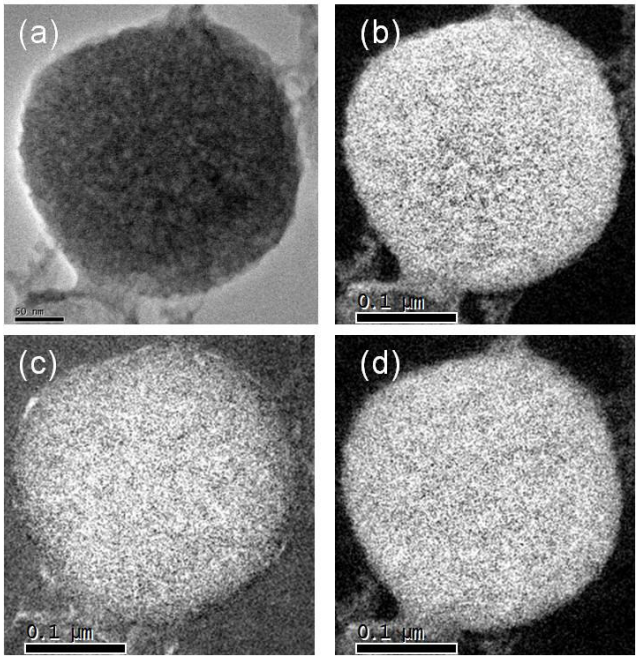

Figure 4.15: (a) TEM image, (b) boron map, (c) carbon map and (d) nitrogen map of a BC_4N sphere.

The XRD pattern of the BC_4N spheres in Figure 4.16 (a) shows two broad reflections with d spacing of 3.4 Å and 2.1 Å, corresponding to the (002) and (100) planes respectively. The pattern is similar to that reported earlier for $B_xC_yN_z$ materials with different compositions.[40,41,47] This XRD pattern is typical of

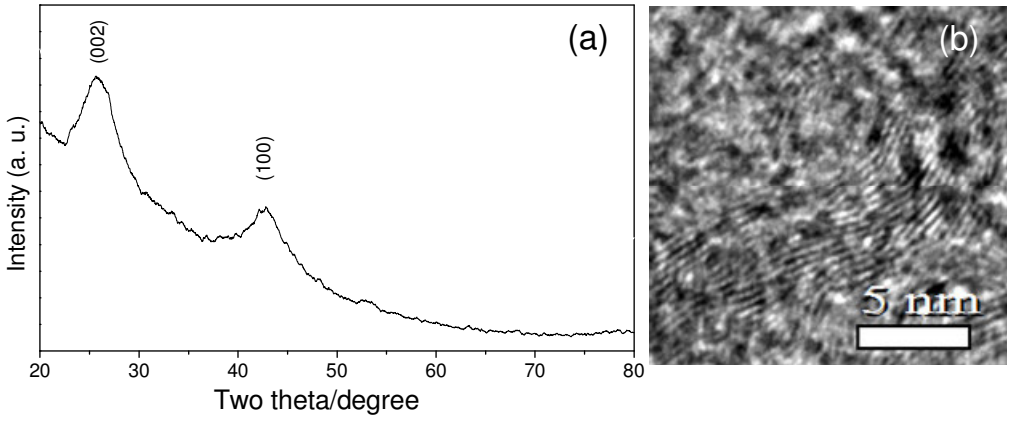

Figure 4.16: (a) XRD pattern of BC_4N spheres (b) HRTEM image of BC_4N spheres

materials with a graphite like structure with little or no sheet-to-sheet registry. The interlayer distance (d = 3.4 Å) of the BC_4N is slightly larger than that of graphite (3.33 Å) and h-BN (3.36 Å). In Figure 4.16 (b), we show a TEM image of BC_4N to reveal the presence of fragments of the layered structure. The Raman spectrum of BC_4N, recorded with the 633 nm line from a HeNe laser, shows two strong features at around 1324 cm^{-1} and 1600 cm^{-1}, which are assigned to the D and G bands as in $B_xC_yN_z$ and graphitic materials.[56,57] The broadness of the D band can arise from disorder in the layers.

In Figure 4.17, we have compared the thermogravimetric analysis curve of BC_4N with that of the starting carbon spheres recorded in air. The carbon spheres get completely oxidized before 1023 K just like other carbon materials. The BC_4N spheres, however, do not show any decomposition up to 1273 K. This feature of BC_4N is noteworthy.

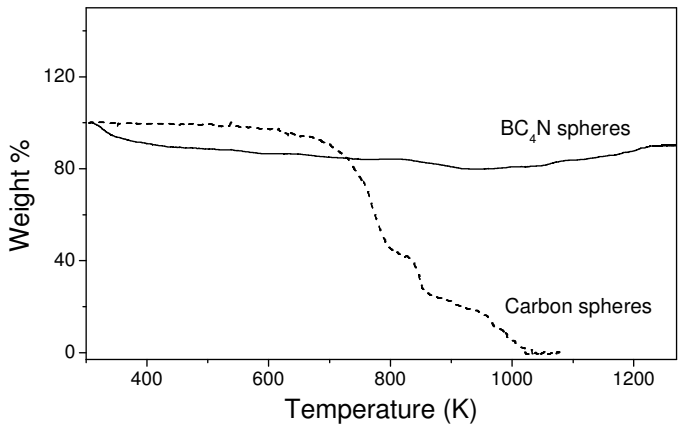

Figure 4.17: TGA of BC_4N spheres and carbon spheres

Nitrogen adsorption-desorption isotherms of BC_4N at 77 K are shown in Figure 4.18. The specific surface area of the BC_4N spheres by the Brunauer-Emmett-Teller (BET) method is 428 m^2/g. The isotherm shows type IV behaviour with a H3

type hysteresis loop (as per IUPAC classification), associated with capillary condensation of N_2 in the mesopores.[71] The sharp rise in N_2 adsorption at low relative pressures ($p/p_0 < 0.01$) indicates the presence of micropores in the material. The pore size distribution, calculated from the adsorption branch of the isotherms using DFT (density functional theory) model confirms the presence of both micropores (1.4 nm) and mesopores (2.8 nm and 4.5 nm) in the BC_4N spheres (see inset of Figure 4.18). The release of gaseous species during the high temperature reaction appears to be responsible for the meso and micro pores in the BC_4N spheres, which in turn give rise to the higher surface area. Thus, the BC_4N spheres prepared by us exhibit properties of a porous ceramic.

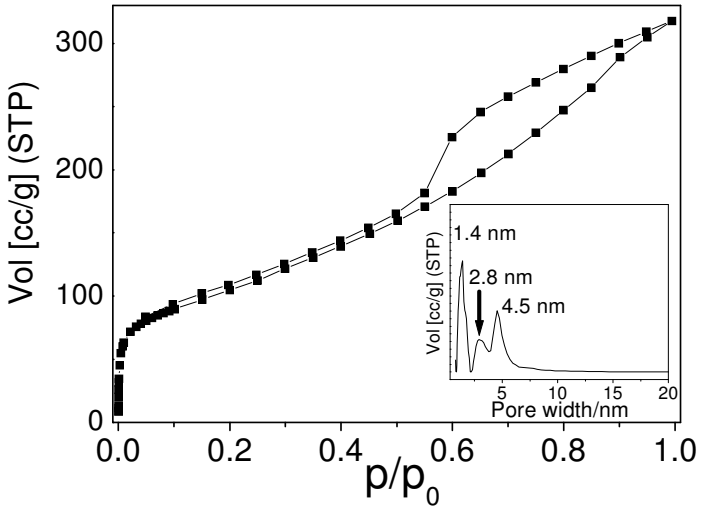

Figure 4.18: Nitrogen adsorption-desorption isotherm of BC_4N spheres (inset pore size distribution)

CO_2 adsorption of the BC_4N spheres measured at 298 K and 40 bar shows 9 wt% uptake (Figure 4.19 (a)). The CO_2 uptake, however, goes up to 40 wt% at 195 K and 1 atmosphere. The adsorption and desorption isotherms (Figure 4.19 (b)) follow exactly the same path, showing no hysteresis. The adsorption isotherm does not exhibit saturation even at $p/p_0 = 1$. We have carried out methanol adsorption

measurements on the BC_4N spheres at room temperature and low pressures. The BC_4N spheres adsorbed about 200 mL (28 wt%) of methanol at $p/p_0 = 0.9$. The H_2 adsorption isotherm of the BC_4N spheres at 77 K and 50 bar rises sharply and

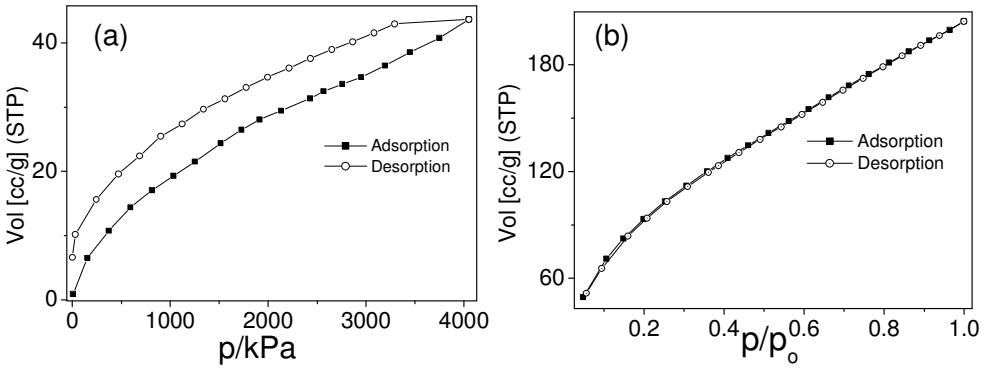

Figure 4.19: CO_2 adsorption-desorption isotherm of BC_4N spheres (a) at 298 K and 40 bar (b) at 195 K and 1 atm

reaches saturation at 10 bar, with 1.1 wt% of H_2 adsorption. At 77 K and 1 atmospheric pressure, the BC_4N spheres adsorb 0.8 wt% of H_2.

Prof. U. V. Waghmare, and Dr. K. P. S. S. Hembram have carried out first-principles density functional theory based calculations to understand the structure and properties of BC_4N. Four different structures of a BC_4N layer have been considered by substituting boron and nitrogen for one third of carbon atoms in the 6 × 6 unit cells (a supercell) of graphene. In Figure 4.20 (b), two such configurations (i) and (iv) are shown. While configuration (i) has a homogeneous distribution of boron and nitrogen, configuration (iv) has phase segregated regions of BN. The atomic positions and the periodic cell parameter of four configurations were relaxed to minimum energy. Figure 4.20 (a) shows energy as a function of lattice constant for all four configurations of BC_4N. From the cohesive energies (Table 4.3), it is clear that BC_4N layers are less stable than pristine graphene by -2.5 to -6 %. The

configuration (i) is 0.3 eV per atom higher in energy than that of configuration (iv). The configuration of the sample synthesized by us would depend on the kinetics and

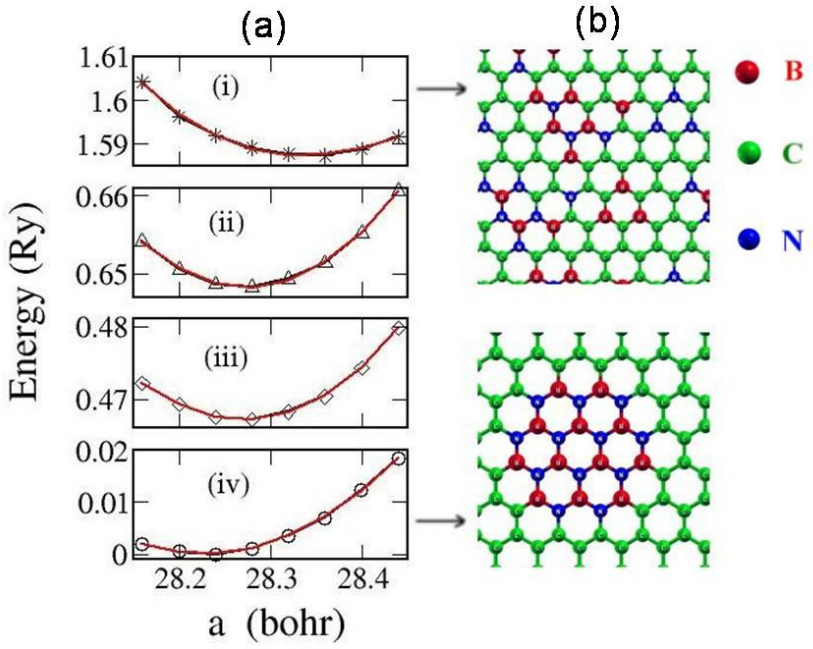

Figure 4.20: (a) Energy as a function of lattice constant of BC_4N for configurations with different ordering of B and N on carbon lattice. (b) Structures of configurations with the highest (top) and lowest energy (bottom) of the four. Note that the energies are of the whole supercell that contains 72 atoms.

Table 4.3 Lattice parameter (a), bulk modulus (B) and cohesive energy (E_{coh}) of graphene and BC_4N in different configurations.

Configuration	a (bohr)	B (GPa. m)	E_{coh} (eV/atom)
BC_4N (i)	28.36	1.81	8.63
BC_4N (ii)	28.28	2.06	8.81
BC_4N (iii)	28.28	1.66	8.84
BC_4N (iv)	28.24	1.61	8.93
Graphene	28.04	1.74	9.16

other experimental factors such as temperature. Configurational entropy would favour a homogeneous distribution of boron and nitrogen, as in configuration (i), which may be the most stable form if the samples are grown at high temperatures.

The electronic structure and bulk modulus of BC_4N is found to be sensitive to the ordering of boron and nitrogen. While a small gap of ~ 0.17 eV opens up in configuration (i), configuration (iv) exhibits a larger bandgap of 1.1 eV, this is due to the different on-site potentials felt on the two sub-lattices of graphene.

4.5 Conclusions

It has been possible to synthesize nanotube brushes of the composition BC_4N starting with amorphous carbon nanotubes prepared with the porous polycarbonate membranes. The reaction of the a-CNTs with a mixture of urea and boric acid provides an excellent means for the incorporation of boron and nitrogen in the carbon nanotubes. In the first step of the reaction, the decomposition of urea produces NH_3, which on reaction with boric acid at high temperatures enables the incorporation of boron and nitrogen in the carbon nanotubes. The BC_4N nanotubes have been characterized by various physical methods and the composition was established by XPS and EELS analysis. Although the nanotubes may not have an extended ordered structure with graphene type BC_4N layers but there is sufficient order to give X-ray diffraction pattern and a well-defined Raman spectrum. Surprisingly, BC_4N nanotubes have very high thermal stability. They are nonmagnetic insulators with a high propensity for CO_2 uptake (up to 23.5 wt%). First principle calculations indicate that the most stable structure may involve a graphitic network containing BN_3 and NB_3 units connected by a B–N bond.

It has also been possible to synthesize a ceramic of the composition BC_4N starting with amorphous carbon spheres, obtained from the hydrothermal treatment of glucose. The reaction of amorphous carbon spheres with urea and boric acid yields bulk quantities of BC_4N spheres. The boron, carbon, and nitrogen atoms are homogeneously distributed in the structure. BC_4N has a graphite type layered structure and gives an X-ray diffraction pattern and Raman spectrum expected of such a structure. Similar to BC_4N nanotube brushes, BC_4N spheres have high propensity for CO_2 uptake (up to 40 wt%) with high thermal stability. First-principles density functional theoretical calculations were used to compare the structure and properties of BC_4N and graphene. It is found that BC_4N is stable and its electronic structure and elastic modulus are sensitive to the ordering of boron and nitrogen atoms.

References

1. N. Bartlett and B. W. McQuillan, *Intercalation Chemistry* (Ed: M. **S.** Whittingham and A. J. Jacobson), Academic Press, New York, *24*, 1982.

2. R. B. Kaner, J. Kouvetakis, C. E**.** Warble, M. L. Sattler and N. Bartlett, *Mater. Res. Bull.,* **22**, *399*, 1987.

3. M. Kawaguchi and N. Bartlett, *Chemistry, Physics and Applications of Fluorine-Carbon and Fluoride-Carbon Compounds*, (Ed: T. Nakajima) Marcel Dekker, New York, Chapter 5, 1995.

4. M. Kawaguchi, *Adv. Mater.*, **9**, *8*, 1997.

5. J. D. Bernal, *Proc. R.* Soc. *London, Ser. A,* **106,** *749***,** 1924.

6. A. H. R. Palser, *Phys. Chem. Chem. Phys*., **1**, *4459*, 1999.

7. J. W. Mcclure, *Phys. Rev*., **108**, *612*, 1957.

8. K. T. Park, K. Terakurat and N. Hamada, *J. Phys. C: Solid State Phys.* **20,** *1241*, 1987.

9. A. Cattelani, M. Posterneak, A. Baldereschi, H. J. F. Jansen and A. J. Freeman, *Phys. Rev. B*, **32**, *6997*, 1985.

10. M. Kawaguchi, T. Kawashima and T. Nakajima, *Chem. Mater*, **8**, *1197,* 1996.

11. A. Y. Liu, R. M. Wentzcovitch and M. L. Cohen, *Phys. Rev. B,* **39**, *1760*, 1989.

12. M. Morita, T. Hanada, H. Tsutsumi, Y. Matsuda and M. Kawaguchi, *J. Electrochem. Soc.*, **139,** *1227*, 1992.

13. S. Iijima, *Nature*, **354**, *56*, 1991.

14. N. G. Chopra, R. J. Luyken, K. Cherrey, V. H. Crespi, M. L. Cohen, S. G. Louie and A. Zettl, , *Science*, **269**, *966*, 1995.

15. T. Laude, Y. Matsui, A. Marraud and B. Jouffrey, *Appl. Phys. Lett.*, **76**, *3239*, 2000.

16. W. Han, Y. Bando, K. Kurashima and T. Sato, *Appl. Phys. Lett*., **73**, *3085*, 1998.

17. O. R. Lourie, C. R. Jones, B. M. Bartlett, P. C. Gibbons, R. S. Ruoff and W. E. Buhro, *Chem. Mater.*, **12**, *1808,* 2000.

18. R. Sen, B. C. Satishkumar, A. Govindaraj, K. R. Harikumar, G. Raina, J. P. Zhang, A. K. Cheetham and C. N. R. Rao, *Chem. Phys. Lett.*, **287**, *671*, 1998.

19. M. Terrones, P. Redlich, N. Grobert, S. Trasobares, W. K. Hsu, H. Terrones, Y. Q. Zhu, J. P. Hare, C. L. Reeves, A. K. Cheetham, M. Ruhle, H. W. Kroto and D. R. M. Walton, *Adv. Mater.*, **11**, *655*, 1999.

20. S. L. Sung, S. H. Tsai, C. H. Tseng, F. K. Chiang, X. W. Liu and H. C. Shih, *Appl. Phys. Lett.*, **74**, *197*, 1999.

21. D. Y. Zhong, S. Liu, G. Y. Zhang and E. G. Wang, *J. Appl. Phys.*, **89**, *5939*, 2001.

22. O. Stephan, P. M. Ajayan, C. Colliex, P. Redlich, J. M. Lambert, P. Bernier and P. Lefin, *Science*, **266**, *1683,* 1994.

23. Z. W. Sieh, K. Cherry, N. G. Chopra, X. Blase, Y. Miyamoto, A. Rubio, M. L. Cohen, S. G. Louie, A. Zettl and R. Gronsy, *Phys. Rev. B*, **51**, *11229*, 1995.

24. P. Redlich, J. Loeffler, P. M. Ajayan, J. Bi, F. Aldinger and M. Rule, *Chem. Phys. Lett.*, **260**, *465,* 1996.

25. J. Yu, J. Ahn, S. F. Yoon, Q. Zhang, Rusli, B. Gan, K. Chew, M. B. Yu, X. D. Bai and E. G. Wang, *Appl. Phys. Lett.*, **77**, *1949,* 2000.

26. N. Hamada, S. Sawada and A. Oshiyama, *Phys. Rev. Lett.*, **68**, *1579, 1992*.

27. A. Hassanien, M. Tokumoto, Y. Humazawa, H. Kataura, Y. Maniwa, S. Suzuki and Y. Achiba, *Appl. Phys. Lett.*, **73**, *3839,* 1998.

28. A. Hassanien, M. Tokumoto, S. Ohshima, Y. Kuriki, F. Ikazaki, K. Uchida and M. Yumura, *Appl. Phys. Lett.*, **75**, *2755,* 1999.

29. D. Golberg, P. Dorozhkin, Y. Bando, M. Hasegawa, Z. C. Dong, *Chem. Phys. Lett.,* **359**, *220,* 2002.

30. X. D. Bai, C. Y. Zhi and E. G. Wang, *J. Nanosci. Nanotechnol.*, **4**, *35*, 2001.

31. S. Azevedo, R. D. Paiva and J. R. Kaschny, *J. Phys.: Condens. Matter,* **18,** *10871*, 2006.

32. M. A. Mannan, M. Nagano, T. Kida, N. Hirao and Y. Baba, *J. Phys. Chem. Solids* **70**, *20*, 2009.

33. V. S. Sulyaeva, Y. M. Rumyantsev, M. L. Kosinova, A. N. Golubenko, N. I. Fainer and F. A. Kuznetsov, *Surf. Coat. Technol.* **201***, 9009,* 2007.

34. H. A. Castillo, A. Devia, G. Soto, J. A. Diaz and W. D. L. Cruz, *Microelectronic J*, **39**, *1382,* 2008.

35. Z. F. Ying, D. Yu, H. Ling, N. Xu, Y. F. Lu, J. Sun and J. D. Wu, *Diamond Relat. Mater*, **16**, *1579*, 2007.

36. F. Zho, K. Adachi and K. Kato, *Thin Solid Films,* **497**, *210,* 2006.

37. V. Linss, J. B. Quiquia, P. Haussler and F. Richter, *Thin Solid Films*, **467**, *66,* 2004.

38. D. H. Kim, E. Byon, S. Lee, J. K. Kim and H. Ruh, *Thin Solid Films*, **447**, *192*, 2004.

39. M. K. Lei, Q. Li, Z. F. Zhou, I. Bello, C. S. Lee and S. T. Lee, *Thin Solid Films*, **389**, *194*, 2001.

40. F. Zhuge and S. Yamanaka, *J. Alloys Compd.*, **466**, *299*, 2008.

41. F. Zhuge, Z. G. Ji, H. P. He, Z. Z. Ye and L. P. Zhu, *J. Cryst. Growth*, **310**, *3869*, 2008.

42. E. Kroke, K. W. Volger, A. Klonczynski and R. Riedel, *Angew. Chem. Int. Ed.*, **40**, *1698*, 2001.

43. K. W. Volger, E. Kroke, C. Gervais, T. Saito, F. Babonneau, R. Riedel, Y. Iwamoto and T. Hirayama, *Chem. Mater.*, **15,** *755*, 2003.

44. A. Vinu, M. Terrones, D. Golberg, S. Hishita, K. Ariga and T. Mori, *Chem. Mater.*, **17**, *5887*, 2005.

45. H. Guo and Q. Gao, *J. Power Sources*, **186**, *551*, 2009.

46. R. Reidel, J. Bill and G. Passing, *Adv. Mater*, **3**, *551*, 1991.

47. M. Hubacek and T. Sato, *J. Solid State Chem.*, **114**, *258*, 1995.

48. K. Suenaga, C. Colliex, N. Demoncy, A. Loiseau, H. Pascard and F. Willaime, *Science,* **278**, *653*, 1997.

49. Y. Zhang, H. Gu, K. Suenaga and S lijirna, *Chem. Phys. Lett.,* **279,** *264,* 1997.

50. W. Q. Han, J. Cumings, X. Huang, K. Bradley and A. Zettl, *Chem. Phys. Lett.*, **346,** *368*, 2001.

51. M. Terrones, D. Golberg, N. Grobert, T. Seeser, M. R. Reyes, M. Mayne, R. kamalakaran, P. Dorozhkin, Z. C. Dong, H. Terrones, M. Ruhle and Y. Bando, *Adv. Mater.,* **15**, *1899*, 2003.

52. W. L. Wang, X. D. Bai, K. H. Liu, Z. Xu, D. Golberg, Y. Bando and E. G. Wang, *J. Am. Chem. Soc.,* **128,** *6530,* 2006.

53. S. Y. Kim, J. Park, H. C. Choi, J. P. Ahn, J. Q. Hou and H. S. Kang, *J. Am. Chem. Soc.,* **129,** *1705*, 2007.

54. J. Dinesh, M. Eswaramoorthy and C. N. R. Rao, *J. Phys. Chem. C,* **111,** *510*, 2007

55. X. Sun and Y. Li, *Angew. Chem. Int. Ed.,* **43**, *597*, 2004.

56. C. Y. Zhi, X. D. Bai and E. G. Wang, *Appl. Phys. Lett.*, **80**, *3590,* 2002.

57. J. Wu, W. Q. Han, W. Walukiewicz, J. W. Ager, III and W. Shan, *Nano Lett.*, **4**, *647*, 2004

58. W. Q. Han, W. Mickelson, J. Cumings and A. Zettl, *Appl. Phys. Lett*., **81**, *1100*, 2002.

59. A. Gomathi, A. Sundaresan and C. N. R. Rao, *J. Solid State Chem.*, **180**, *291*, 2007.

60. A. Gomathi, S. Reshma and C. N. R. Rao, *J. Solid State Chem.*, **182**, *72*, 2009.

61. S. Okada and A. Oshiyama, *Phys. Rev. Lett.,* **84,** *146803*, 2001.

62. J. Choi, Y. H. Kim, K. J. Chang and D. Tomanek, *Phys. Rev. Lett.,* **67**, *14680*, 2003.

63. J. Nakamura, T. Nitta and A. Natori, *Phys. Rev. Lett.,* **72**, *205429*, 2005.

64. R. Q. Wu, L. Liu, G. W. Peng and Y. P. Feng, *Appl. Phys. Lett.,* **86,** *122510*, 2005.

65. A. R. Milliward and O. M. Yaghi, *J. Am. Chem. Soc.,* **127,** *17998*, 2005.

66. S. Cavenati, C. A. Grande and A. E. Rodrigues, *J. Chem. Eng. Data,* **49,** *1095*, 2004.

67. A. C. Sudik, A. R. Millward, N. W. Ockwig, A. P. Cote, J. Kim and M. Yaghi, *J. Am. Chem. Soc.,* **127,** *7110*, 2005.

68. L. G. Jacobsohn, R. K. Schulze, M. E. H. M. Costa and M. Nastasi, *Surf. Sci.*, **572**, *418*, 2004.

69. M. Kawaguchi and K. Nozaki, *Chem. Mater.*, **7**, *257*, 1995.

70. A. Lousa, J. Esteve, S. Muhl and E. Martínez, *Diamond Relat. Mater.*, **9**, *502*, 2000.

71. K. S. W. Sing, *Pure Appl. Chem.*, **57**, *603*, 1985.

CHAPTER 5

BCN: A graphene analogue with remarkable adsorptive properties*

Summary

This chapter deals with the synthesis, characterization and properties of BCN which is a graphene analogue. This analogue of graphene containing boron, carbon and nitrogen (BCN) has been obtained by the reaction of high-surface-area activated charcoal with a mixture of boric acid and urea at 1173 K. X-ray photoelectron spectroscopy and electron energy loss spectroscopy reveal the composition to be close to BCN. The X-ray diffraction pattern, high-resolution electron microscopy images and Raman spectrum indicate the presence of graphite-type layers with low sheet-to-sheet registry. Atomic force microscopy reveals the sample to consist of two to three layers of BCN, as in a few-layer graphene. BCN exhibits more electrical resistivity than graphene, but weaker magnetic features. BCN exhibits large surface area and high propensity for CO_2 uptake (up to 100 wt%) at 195 K and a hydrogen uptake of 2.6 wt% at 77 K.

---

*A paper based on this study has been published in *Chem. Eur. J.* **(2010)**.

5.1 Introduction

Graphene, the one atom thick two dimensional honeycomb sp^2 network of carbon has become one of the most of exciting topic of research in the last five to six years.[1-6] This atomically thin carbon sheet is the mother of all graphitic forms, but it exhibits many unique properties which is distinctly different from other graphitic forms like graphite, carbon nanotubes and fullerenes. For example, graphene exhibits

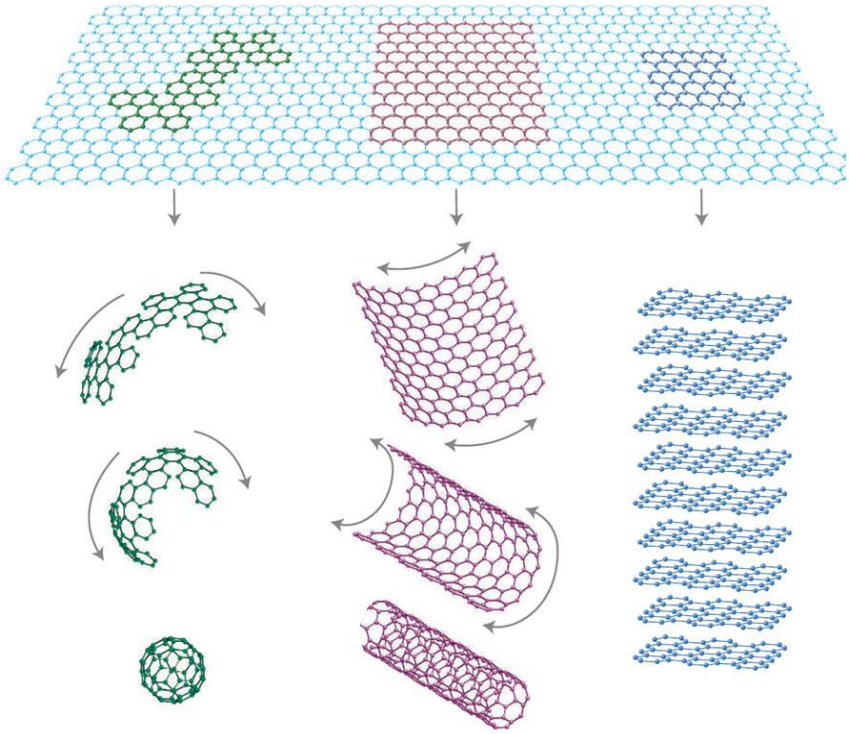

Figure 5.1: Graphene: mother of all graphitic forms. (From reference 1)

anomalous quantum Hall effect[7] and effectively relativistic dynamics of charge carriers.[8] These phenomena discovered earlier, with different materials possess different structure and composition, but graphene showing the similar phenomena is quite interesting. The electron mobility of graphene can exceed 15,000 $cm^2V^{-1}s^{-1}$ even under ambient conditions.[7, 9-11] Depending on the direction of the cutting line of a graphene sheet, there can be two types of edges created; armchair and zigzag

edges.[12] The electronic structure of graphene crucially depends on the geometrical shape of the edges. According to the theoretical and experimental studies,[13-20] a nonbonding π-electron state called "edge state" is created along the zigzag edges, whereas no such state is present in the armchair edges. Graphene exhibits excellent mechanical property, it is not only the thinnest but also the strongest material ever known.[21] The attractive properties of graphene have potential for variety of applications. Since it is transparent and a good conductor, graphene is suitable for producing transparent touch screens, light panels and solar cells. When mixed into plastics, graphene can turn them into conductors of electricity while making them more heat resistant and mechanically robust.

Graphene is opening up a new research area for materials science and condensed-matter physics with a wide range of diversified potential applications. With graphene, physicists can now study a new class of two-dimensional materials with unique properties. Graphene makes experiments possible that give new twists to the phenomena in quantum physics. Graphene transistors are predicted to be substantially faster than today's silicon transistors and could result in more efficient computers.[22] The fascinating properties of graphene gave a huge momentum to study a wide range of other 2D materials, many of which have enormous potential for both basic research and applications. This includes, BN,[23-25] transition metal dicharcogenides (MoS_2 and WS_2),[26] transition metal oxides and other layered structures such as Bi_2Te_3[27] and Bi_2Se_3.

Even though graphene has generated a huge interest due to its unique properties and potential applications, its use as a semiconductor in nano-electronic circuits is however limited due to its vanishing bandgap. In contrast to graphene which

possesses zero bandgap, BN with a similar structure is an insulator. On the other hand, $B_xC_yN_z$ materials which can be considered as a hybrid of graphite and BN with a graphene-like structure can offer several types of semiconductors with a tunable band gap. The properties of $B_xC_yN_z$ can be tuned by varying their composition and the arrangement of B, C and N atoms. Graphene analogues of $B_xC_yN_z$ could exhibit many interesting properties superior to both graphene and graphene-like BN.

5.2 Scope of the present investigations

Analogues of graphite containing boron, carbon and nitrogen have attracted interest for some years and there has been some success in preparing $B_xC_yN_z$ compositions.[28] The subject has become of great interest recently because of the relevance of such materials to graphene.[29-31] There are several reports in the literature of $B_xC_yN_z$ nanotubes of various compositions.[32-41] Nanotubes as well as bulk samples of BC_4N has been prepared by the reaction of B_2O_3, urea and carbon at high temperatures.[42,43] A material with the stoichiometry of BCN would be of particular interest because of its unique composition and possible interesting properties. It would indeed be instructive to compare the properties of BCN with those of graphite or graphene. Bartlett and coworkers[44] seem to have prepared a composition close to BCN by the reaction of BCl_3, NH_3 and acetylene. However, this sample could not been adequately characterized for the structure and properties. A composition close to BCN has been reported[45] by reaction of the mesoporous carbon with B_2O_3 and N_2, but the only property reported was its surface area. We, therefore, sought to prepare BCN by the reaction of a mixture of B_2O_3 and urea with activated charcoal of high surface area. This strategy was employed because the reaction of low surface area carbon with urea and boric acid yields BC_4N. In this procedure, urea has been used as a source of NH_3, a strategy that has been successful

to prepare metal nitrides and oxynitrides.[46,47] In this article, we report the successful synthesis of a layered material with the composition BCN with high surface area and a great propensity for CO_2 uptake. Interestingly, the as-prepared material consists of only a few layers, as in graphene.

5.3 Experimental and related aspects

5.3.1 Synthesis of BCN

1 g of activated charcoal (surface area 1256 m^2/g) was thoroughly mixed with 40 ml aqueous solution of boric acid (0.3 g) and urea (3.6 g). The mixture was warmed at 333 K forming a thick slippery liquid, which was then dried at the same temperature. The dried mixture was heated in a tube furnace at 1173 K for 10 h in a N_2 atmosphere. After cooling it down to room temperature, the sample was heated in an NH_3 environment up to 1203 K for 3 hour. The black coloured product obtained after the reaction was subjected to characterization.

5.3.2 Characterization techniques

X-Ray diffraction (XRD): XRD patterns were recorded at 298 K with a Rich-Siefert 3000-TT diffractometer using Cu Kα radiation.

Electron Microscopy: The morphology of the product was examined by transmission electron microscopy (TEM) with a JEOL JEM 3010 instrument (Japan) operated at an accelerating voltage of 300 kV, and field emission scanning electron microscope (FESEM, FEI Nova-Nano SEM-600, Netherlands). Electron energy loss spectra (EELS) were recorded using a FEI, TECNAI F30 or TITAN transmission electron microscope, equipped with an energy filter for EELS operating at 300 kV.

X-ray Photoelectron Spectroscopy (XPS): X-Ray photoelectron spectroscopy (XPS) measurements were carried out using an ESCALAB MKIV spectrometer employing Al Kα (1486.6 eV) as photon source.

Atomic force microscopy: A NanoMan instrument was used in tapping mode for AFM measurements. A dilute dispersion of sample in acetone dropped on a SiO_2 substrate was used for AFM measurements.

Raman spectroscopy: Raman spectra were recorded using a LabRAM HR with a 633 nm line from HeNe laser.

Thermogravimetric analysis: Thermogravimetric analysis was performed using a Mettler Toledo Star system.

Gas adsorption: QUANTACHROME AUTOSORB-1C surface area analyzer was used for gas adsorption studies. Surface areas were obtained from nitrogen adsorption–desorption isotherm at 77 K. High-pressure gas sorption isotherm measurements were carried out on BELSORP-HP, BEL JAPAN high pressure instrument. Dead volume of the sample cell was measured with He of 99.999% purity. Non-ideal correction for hydrogen gas was done by applying virial coefficients at the respective measurement temperature. The adsorption isotherm of MeOH (at 298 K) was measured in the gaseous state by using BELSORP-aqua volumetric adsorption instrument from BEL, Japan.

Resistance measurements: DC resistance measurements were carried out by the standard four-probe method using the resistivity option in the Physical Property Measurement System (PPMS), Quantum Design, USA.

Magnetization measurements Magnetic measurements were performed by employing a vibrating sample magnetometer (VSM) in the PPMS.

5.4 Results and discussion

Activated charcoal with a high-surface area (1256 m^2/g) constitutes the primary starting material for the synthesis of $B_xC_yN_z$. Reaction of the activated charcoal with urea and boric acid at 1173 K gave a product containing boron, carbon and nitrogen. The material obtained was soft and flaky. Transmission electron microscopy investigations reveal a flake-like morphology of the product. The TEM image in Figure 5.2 (a) shows the presence of BCN layers similar to few-layer graphene.[30,48] The inset in Figure 5.2 (a) shows a selected area electron diffraction (SAED) pattern with two rings due to the (002) and (100) reflections of the graphite-like material. The FESEM image shows rippled and entangled nanosheets of BCN (Figure 5.2 (b)). The flakes are transparent and stable under the electron beam.

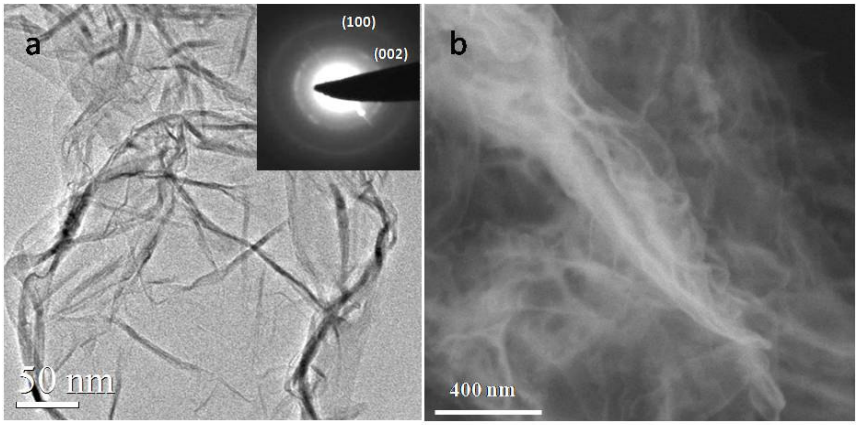

Figure 5.2: (a) TEM image (Inset shows the corresponding SAED pattern) and (b) FESEM image of BCN.

XPS core level spectra of the $B_xC_yN_z$ product are shown in Figure 5.3. The C 1s signal can be deconvoluted into bands at 283.1, 285.4 and 288.2 eV, assigned to three different kinds of carbons, bonded to boron, carbon and nitrogen respectively.[40] The N 1s signal can be deconvoluted into two bands at 397.1 and

399.8 eV. The former corresponds to nitrogen bonded to boron and the latter to nitrogen bonded to carbon.[40] The B 1s signal can be deconvoluted into two bands,

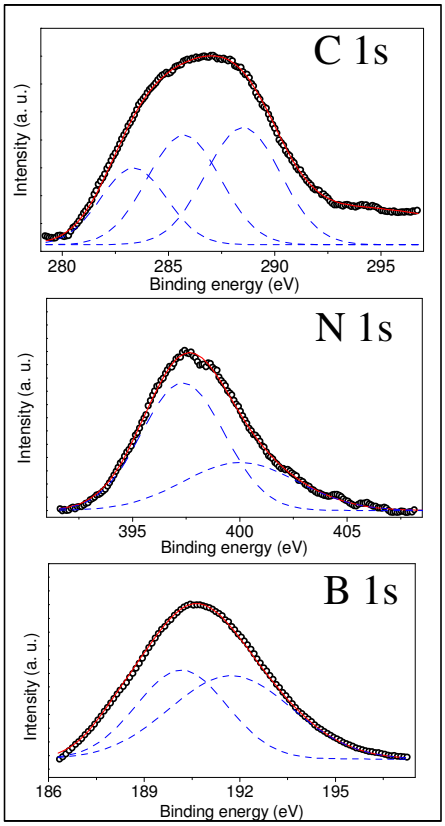

Figure 5.3: XPS data showing the core-level spectra (solid circles) for C 1s, N 1s and B 1s for the BCN Sample. While the dotted lines represent the deconvoluted component spectra, the black lines overlapping the corresponding experimental spectra are overall fit.

of which first one corresponds to boron bonded to carbon and second one assigned to boron atom bonded to nitrogen. Based on the capture cross sections and intensities of B, C and N signal of XPS core level spectra, we estimated the composition to be $BC_{1.5}N_{1.1}$. To establish the elemental composition, we carried out EELS measurements on the K-edge absorption for B, C and N in a high resolution electron microscope. The EEL spectrum of the sample in Figure 5.4 (a) clearly shows the K-shell ionization edges at ~ 190, 284 and 401 eV for B, C and N respectively. The two

peaks at each core edge fine structure is characteristic of sp^2 hybridization state, corresponding to π^* and σ^* bands respectively, thereby indicating the graphite-like

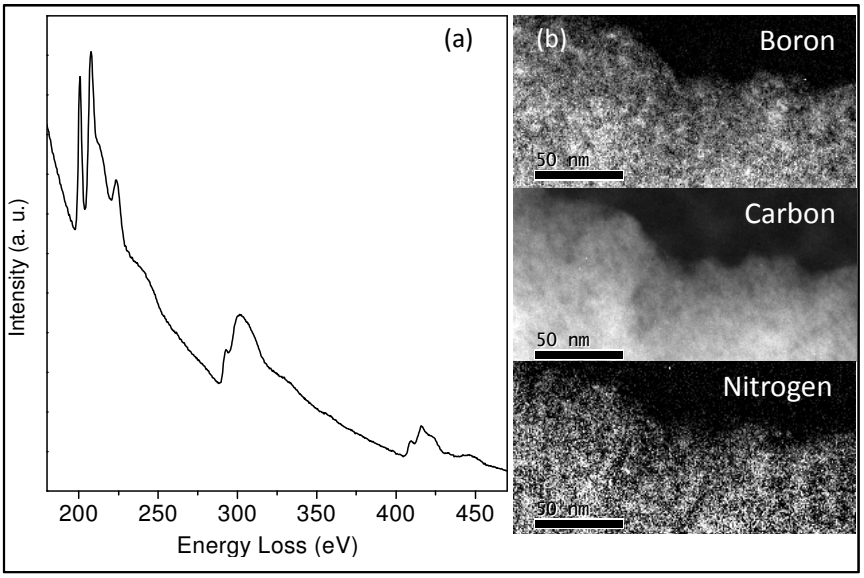

Figure 5.4: (a) EEL spectra and (b) corresponding EEL map of boron, carbon and nitrogen of BCN.

layered structure of the sample.[40] EELS measurements show the average chemical composition to be $BC_{1.2}N$. This analysis is in reasonable agreement with the analysis of XPS. For the purpose of convenience, we have approximated composition to be BCN. The image in Figure 5.4 (b) shows elemental mapping of boron, carbon and nitrogen in a BCN flake. All the three components are uniformly distributed throughout the flake confirming the homogeneous nature of BCN.

The XRD pattern of BCN, shown in the Figure 5.5 (a), is similar to patterns reported for graphitic materials with little sheet to sheet registry.[49,50] The pattern has two broad reflections with d spacings of 3.46 Å and 2.12 Å corresponding to the (002) and (100) planes respectively. The interlayer distance in BCN (3.46 Å) is

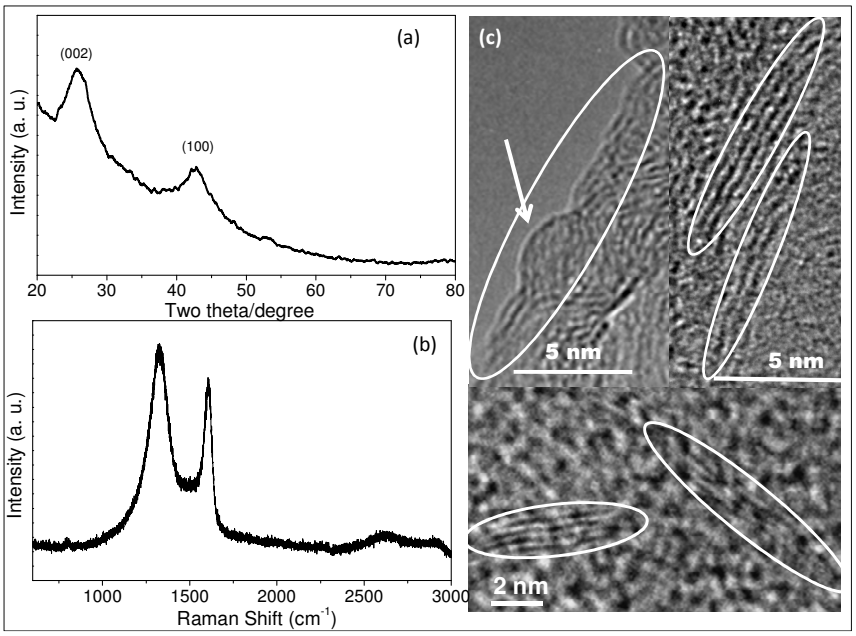

Figure 5.5: (a) XRD pattern, (b) Raman spectrum and (c) HRTEM image of BCN

larger than that in graphite (3.33 Å) and h-BN (3.36 Å). The Raman spectrum of the BCN recorded with 633 nm line from a HeNe laser is shown in Figure 5.5 (b). The spectrum is similar to that of graphitic materials with a D band at 1324 cm^{-1} and G band at 1592 cm^{-1}.[30,51,52] The band at 2600 cm^{-1} may be due to a D + G combination band or a 2D overtone. The high resolution TEM image (Figure 5.5 (c)) mainly shows 2 or 3 layers of BCN with an interplaner distance of 3.43 Å.

The basic reactions involved in the formation of BCN are the dehydration of $B(OH)_3$ and decomposition of urea, as shown below.

$$2B(OH)_3 \xrightarrow{\triangle} B_2O_3 + 3\,H_2O$$

$$CO(NH_2)_2 \xrightarrow{\triangle} NH_3 + HNCO$$

The stoichiometric reaction for the formation of BCN may be written as,

$$B_2O_3 + 2NH_3 + 2C \xrightarrow{\triangle} 2BCN + 3H_2O$$

The overall reaction involves the release of gaseous species which could cause exfoliation and promote the incorporation of boron and nitrogen into the graphitic layers.

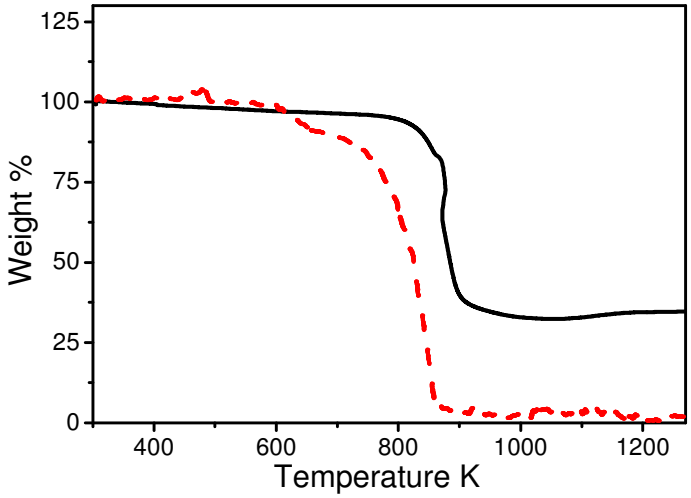

Figure 5.6: TGA curve of BCN (full line) and activated charcoal (broken line)

Thermogravimetric analysis curves of BCN and activated charcoal, carried out in air, are shown in Figure 5.6. BCN shows about 57 % of weight loss at ~ 873 K leaving a residue which is stable up to 1273 K, while activated charcoal completely oxidizes before 873 K. The XRD pattern of the residue in the case of BCN shows the presence of BN and C_3N_4. The approximate reaction of BCN in air can be written as follows:

$$12BCN + 15O_2 \longrightarrow 4BN + C_3N_4 + 9CO_2 + 2N_2 + 4B_2O_3$$

Figure 5.7 shows AFM images of BCN with the corresponding height profiles. The images (a) and (b) show the thickness of samples to be 1.1 and 0.65 nm corresponding to two and three layers respectively. We find that a majority of BCN flakes possesses two to three layers, with occasional presence of single layers, as shown by the bar diagram in Figure 5.7 (c). Thus the AFM results clearly

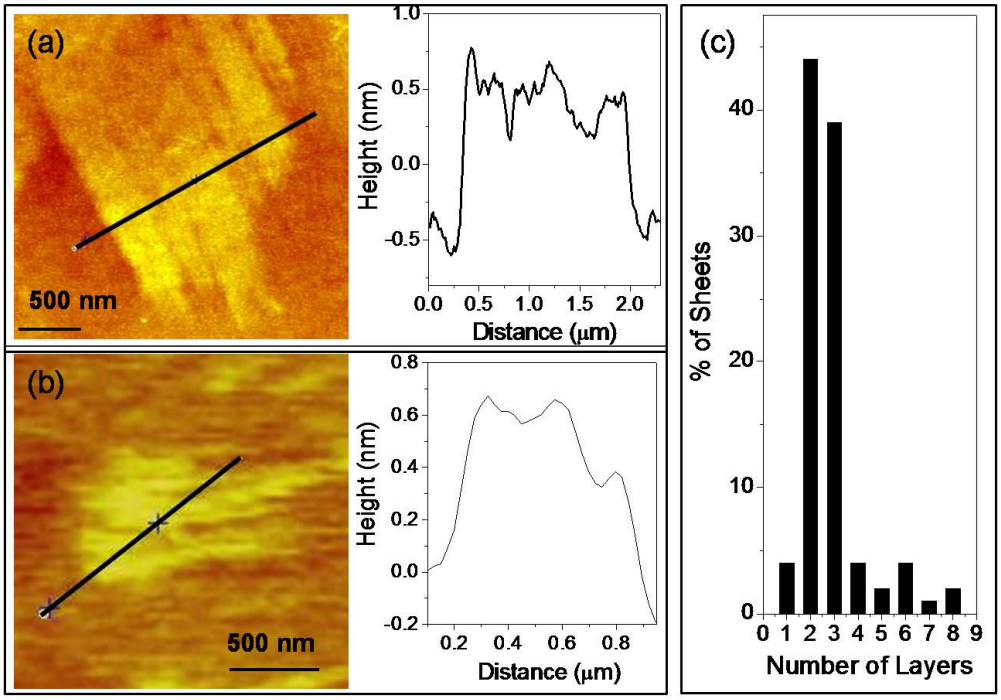

Figure 5.7: AFM images and corresponding height profile of (a) three-layered and (b) two-layered BCN

demonstrate that the BCN synthesized by us possesses only a few layers, resembling few layer-graphene rather than a graphitic material.

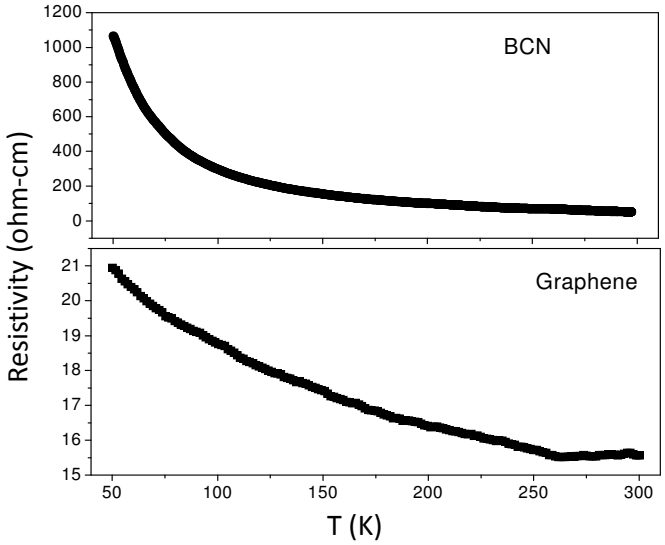

Figure 5.8: Resistivity of BCN and graphene as a function of temperatures

In Figure 5.8, we have compared the resistivity vs temperature plot of BCN with that of two-three layer graphene prepared by arc discharge of graphite in hydrogen (HG).[53] Both show semiconducting behaviour, but BCN exhibits two orders of magnitude higher resistance than graphene.

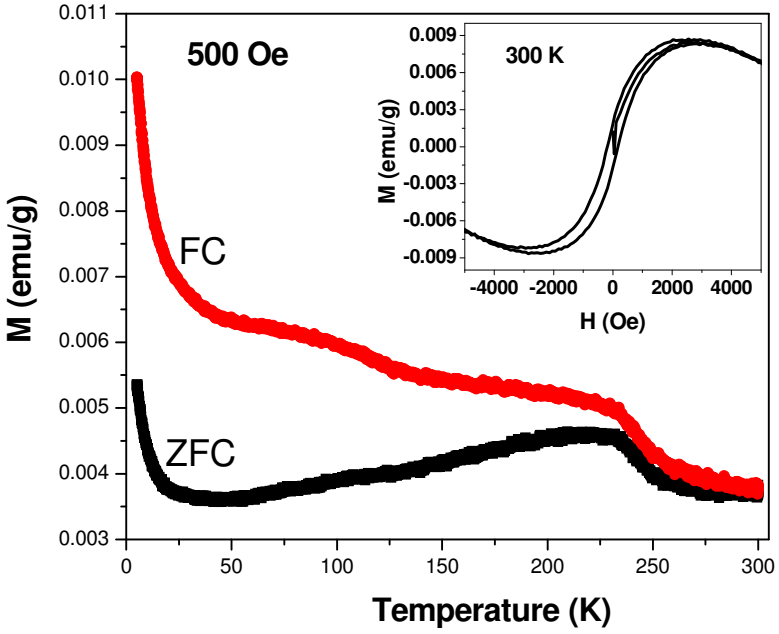

Figure 5.9: Temperature dependence of the magnetization of BCN at 500 Oe under FC and ZFC conditions. The inset shows the magnetic hysteresis at 300 K.

We have examined the magnetic properties of BCN under field-cooled (FC) and zero-field-cooled (ZFC) conditions. Figure 5.9 shows the temperature variation of magnetisation at 500 Oe. The data show divergence between FC and ZFC data below 300 K. The divergence disappears at higher fields and the behaviour is somewhat similar to magnetically frustrated systems or phase-separated oxides. The Curie-Weiss temperature is - 350 K showing antiferromagnetic interaction. However, the material shows a ferromagnetic hysteresis loop at 300 K, as shown in the inset of Figure 5.9. The values of saturation magnetization and remnant magnetism are both very low and the coercive field is ~175 Oe. Magnetism in BCN could arise from the

contribution of edge effect and defects. The presence of both ferromagnetic and antiferromagnetic interactions in BCN are similar to graphene,[54] but the magnitude of the magnetic features is smaller in BCN.

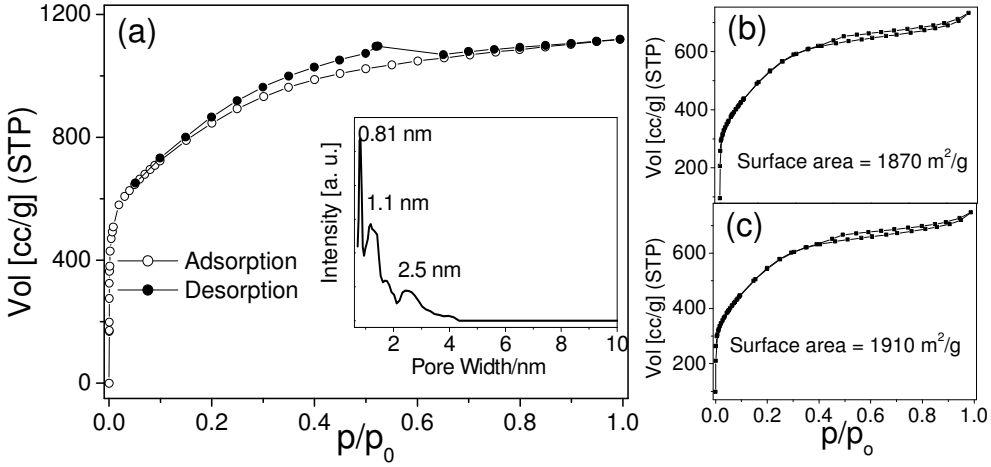

Figure 5.10: (a), (b) and (c) Nitrogen adsorption-desorption isotherms of BCN of different batches of preparation. Inset of Figure 5.10 (a) shows pore size distribution of BCN.

The nitrogen adsorption-desorption isotherms of BCN at 77 K are typical of a type I isotherm (Figure 5.10), which is characteristic of microporous materials.[55] With a small hysteresis loop, these isotherms are concave to the p/p_0 axis and the adsorption approaches a limiting value of $p/p_0 \rightarrow 1$. BCN exhibits different Brunaure-Emmett-Teller (BET) surface area for different batches of preparation. One batch of BCN sample has shown to exhibit a surface area of 2911 m^2/g (Figure 5.10 (a)). However, surface areas obtained for other samples of BCN are in the range of 1600 to 1900 m^2/g. In Figure 5.10 (b) and (c), we show N_2 adsorption-desorption isotherm of two other batches of BCN samples exhibiting surface area of 1870 and 1910 m^2/g respectively. The pore size distribution calculated from the adsorption isotherm shows that the major contribution to the surface area is from the micropores (0.81 nm and 1.1 nm) with a small contribution from mesopores (2.5 nm), as can be seen from the inset in Figure 5.10 (a). The surface areas of these BCN samples are

higher than any composition of the $B_xC_yN_z$ materials reported hitherto. It is known that the surface area of graphene increases with the decrease in the number of layers. Graphene with two to three layers exhibits a surface area in the range of 1000 to 1800 m^2/g.[56] Thus the high surface area of BCN prepared by us is consistent with the AFM observations that the material consists of two to three layers.

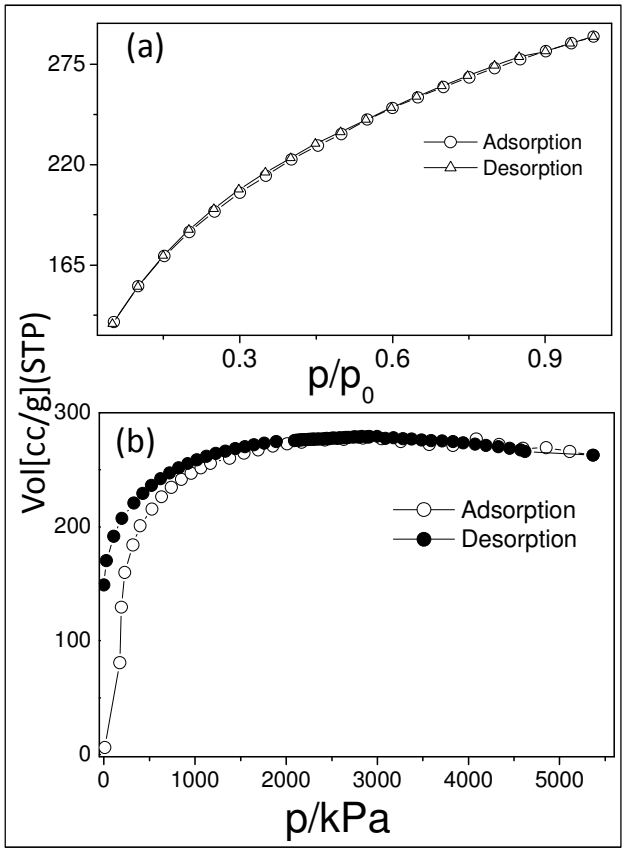

Figure 5.11: H_2 adsorption-desorption isotherm of BCN at (a) 77 K and 1 atmosphere and (b) at 77 K and 55 bar

Materials with good H_2 uptake have potential as clean-energy alternatives. We have examined H_2 adsorption on BCN at 77 K and 1 atmosphere and it finds an uptake of 2.6 wt%. Both adsorption and desorption isotherms of H_2 follow the same path, as shown in Figure 5.11 (a). H_2 uptake on BCN does not increase with increasing pressure. In Figure 5.11 (b), we show adsorption-desorption isotherms of

H_2 on BCN carried out at 77 K and 55 bar. The adsorption isotherm rises sharply and reaches saturation at 10 bar, with a 2.6 wt% of H_2 uptake.

Materials with good CO_2 adsorption capacity are of importance from both environmental and industrial points of view. Graphene analogues of BCN show remarkably high CO_2 uptakes. BCN with highest surface area exhibits 100 wt% of CO_2 uptake at 195 K and 1 atmosphere. Two other samples of BCN have shown 90 and 85 wt% of CO_2 uptake (Figure 5.12 (b) and (c)). On the other hand, activated charcoal the starting material of BCN exhibits 58 wt% of CO_2 uptake under the identical conditions. Adsorption-desorption isotherms of CO_2 on BCN follow

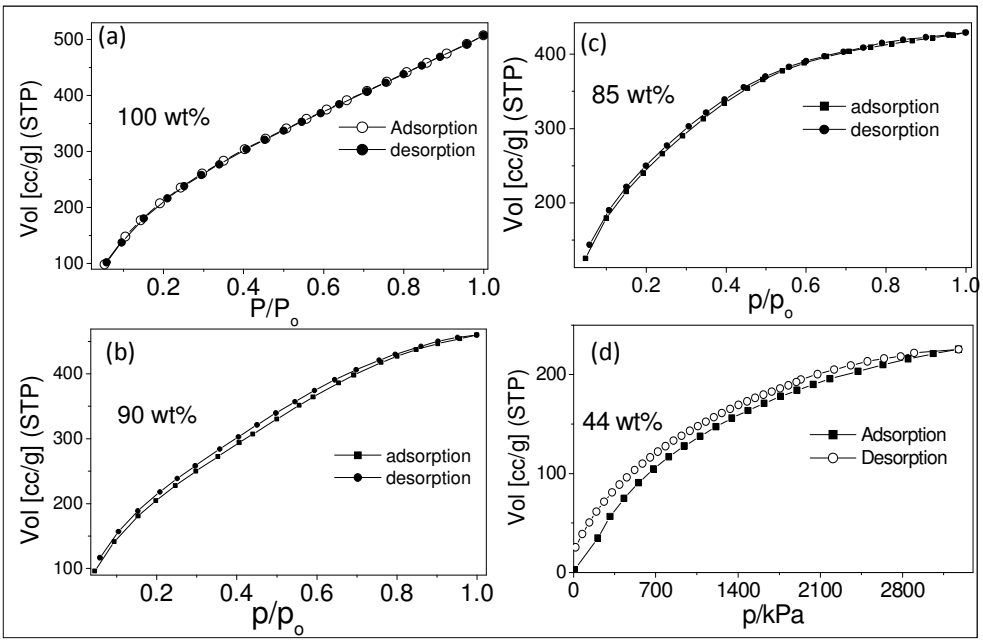

Figure 5.12: (a), (b) and (c) CO_2 adsorption-desorption isotherms of BCN of different batches of preparation, at 195 K and 1 atmosphere, (d) CO_2 adsorption-desorption isotherm of BCN at 298 K and 30 bar

exactly the same path and do not reach saturation at $p/p_0 = 1$ (Figure 5.12 (a), (b) and (c)). However, at room temperature and 30 bar, BCN with highest surface area

uptake 44 wt% of CO_2, shown in Figure 12 (d). The uptake of methanol vapour by BCN is about 26 wt% at room temperature and atmospheric pressure.

Prof. U. V. Waghmare, and Dr. K. P. S. S. Hembram have carried out a first-principles pseudopotential-based DFT studies to understand the structure and properties of BCN. In order to obtain most stable structure of BCN, various ordering of B, C and N atoms on graphene lattice were relaxed to minimum energy. Figure 5.13 shows six different configurations of BCN. The configuration (vi) was

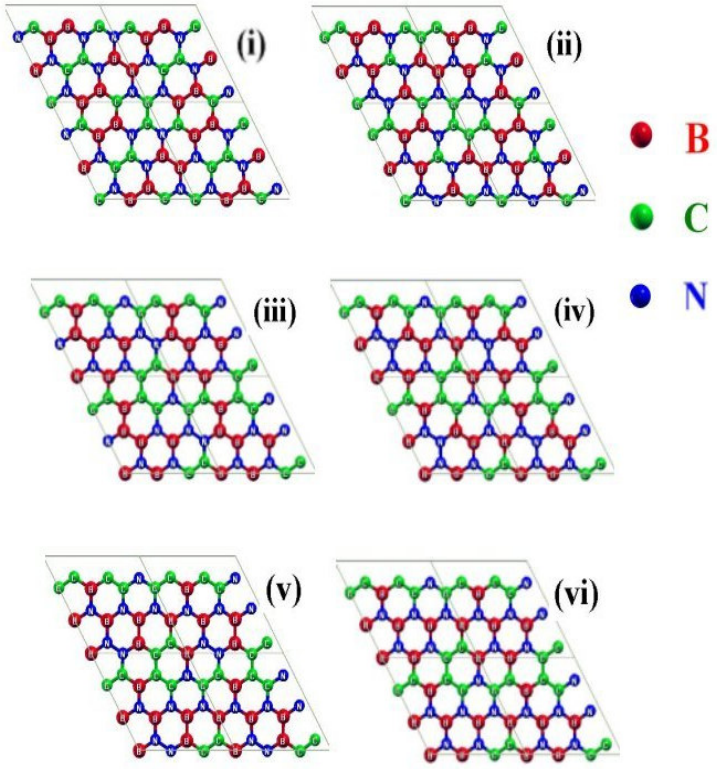

Figure 5.13: Different chemical ordering of B and N on the graphene lattice.

calculated to be the lowest energy configuration with smallest lattice constant (7.52 Å). The lattice constants of other configurations vary within one percent of each other. The cohesive energy of the lowest-energy configuration (vi) is 8.61 eV/atom, smaller than that of graphene (9.16 eV/atom) and BC_4N (8.93 eV/atom).[4,16] In this structure, we see the presence of interlinked local structural motifs of BN_3 and NB_3,

similar to those responsible for the stability of BC_4N. A table comparing lattice constant, bulk modulus and cohesive energy of BCN with six different ordering of B and N on graphene lattice (as shown in Figure 5.13) is given below. BCN is predicted to be an insulator relative to graphene, as indeed found experimentally. The lowest-energy configuration of BCN has a band gap of about 1.8 eV.

Table 5.1: Lattice constant, bulk modulus and cohesive energy of BCN with different ordering of B and N on graphene lattice.

Structure of BCN[(a)]	Lattice Constant (Å)	Bulk Modulus (Pa.m)	E_{coh} (eV/atom)
(i)	7.59	159	8.15
(ii)	7.59	150	8.19
(iii)	7.57	165	8.27
(iv)	7.57	157	8.34
(v)	7.57	158	8.40
(vi)	7.52	174	8.61

(a) See Figure 5.13

Adsorption of CO_2 on BCN and graphene was examined considering the minimum-energy configuration ((vi) in Figure 5.13). The calculations suggest that the strongest CO_2 adsorption occurs with a binding energy of 3.7 kJ/mol compared to 2.0 kJ/mol on graphene. The electrostatic interactions between the B and N sites and oxygen atoms of CO_2 and a small overlap between the electronic states of the molecule and lattice govern the interaction between BCN and CO_2.

5.5 Conclusions

It has been possible to synthesize a $B_xC_yN_z$ composition with x = y = z = 1 by reacting high surface area activated charcoal with urea and boric acid. It has a two-dimensional layered structure. AFM measurements show that BCN mainly consists of 2-3 layers establishing its resemblance to few-layer graphene.[30] BCN prepared by us is a microporous material exhibiting type I N_2 adsorption-desorption isotherms at 77 K and a very large surface area. The extraordinarily high CO_2 uptake of BCN is noteworthy. Theoretical calculations show that the structureof BCN is likely to be one with C-C, B-N and C-N bonds. BCN has a finite energy gap and shows the presence of both ferromagnetic and antiferromagnetic features.

References

1. A. K. Geim and K. S. Novoselov, *Nat. Mater*, **6,** *183,* 2007.

2. D. Li and R. B. Kaner, *Science*, **320**, *1170,* 2008.

3. M. I. Katsnelson, *Materials Today*, **10**, *20,* 2007.

4. C. N. R. Rao, K. Biswas, K. S. Subrahmanyam and A. Govindaraj, *J. Mater. Chem.*, **19**, *2457,* 2009.

5. C. N. R. Rao, A. K. Sood, K. S. Subrahmanyam and A. Govindaraj, *Angew. Chem. Int. Ed*, **48**, *7752*, 2009.

6. C. N. R. Rao, A. K. Sood, R. Voggu and K. S. Subrahmanyam, *J. Phys. Chem. Lett.*, **1**, *572,* 2010.

7. Y. Zhang, Y. W. Tan, H. L. Stormer and P. Kim, *Nature*, **438**, *201*, 2005.

8. K. S. Novoselov, A. K. Geim, S. V. Morozov, D. Jiang, M. I. Katnelson, I. V. Grigorieva, S. V. Dubonos and A. A. Firsov, *Nature*, **438**, *197*, 2005.

9. K. S. Novoselov, A. K. Geim, S. V. Morozov, D. Jiang, Y. Zhang, S. V. Dubonos, I. V. Grigorieva and A. A. Firsov, *Science,* **306,** *666,* 2004.

10. K. S. Novoselov, D. Jiang, F. Schedin, T. J. Booth, V. V. Khotkevich, S. V. Morozov and A. K. Geim, *Proc. Natl. Acad. Sci. USA,* **102,** *10451*, 2005.

11. K. S. Novoselov, A. K. Geim, S. V. Morozov, D. Jiang, M. I. Katsnelson, I. V. Grigorieva, S. V. Dubonos and A. A. Firsov, *Nature,* **438,** *197*, 2005.

12. T. Enoki, Y. Kobayashi and K. Fukui, *Int. Rev. Phys. Chem.,* **26**, *609*, 2007.

13. S. E. Stein and R. L.Brown, *J. Am. Chem. Soc*., **109**, *3721*, 1987.

14. K. Yoshizawa, K. Okahara, T. Sato, K. Tanaka and T. Yamabe, *Carbon,* **32**, *1517*, 1994.

15. M. Fujita, K. Wakabayashi, K. Nakada and K. Kusakabe, *J. Phys. Soc. Jpn.,* **65**, *1920*, 1996.

16. K. Nakada, M. Fujita, G. Dresselhaus and M. S. Dresselhaus, *Phys. Rev. B,* **54**, *17954*, 1996.

17. Y. Kobayashi, K. Fukui, T. Enoki, K. Kusakabe and Y. Kaburagi, *Phys. Rev. B,* **71**, *193406*, 2005.

18. Y. Niimi, T. Matsui, H. Kambara, K. Tagami, M. Tsukada and H. Fukuyama, *Appl. Surf. Sci.* **241**, *43*, 2005.

19. Y. Kobayashi, K. Fukui, T. Enoki and K. Kusakabe, *Phys. Rev. B,* **73**, *125415,* 2006.

20. Y. Niimi, T. Matsui, H. Kambara, K. Tagami, M. Tsukada and H. Fukuyama, *Phys. Rev. B,* **73**, *085421*, 2006.

21. C. Lee, X. Wei, J. W. Kysar and J. Hone, *Science,* **321**, *385*, 2008.

22. Y. M. Lin, C. Dimitrakopoulos, K. A. Jenkins, D. B. Farmer, H. Y. Chiu, A. Grill and P. Avouris, *Science*, **327**, *662*, 2010.

23. W. Q. Han, L. Wu, Y. Zhu, K. Watanabe and T. Taniguchi, *Appl. Phys. Lett.*, **93**, *223103*, 2008.

24. C. Zhi, Y. Bando, C. Tang, H. Kuwahara and D. Golberg, *Adv. Mater.*, **21**, *2889*, 2009.

25. A. Nag, K. Raidongia, K. P. S. S. Hembram, R. Dutta, U. V. Waghmare and C. N. R. Rao, *ACS Nano*, **4**, *1539*, 2010.

26. H. S. S. R. Matte, A. Gomathi, A. K. Manna, D. J. Late, R. Datta, S. K. Pati and C. N. R. Rao, *Angew. Chem. Int. Ed.*, **49**, *4059*, 2010.

27. D. Teweldebrhan, V. Goyal, M. Rahman and A. A. Balandin, *Appl. Phys. Lett.,* **96**, *053107*, 2010.

28. M. Kawaguchi, *Adv. Mater.*, **9**, *8***,** 1997.

29. A. K. Geim and K. S. Novoselov, *Nature materials,* **6**, *183*, 2007.

30. C. N. R. Rao, K. Biswas, K. S. Subrahmanyam and A. Govindaraj, *J. Mater. Chem.*, **19,** *2457*, 2009.

31. L. S. Panchakarla, K. S. Subrahmanyam, S. K. Saha, A. Govindaraj, H. R. Krishnamurthy, U. V. Waghmare and C. N. R. Rao, *Adv. Mater.,* **21***, 4208*, 2009.

32. O. Stephan, P. M. Ajayan, C. Colliex, P. Redlich, J. M. Lambert, P. Bernier and P. Lefin, *Science,* **266,** *1683*, 1994.

33. P. Redlich, J. Loeffler, P. M. Ajayan, J. Bill, F. Aldinger and M. Riihle, *Chem. Phys. Lett.,* **260**, *465***,** 1996.

34. K. Suenaga, C. Colliex, N. Demoncy, A. Loiseau, H. Pascard and F. Willaime, *Science,* **278**, *653*, 1997.

35. Y. Zhang, H. Gu, K. Suenaga and S. lijirna, *Chem. Phys. Lett.,* **279**, *264*, 1997.

36. R. Sen, B. C. Satishkumar, A. Govindaraj, K. R. Harikumar, G. Raina, J. P. Zhang, A. K. Cheetham and C. N. R. Rao, *Chem. Phys. Lett.,* **287**, *671*, 1998.

37. W. Q. Han, J. Cumings, X. Huang, K. Bradley and A. Zettl, *Chem. Phys. Lett.,* **346**, *368*, 2001.

38. M. Terrones, D. Golberg, N. Grobert, T. Seeser, M. Reyes-Reyes, M. Mayne, R. Kamalakaran, P. Dorozhkin, Z. C. Dong, H. Terrones, M. Ruhle and Y. Bando, *Adv. Mater.,* **15**, *1899*, 2003.

39. W. L. Wang, X. D. Bai, K. H. Liu, Z. Xu, D. Golberg, Y. Bando and E. G. Wang, *J. Am. Chem. Soc.,* **128**, *6530*, 2006.

40. S. Y. Kim, J. Park, H. Chul Choi, J. P. Ahn, J. Q. Hou and H. S. Kang, *J. Am. Chem. Soc.,* **129**, *1705*, 2007.

41. C. N. R. Rao and A Govindaraj, *Adv. Mater.*, **21**, *4208*, 2009.

42. K. Raidongia, D. Jagadeesan, M. U. Kahaly, U. V. Waghmare, S. K. Pati, M. Eswaramoorthy and C. N. R. Rao, *J. Mater. Chem.,* **2008**, *18*, 83.

43. K. Raidongia, K. P. S. S. Hembram, U. V. Waghmare, M. Eswaramoorthy and C. N. R. Rao, *Z. Anorg. Allg. Chem.,* **636**, *30*, 2010.

44. R. B. Kaner, J. Kouvetakis, C. E. Warble, M. L. Sattler and N. Bartlett, *Mat. Res. Bull.,* **22**, *399*, 1987.

45. A. Vinu, M. Terrones, D. Golberg, S. Hishita, K. Ariga and T. Mori, *Chem. Mater.,* **17**, *5887*, 2005.

46. A. Gomathi, A. Sundaresan and C. N. R. Rao, *J. Solid State Chem.*, **180**, *291*, 2007.

47. A. Gomathi, S. Reshma and C. N. R. Rao, *J. Solid State Chem.,* **182**, *72*. 2009.

48. G. Wang, J. Yang, J. Park, X. Gou, B. Wang, H. Liu and J. Yao, *J. Phys. Chem. C,* **112**, *8192*, 2008.

49. F. Zhuge and S. Yamanaka, *Journal of Alloys and Compounds,* **466**, *299*, 2008.

50. M. Hubacek and T. Sato, *J. Solid State Chem.,* **114**, *258*, 1995.

51. C. Y. Zhi, X. D. Bai and E. G. Wang, *Appl. Phys. Lett.,* **80**, *3590*, 2002.

52. J. Wu, W. Q. Han, W. Walukiewicz, J. W. Ager-III and W. Shan, *Nano Lett.,* **4**, *647*, 2004.

53. K. S. Subrahmanyam, L. S. Panchakarla, A. Govindaraj and C. N. R. Rao, *J. Phys. Chem. C,* **113**, *4259*, 2009.

54. H. S. S. R. Matte, K. S. Subrahmanyam and C. N. R. Rao, *J. Phys. Chem. C,* **113**, *9982*, 2009.

55. Pure & Appl. Chem. **57**, *603*, 1985.

56. A. Ghosh, K. S. Subrahmanyam, K. Saikrishna, S. Datta, A. Govindaraj, S. K. Pati and C. N. R. Rao, *J. Phys. Chem. C,* **112**, *15704*, 2008.

CHAPTER 6

Synthesis, characterization and properties of BN nanostructures*

Summary

This chapter deals with synthesis, characterization and properties of BN nanostructures. The reaction of urea and boric acid has been exploited to obtain graphene analogues of BN with desired number of layers depending on the relative proportions of the two reactants. Synthesis with a high proportion of urea yields BN flakes with an average of 3 layers, with occasional presence of single layer. The surface area of BN increases with the decreasing number of layers, and the high surface area BN also exhibits high CO_2 adsorption. Few-layer BN can be solubilized by interaction with Lewis bases.

Nanopans and nanosheets formed by graphene-like BN are generated by the vapor phase reaction of NH_3 and BBr_3 at 1223 K. Nanopans of BN, being reported for the first time have a bottom comprising single-layer BN and a wall of 0.7 nm height. The average inner volume of the nanopan is around 400 nm^3.

We have also investigated mechanical properties of composites of polymethylmethacrylate (PMMA) with graphene-like BN, prepared by urea-boric

---

*Papers based on this work have been published in *ACS Nano* **(2010),** *Isr. J. Chem* **(2010)** and *Scripta Materialia* **(2010).**

acid reaction, to explore the dependence of the properties on the number of BN layers. The study demonstrates that mechanical properties of the polymer composites are significantly improved by BN with the fewest number of layers. Thus, with incorporation of three-layer BN, the hardness and elastic modulus of the composite showed 125 and 130% increase respectively relative to pure PMMA.

6.1 Introduction

Boron nitride is one of the most important III-V group and non-oxide ceramic materials. This simple material exhibits many interesting properties including wide band gap, high chemical and thermal stability, excellent mechanical properties and high thermal conductivity. Because of these properties BN has been used in different fields, for example, as a solid lubricant in rigorous environments, as an ultraviolet-light emitter[1-5] and as an insulating thermoconductive filler in composites.[6,7] Even though boron nitride is not found in nature, several novel synthetic and processing methods have made BN an economically affordable advanced material for various applications. The first BN synthesis was made in 1842 by W. H. Balmain by the reaction of molten boric acid with potassium cyanide.[8]

Pairs of boron and nitrogen atoms are isoelectronic to pairs of carbon atoms. Therefore, like carbon, BN has four crystalline structural variants: cubic (c-BN), wurzite (w-BN), hexagonal (h-BN) and rhombohedral (r-BN).[9,10] Figure 6.1 depicts the structural projections of the BN phases. c-BN and w-BN are hard and dense phases and are bonded through strong sp^3 hybridization (σ-bond). Both of them consist of tetrahedrally coordinated boron and nitrogen atoms with (111) planes of c-BN arranged in a three-layer ABCABC... stacking sequence (Figure 6.1 (d)). The (0002) planes of w-BN (structurally identical to the (111) planes of c-BN) are arranged in a two-layer AB'AB'... stacking sequence (Figure 6.1 (c)).[11, 12] Both h-BN and r-BN are softer and consist of graphite-like hexagonal layers. The hexagonal layers of h-BN are arranged in a two-layer ab'ab'..., stacking sequence (Figure 6.1 (a)). For r-BN these layers are arranged in a three-layer (abcabc ..., stacking sequence (Figure 6.1 (b)). In both h-BN and r-BN, the in-plane atoms are bonded

through localized sp^2 hybridized orbital and the out-of-plane atoms are bonded by weakly interacting p orbitals.[11] In addition to these four phases, there are two other disordered BN phases: turbostratic BN (t-BN)[13] and amorphous BN (a-BN). In t-BN, the stacking of the sp^2 layers is random and is rotated randomly along the c axis. It produces a broad and diffuse diffraction pattern distinctly different from that of h-BN or r-BN.[13] a-BN is characterized by an atomic level structural disorder.

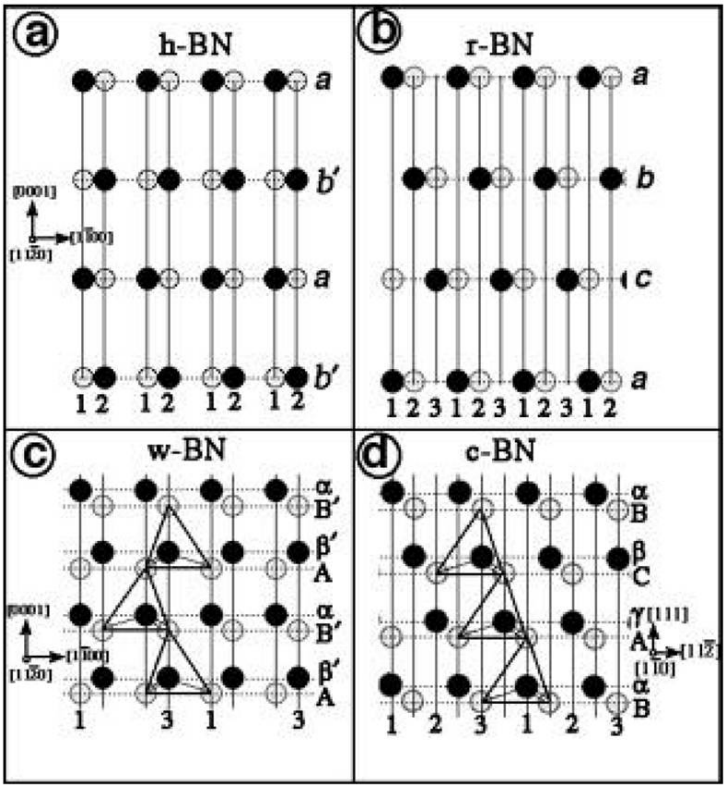

Figure 6.1: Projections of (a) h-BN, (b) r-BN, (c) w-BN and (d) c-BN (adopted from reference 10)

Among different forms of boron nitride, h-BN and c-BN are the most interesting and widely used. While h-BN is a soft lubricious material, c-BN is extremely hard. A table comparing properties of h-BN and c-BN is given below (Table 6.1). Hardness of c-BN (5000 Kg mm^{-2}) is inferior only to diamond, but its thermal and chemical stability is superior to diamond.[11] It is stable in air at

temperatures up to 1673 K, while diamond starts to decompose at 1073 K. c-BN is also chemically inert, exhibits extreme toughness (resistance to fracture) and can be

Table 6.1: Comparison of hexagonal and cubic boron nitride.

h-BN	**c-BN**
Soft	Hard
Lubricating	Abrasive
Thermally conductive	Thermally conductive
Oxidation resistant	Oxidation resistant
High temperature resistant	Non-reactive with ferrous alloys
Inert	
Electrically insulating	

produced in a variety of uniform grain sizes. In addition, properties such as thermal conductivity and toughness of BN may be altered to fit specific applications. c-BN, is synthesized from h-BN at high temperature (~1773 K) and pressure (60 kilobars).[14,15] This process changes the atomic structure of h-BN from hexagonal to cubic, same as that of graphite to diamond. The density of cubic boron nitride (3.49 g/cc) is close to that of diamond (3.51 g/cc). Hexagonal boron nitride is a naturally lubricious material and hence, it is often called white graphite. The primary use of h-BN is as an additive to a variety of other advanced materials. As an additive, boron nitride improves thermal shock resistance, mechanical properties, thermal conductivity and electrical properties and reduces friction. Its high temperature performance and lubricity make it an ideal additive to metal composite friction materials used in high-performance aircraft brakes.

Urea route has been found to be simple and useful for the synthesis of nitrides of different kinds.[16-18] The method involves heating a mixture of urea with an appropriate compound of choice at an appropriate temperature. The motivation behind using urea route is that urea yields NH_3 when heated at around 423 K and

thereby, can replace hazardous precursors traditionally used as nitrogen sources. Pure urea decomposes endothermically in following stages.[16-18]

$$NH_2CONH_2 \longrightarrow HCNO + NH_3 \text{ (413 K)}$$

$$NH_2CONH_2 \longrightarrow H_2CN_2 + H_2O \text{ (413 K)}$$

$$NH_2CONH_2 + HCNO \longrightarrow H_2NCONHCONH_2 \text{ (453 K, biuret)}$$

In an oxygen free atmosphere, the decomposition of urea also yields non-oxygen containing products like H_2CN_2, $H_4C_2N_4$ and $H_6C_3N_6$. On heating to higher temperature however, all the nitrogen compounds decompose. Urea route has been successfully exploited to synthesize several important binary and ternary nitrides, for example, GaN, InN, TiN, Fe_3Mo_3N and Co_3Mo_3N.[19,20] Nanoparticles and nanotubes of BN are obtained by heating H_3BO_3 with urea in 1:6 molar ratio at 1223 K.[19]

6.2 Scope of the present investigations

Hexagonal boron nitride (h-BN) is a graphite-like layered material with planar networks of BN hexagons stacked regularly. The h-BN also manifests variety of nanostructures just like that of graphite. After the discovery of C_{60} soccer ball,[21] various cage like structures of BN like $B_{12}N_{12}$, $B_{16}N_{16}$ and $B_{28}N_{28}$ have been realised both theoretically as well as experimentally.[22-25] As a structural analogue of carbon nanotubes (CNTs),[26] BN nanotube (BNNT) was first predicted in 1994[27] and synthesized in the following year.[28] Since then, it has become one of the most intriguing non-carbon nanostructures.[29] Similarly, in the light of the sensation caused by graphene in the last few years,[30-32] there has been some effort to prepare graphene analogues of BN. It is possible to peel off BN layers from a bulk BN crystal by micromechanical cleavage,[33] while few-layer BN can be made by

sonication[34,35] of BN particles or by using a high-energy electron beam.[36,37] There is, however, no report of the controlled chemical synthesis of graphene analogues of BN possessing a desired number of layers. Such a method would be useful for large-scale production of the material that can be used for preparing composites and in other applications. We have sought to explore such a synthesis of few-layer BN that permits the generation of materials with the control over the number of layers. In this purpose, we have employed the reaction of boric acid with urea at high temperatures, wherein we have varied the relative proportions of the two reagents. This simple method has enabled us to prepare graphene analogues of BN of varying thicknesses, exhibiting novel properties. We have also been interested in exploring vapor-phase synthesis of BN nanostructures with the expectation that such an approach may lead to graphene-like BN. With this purpose, we have investigated the reaction of BBr_3 and NH_3 at high temperature and found that nanopans as well as nanosheets formed by graphene-like BN can be accomplished by this means.

Nanomaterials have been widely used as additives to prepare polymer composites with a view to improve mechanical properties, the most important one among them being carbon nanotubes.[38,39] BN nanotubes have also been used for this purpose.[40-42] Incorporation of two-dimensional graphene has been shown to improve mechanical properties of polymer composites,[43,44] particularly significant being the recent observation[45] that there is great synergy when graphene is combined with a small amount of carbon nanotubes or nanodiamond. It has been suggested that varying the number of layers of two-dimensional additive would have a significant effect on the mechanical properties of polymer composites, the properties being favoured by a smaller number of layers.[43,46] In this context, we felt that it was purposeful to investigate the mechanical properties of polymer

composites prepared with graphene analogues of BN with varying number of layers. BN nanomaterials are expected to have advantage over other nanomaterials.[46] We have incorporated graphene-like BN samples of different number of layers, prepared by urea-boric acid reaction, in polymethylmethacrylate (PMMA) to study their mechanical properties. It was indeed found that the hardness (H) and elastic modulus (E) of PMMA improved significantly upon incorporation of graphene-like BN. The improvement depends sensitively on the number of layers, the beneficial effect increasing with the decreasing number of layers.

6.3 Experimental and related aspects

6.3.1 Urea route synthesis

In order to prepare graphene-like layers of BN, boric acid/urea mixtures with different molar ratios (1:6, 1:12, 1:24, 1:48 and 1:72) were dissolved in ~ 40 mL of Millipore water and heated at 338 K until the evaporation of water was complete. The dried mixture was heated (ramping rate of 3 K per minute) at 1173 K for 5 h in a N_2 atmosphere, yielding white products.

To functionalize the few-layer BN, 1 mg of BN was mixed with 3 mL of toluene followed by addition of 0.3 mL of trioctylamine or trioctylphosphine. The mixture was then sonicated for 15 min to obtain a clear and stable solution of BN. Composites of few-layer BN with PMMA were prepared by dissolving trioctylamine functionalized BN either in chloroform or dimethylformamide (DMF) solvents. Appropriate amounts of PMMA were added to these solutions under vigorous sonication and followed by drying at 313 K. BN-PMMA composites (containing 3 wt% of BN) obtained in this manner were pelletized and annealed at 100 ^{o}C for four hours.

6.3.2 Vapor phase synthesis

BN nanostructures could also be obtained by the reaction of BBr_3 vapor (carried by N_2 gas) with NH_3 vapor at 1223 K inside a quartz tube. A schematic diagram of the experimental set-up is shown in Figure 6.2. A glass slide was placed inside the quartz tube inclined on a quartz boat after the hot zone in the furnace to prevent free flow of the vapors. Both BBr_3 and NH_3 decompose at this temperature to produce BN nanostructures. A mixture of BN and NH_4Br was deposited on the colder zone after passing the glass slide. This material was collected and heated at 1023 K to obtain BN nanostructures in pure state. BN nanostructures were also formed in the hot zone of the reaction tube which was collected from the quartz boat.

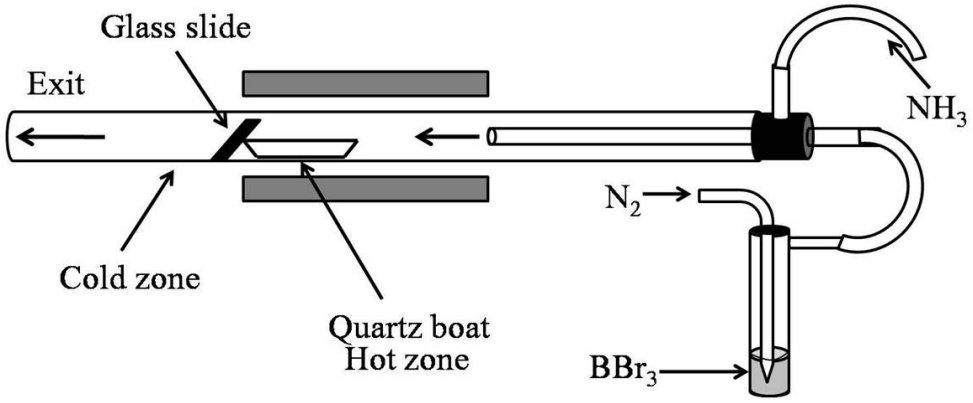

Figure 6.2: Experimental set-up used for the vapor phase synthesis of BN.

6.3.3 Characterization techniques

X-Ray diffraction (XRD): XRD patterns were recorded at 298 K with a Bruker-D8 X-ray diffractometer using Cu-Kα radiation

Electron Microscopy: Scanning electron microscopy images were recorded with a field emission scanning electron microscope (FESEM, FEI Nova-Nano SEM-600, Netherlands). TEM studies were carried with a FEI TITAN (cube) 80-300 and a JEOL JEM 3010 instrument operating at 300 kV. Atomic arrangement of hexagonal

BN (no reconstruction) was obtained from the FEI TITAN 80 - 300 kV aberrations corrected transmission electron microscope with a negative spherical aberration coefficient (Cs) of ~ -30 µm and a positive defocus about 8 nm, where atomic potentials appear with bright contrast in a dark background.[47] This bright atom imaging mode is an essential condition for imaging light atoms. Quantification of the Electron energy loss spectra (EELS) was obtained with a Gun monochromator (resolution better than 0.3 eV), camera length 73 mm and GIF aperture 1 mm, which gives collection angle ~ 3.336 mrad. Calculations were carried out using Gatan DM software to obtain B and N atomic percent.

Raman spectroscopy: Raman spectra were recorded with a LabRAM HR with the 633 nm line from HeNe laser. The excitation wavelength is 632.8 nm.

Infrared spectroscopy: Infrared spectra were recorded using Bruker IFS 66v/S spectrometer.

Atomic force microscopy: AFM measurements were performed using a NanoMan instrument using tapping mode. A dilute dispersion of BN flakes in acetone was dropped on a SiO_2 substrate and was used for AFM measurements.

Gas adsorption: QUANTACHROME QUADRASORB-1C surface area analyzer was used for gas adsorption studies. Brunauer Emmett Teller (BET) surface areas were obtained from a nitrogen adsorption-desorption isotherm at 77 K. The CO_2 adsorption was carried out at 195 K (1:1 mixture of dry ice and acetone). Hydrogen adsorption was carried out at liquid nitrogen temperature (77 K).

Mechanical properties: Mechanical properties of BN-PMMA composites were investigated using a nano-indenter (Triboindenter of Hysitron, Minneapolis, USA) having in-situ imaging capability. Nano-indentation was carried out on pellets of the BN-PMMA composites. The instrument continuously monitors and records the load

(P) and displacement (h) of the indenter with force and displacement resolutions of 1 nN and 0.2 nm, respectively. A Berkovich tip (three-sided pyramidal diamond tip) of diameter 100 nm was used for the nano-indentation. Loading and unloading rates of 0.1 mN/s and a hold time of 10 s at a peak load of 1 mN were employed. A minimum of 30 indentations were performed on each pellet. Since the mechanical properties extracted from the nano-indentation are sensitive to the tip geometry, the tip area function was calibrated before determining the mechanical properties.

6.4 Results and discussion

6.4.1 Graphene analogues of BN by the urea route

The high temperature reaction of urea and boric acid in the molar ratio of 1 : x with x = 6, 12, 24, 48 and 72 yields graphene-like BN with different number of layers. XRD patterns of these products exhibit the characteristic (002) and (100) reflections of hexagonal BN at d = 3.5 and 2.1 Å, respectively (see Figure 6.3). The

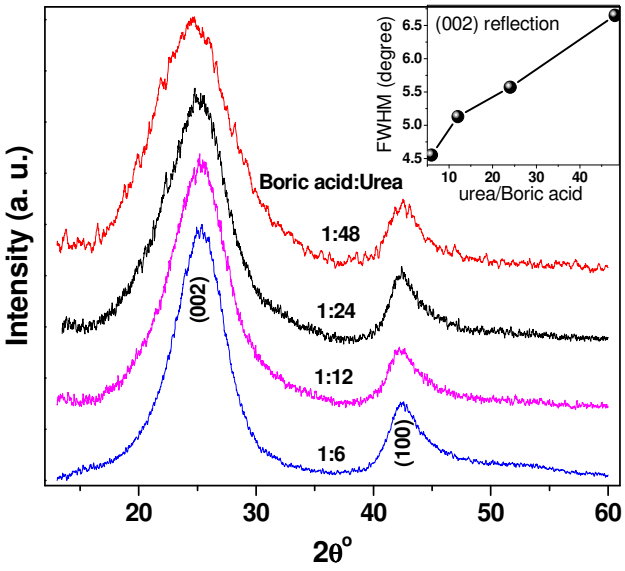

Figure 6.3: XRD patterns of few-layer BN samples, prepared with different boric acid : urea ratio, inset shows the width of (002) reflection as function of urea/boric acid.

width of (002) reflection increases with the increasing proportion of urea in the starting reaction mixture as shown in the inset of Figure 6.3. The *d*-spacing corresponding to the (002) plane increases slightly when the boric acid to urea ratio was 1:48, indicating lower sheet to sheet registry in the sample. Raman spectra of all the samples show a band centered at 1373 cm^{-1} due to the E_{2g} tangential mode[48] and does not exhibit any significant change with the increasing proportion of urea in the reaction mixture. Fourier transform infrared (FTIR) spectra show peaks at 1384 and 800 cm^{-1} corresponding to in-plane B-N transverse optical mode and out-of-plane B-N-B bending mode respectively, along with the N-H stretching band due to the amino groups on the surface.[49,50]

TEM investigations of the products reveal the presence of single as well as few-layer BN. In Figure 6.4, we show representative high resolution TEM images of

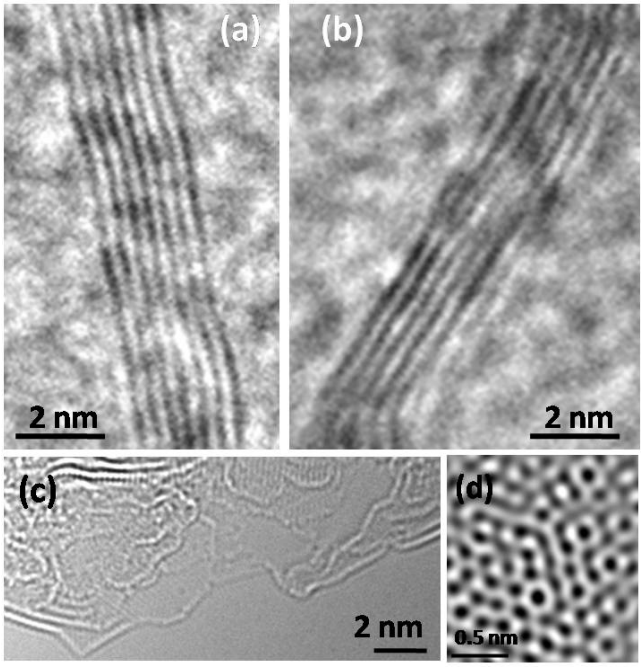

Figure 6.4: TEM images of few-layer BN prepared with (a) 1:12, (b) 1:24 and (c) 1:48 boric acid : urea mixture. (d) High-resolution TEM image of few-layer BN prepared with 1:48 boric acid : urea mixture.

some of the samples synthesized with different boric acid to urea ratios. The interlayer spacing in all the cases is ~ 3.5 Å corresponding to the (002) planes of *h*-BN. In bulk BN, this distance is 3.3 Å. The images in Figures 6.4 (a) and (b) correspond to samples prepared with boric acid to urea ratios of 1:12 and 1:24 showing the presence of eight and six layers of BN respectively. The image in Figure 6.4 (c), obtained from the sample prepared with 1:48 boric acid : urea ratio shows the presence of single layers along with two-layers. This image also shows evidence for curves and bends in the layers representing a possible intermediate stage in the formation of nanotube by rolling. The hexagonal atomic arrangement of BN crystal can be seen from the high-resolution TEM image in Figure 6.4 (d) with the incident electron beam along the <001> direction. The distance between two neighboring bright dots in the hexagon is 1.44 Å which matches up with the known length of the B-N bond. The distance between the alternating dots in the hexagon is 2.49 Å, corresponding to the (100) lattice constant of *h*-BN. This distance describes the

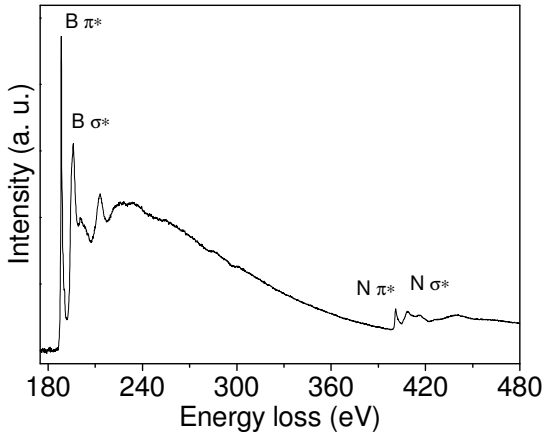

Figure 6.5: EEL spectrum of BN nanosheets prepared by the urea route.

separation between nearest N or B atoms.[35-37] Thus, TEM studies of the products of urea-boric acid reaction reveal the formation of graphene analogues of BN, the layer thickness decreasing with increasing urea concentration in the reaction mixture. The

observation of a single layer BN with a high proportion of urea in the reaction mixture is significant. Electron energy loss spectroscopy (EELS) carried out in the microscope shows K-edge absorptions of B and N at 188 and 401 eV respectively (Figure 6.5). Both the core edges exhibit π^* and σ^* peaks, characteristic of sp^2 hybridized BN.[34] EELS measurements also reveal the composition of the product to be stoichiometric.

More reliable information on the number of layers in the BN samples was obtained by the AFM examination of the products as shown in Figure 6.6. The average sheet areas varied between 0.1 μm × 0.1 μm and 1 μm × 1 μm depending on

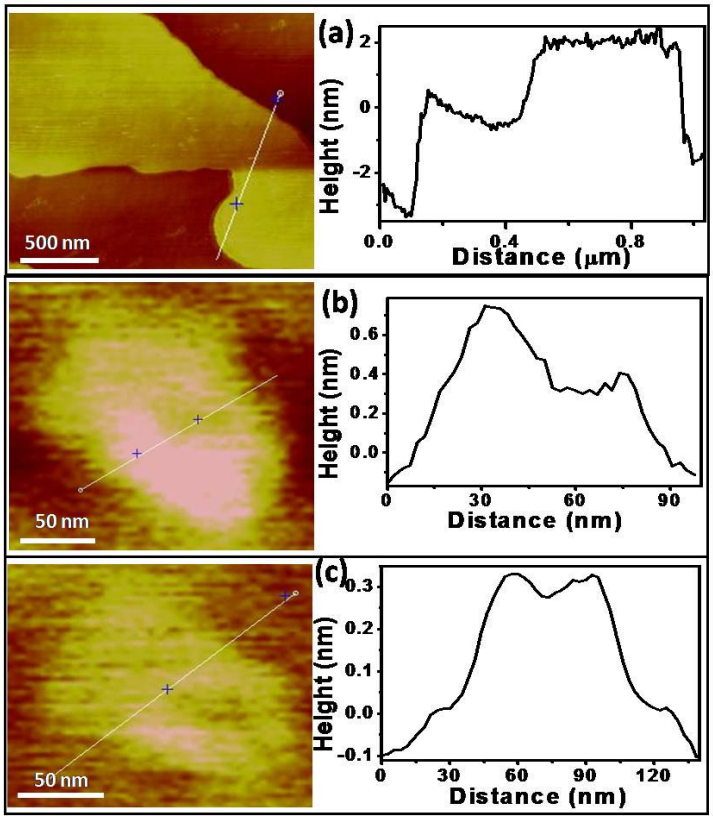

Figure 6.6: AFM images and corresponding height profiles of few-layer BN prepared with different boric acid : urea molar ratios (a) 1:12, (b) 1:24 and (c) 1:48.

the starting reactant ratio. Figure 6.6 (a) shows a micrometer size BN flake obtained with a boric acid to urea ratio of 1:12. The step-like increase in the height profile from 3 to 5 nm along the white line shown in the image represents an increase in the number of layers from 8 to 14 layers. The AFM image in Figure 6.6 (b) of a BN flake (150 X 200 nm^2) obtained with a reactant ratio of 1:24 exhibits a step-like increase in height from 0.4 to 0.8 nm corresponding to single and bi-layers. Figure 6.6 (c) shows an AFM image and the corresponding height profile of a single-layer BN obtained from the sample prepared with a boric acid to urea ratio of 1:48. AFM images with larger scanning area show multiple BN flakes with thickness in the 0.5-0.9 nm range. In Figure 6.7, we show the histograms of layer thickness obtained from an analysis of the AFM images. We clearly see that with the increasing

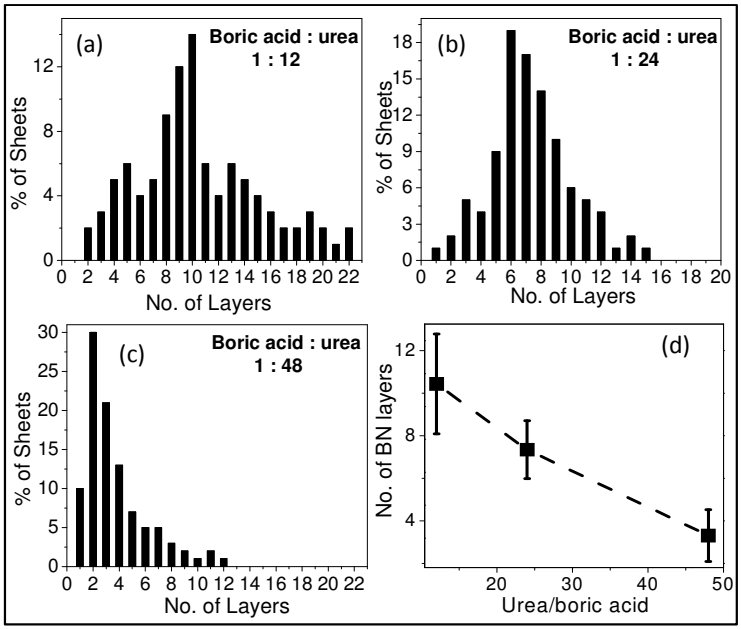

Figure 6.7: Bar diagrams derived from an analysis of AFM images, showing the layer-distribution of few-layer BN prepared with different boric acid : urea molar ratios of (a) 1:12, (b) 1:24 and (c) 1:48. (d) Variation of the average layer thickness vs urea/boric acid ratio.

proportion of the urea in the starting reaction mixture, the number of BN layers decreases. While the number of layers is between 8 and14 for the sample with the reactant ratio of 1:12, we obtain ~1-4 layers of BN with a boric acid to urea ratio of 1:48 (see Figures 6.7 (a), (b) and (c)). In Figure 6.7 (d), we show the variation of the average number of layers with the reactant ratio. Further increase in urea content in the reaction mixture had little effect on the number of BN layers in the product.

We have determined the BET surface areas of the few-layer BN samples by employing N_2 adsorption-desorption isotherms (Figure 6.8). The surface area increases with the increasing proportion of urea in the reaction mixture. We consider

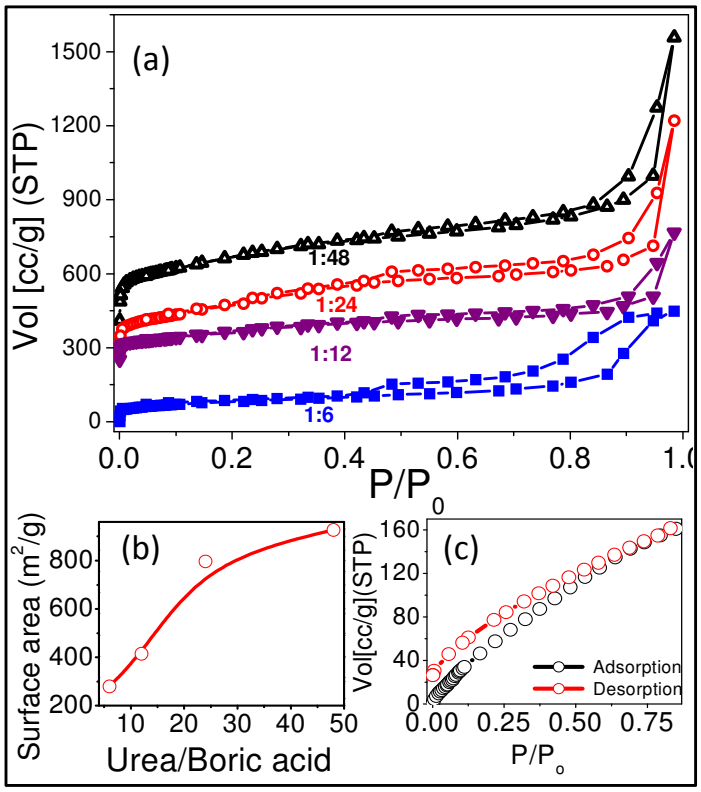

Figure 6.8: (a) Nitrogen adsorption-desorption isotherms of few-layer BN prepared with different boric acid/urea ratios. Plots for boric acid/urea ratios of 1:12, 1:24 and 1:48 have been moved vertically upward by 150, 270 and 400 units, for a clear representation. (b) The variation of the BET surface area *vs* urea/boric acid precursor ratio. (c) CO_2 adsorption-desorption isotherms at 195 K and 1 atmp for the BN sample with highest surface area

this to reflect the decrease in the number of layers, rather than the variation of the area of the BN flakes. The variation of the surface area with the proportion of urea is shown in Figure 6.8 (b). To the best of our knowledge, such high surface area BN samples are not reported hitherto. Remarkably, BN with the highest surface area adsorbs 32 wt% of CO_2 at 195 K and p/p_0 = 0.85 as shown in Figure 6.8 (c). This sample, however, adsorbs only ~ 0.5 wt% of H_2 at 77 K and 1 atmosphere.

As-prepared BN layers are insoluble in both polar and nonpolar solvents. For possible applications of few-layer BN in composites and elsewhere, it is necessary to functionalize the samples. We have accomplished this by making use of the inherent

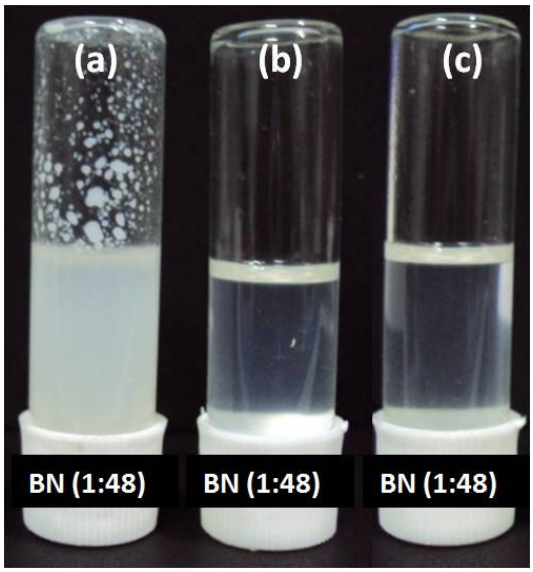

Figure 6.9: Photographs of solutions of (a) as-prepared few-layer BN along with BN functionalized with (b) TOP and (c) TOA in toluene. The BN sample was prepared with boric acid : urea ratio of 1:48.

electron deficiency of boron to form Lewis acid-Lewis base adducts, by interacting few-layer BN with a Lewis base.[51] Thus, adducts with trioctylamine (TOA) and trioctylphosphine (TOP) are soluble in non-polar solvents such as toluene, heptane and benzene. This behavior is different from the dispersion of

BN in polar solvents such as dimethylformamide. Figure 6.9 shows photographs of clear solutions of functionalized BN in toluene.

Prof. U. V. Waghmare and Dr. K. P. S. S. Hembram have carried out first-principles simulations on few-layer BN. The calculation results show that energetically it is easy for few-layer BN to form stacking faults that involve slips and twists of adjacent planes resulting in inhomogeneity in the interplanar distances, as revealed by high-resolution TEM images of the few-layer BN samples. Interestingly, the interplanar distance in graphene analouges of BN is larger than that of the bulk BN. This is counterintuitive but is in agreement with experiment (see Table 6.2). Cohesive energies of few-layer BN sheets converge close to bulk values for $n > 4$, indicating that the graphene-like BN sheets are quite stable.

Table 6.2: Lattice parameters (a) and inter-layer distances (d) in BN structures

BN structures	Experiment[(a,b,c)]		Theory	
	a (Å)	d (Å)	a (Å)	d (Å)
Bulk	2.5	3.3	2.48	3.2
Two or few layers	2.5	3.5	2.48	3.3

(a) Ref. 35, (b) Ref. 52 and (c) our experimental results

The bulk modulus of graphene analouges of BN is calculated to be 160 Pa.m, as compared to 202 Pa.m of graphene, showing the relative softness of BN. Calculations also show a weaker H_2 adsorption on BN layers compared to graphene in accord with our experimental results

6.4.2 BN nanopans and other nanostructures by the vapour phase route

We have explored the vapor phase reaction of BBr_3 and NH_3 at 950 ^oC for obtaining nanostructures of graphene-like BN. The reaction involved can be written as follows:

$$BBr_3 + 2NH_3 \xrightarrow{1223\ K} BN + NH_4Br + Br_2 + H_2$$

After carrying out the reaction for ~ 90 minutes, solid deposits were found in both the hot and cold zones of the reaction tube. The solid deposited in the cold zone contained BN nanostructures along with some NH_4Br. On heating this product at 1023 K, pure BN nanostructures were obtained. The XRD pattern and Raman spectrum of so obtained BN are shown in Figure 6.10 (a) and (b) respectively. FESEM and TEM examinations showed these nanostructures to be sheets of BN with several micrometers in lateral dimension. In Figure 6.11 (a), we show TEM image of a typical BN sheet. The high resolution TEM in

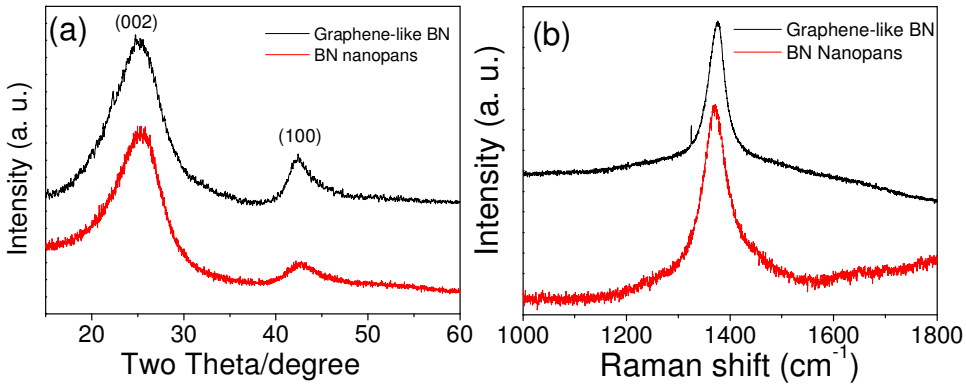

Figure 6.10: (a) XRD patterns and (b) Raman spectra of graphene-like BN and BN nanopans.

Figures 6.11 (b) shows the presence of two and three layer BN. A representative AFM image of BN sheets along with the associated height profile is shown in

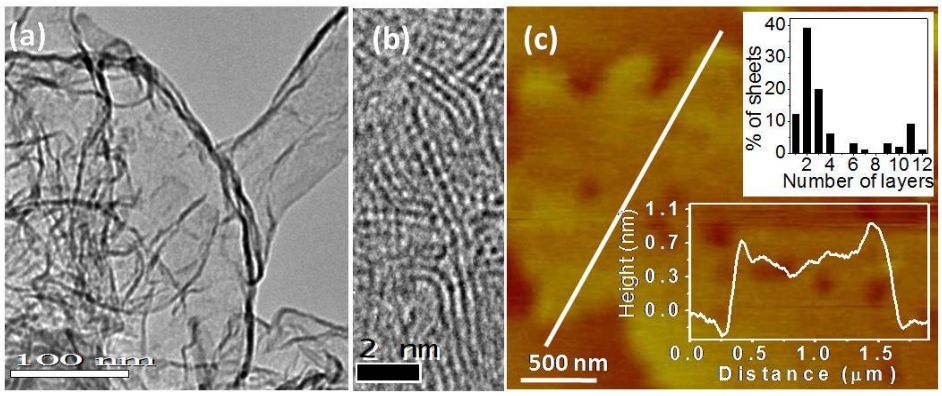

Figure 6.11 (a) TEM image of graphene-like sheets of BN obtained in the cold zone of the reaction chamber. (b) High resolution TEM image showing BN layers (c) AFM image of graphene-like BN. Inset in (c) shows a distribution of layer thickness of graphene-like BN

Figure 6.11 (c). The inset of Figure 6.10 (c) shows the histogram of the layer thickness of the BN sheets obtained on the basis of an analysis of the AFM images. We see that the BN sheets mainly contain one to three layers. The graphene-like BN found here is similar to that obtained by the high-temperature reaction of urea and boric acid.

The material deposited in the hot zone of the reaction tube was found to contain pan-like nanostructures with an average outer diameter of 110 nm (Figure 6.12). Most of the pan-like nanostructures have a rim with a width of around 25 nm and a central portion with a diameter of ~ 40 nm as can be seen from the TEM image given in inset (a) of Figure 6.12 (a). The TEM image clearly distinguishes the rim and the bottom part of the nanopan. Atomic force microscope images clearly reveal the nature of the nanopans (Figure 6.12 (b)). The AFM height profile shows a maximum of ~ 0.7 nm followed by a dip and another maximum of a similar height. Based on this we can conclude that the nanopan has a wall ~ 0.7 nm in height and a bottom with a thickness of ~ 0.4 nm.

The thickness of 0.4 nm corresponds to a single layer of BN. The height of 0.7 nm corresponds to a strip of BN containing three six-membered rings. We show a high resolution TEM image of the single layer BN constituting the bottom of the nanopan in inset (b) of Figure 6.12, which clearly shows the hexagonal atomic

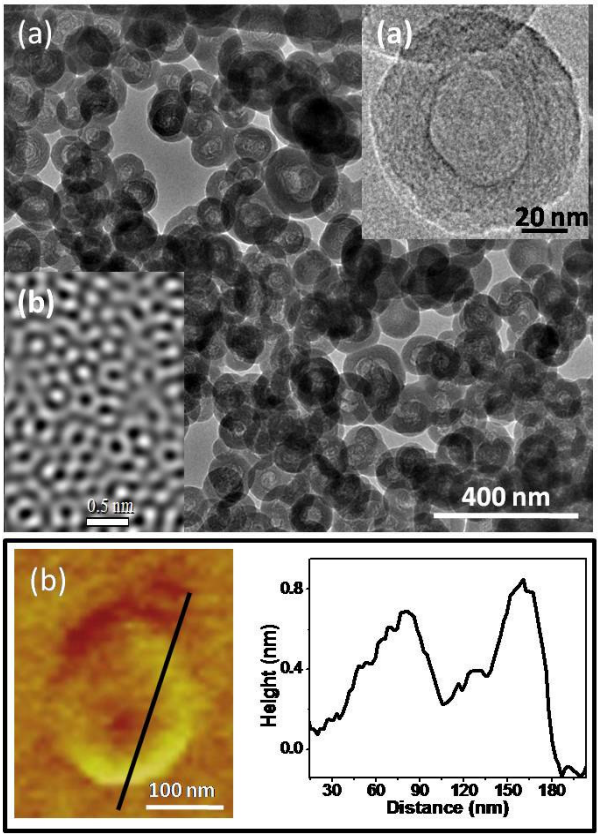

Figure 6.12: (a) TEM image of BN nanopans found in the hot zone of the reaction chamber. Inset (a) shows the TEM image of a single nanopan clearly delineating the ring and central bottom portions. Inset (b) shows high resolution TEM image of the single layer BN forming at the bottom of the nanopans. (b) AFM image of BN nanopan and the associated height profiles.

arrangement of BN crystal. The distance between two neighbouring bright dots in this image represents the B-N bond length. The (100) lattice constant of BN represented by alternating dots in the hexagons is 2.46 Å, (literature value of B-N

distance is 1.44 Å).[35-37]

The XRD pattern of the nanopans exhibits two reflections at d = 3.5 and 2.1 Å corresponding to the (002) and (100) planes of BN respectively (Figure 6.10 (a)). Selected area electron diffraction patterns also show reflections due to these two planes. The Raman spectrum of the nanopans shows the characteristic band of BN centred at 1370 cm^{-1} (Figure 6.10 (b)), while the infrared spectrum exhibits bands at 1382 and 801 cm^{-1} due to B-N transverse optical mode and B-N-B out-of-plane bending mode respectively. The electron energy loss spectrum (EELS) of the nanopans establishes the elemental composition to correspond to BN. The spectrum shows the K shell ionization edges due to B and N at 188 and 401 eV respectively, characteristic of sp^2-hybridization. These bands occur as doublets arising from π^* and σ^* states. The curling of growing BN along the pan circumference is very interesting. Similar spherical curling of the basal planes under electron irradiation is a general phenomenon in graphite-like structure.[53-55] In carbon systems, curling occurs by the formation of pentagons which is not possible in the case BN as it requires B-B or N-N bonds. The formation of curled clusters in boron nitride under electron irradiation has been explained for the formation of four-membered BN rings.[53] Similar rings are used for the construction of closed spherical boron-nitrogen analogues of fullerenes such as $B_{30}N_{30}$[56] or $B_{12}N_{12}$.[57] Four-membered BN rings ensure a perfect alternation of boron and nitrogen and lead to curled structures but would have significantly more strain than five-membered rings.

In Figure 6.13 (a), we show a schematic of the nanopan which incorporates all the features mentioned earlier. Figure 6.13 (b) shows a high resolution image of the walls showing spots separated by ~ 2.5 Å. The structural

diagram given in Figure 6.13 (b) explains the distances that define the wall of the nanopans. The volume of nanopan works out to be around 400 nm^3.

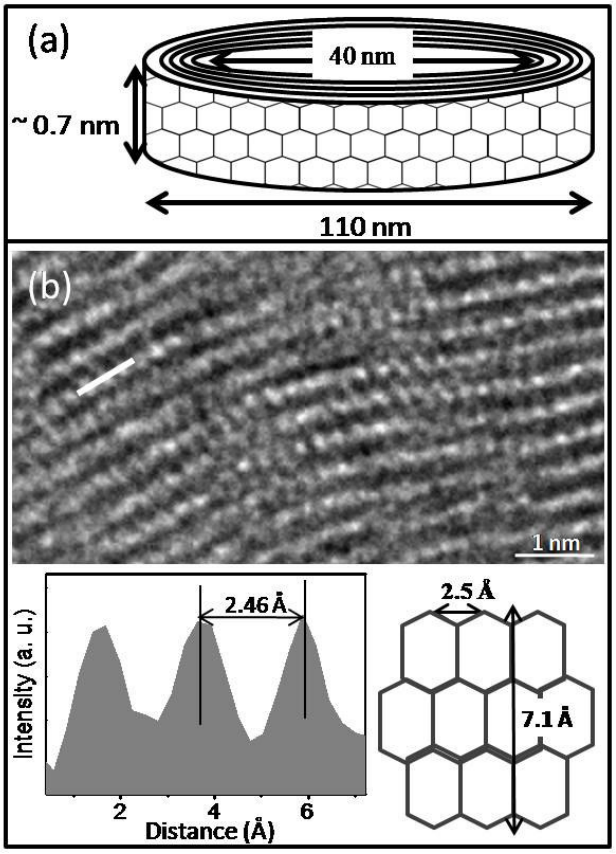

Figure 6.13 (a) Schematic describing of the nanopans, (b) high resolution TEM image of the walls of the nanopan. The spots are separated by 2.5 Å along the wall. Inset in (b) shows the structure of the wall and explains how the 2.5 Å is related to the structure.

6.4.3 Mechanical properties

We have investigated mechanical properties of composites of PMMA with graphene-like BN prepared by the high temperature reaction of urea-boric acid mixtures. In Figure 6.14, we show the force-displacement (P-h) curve of pure PMMA along with those of the BN-PMMA composites incorporating 3 wt% of

three-layered BN prepared from DMF and chloroform solvents. We see that the maximum depths of penetration (h_{max}) for BN-PMMA composites are significantly

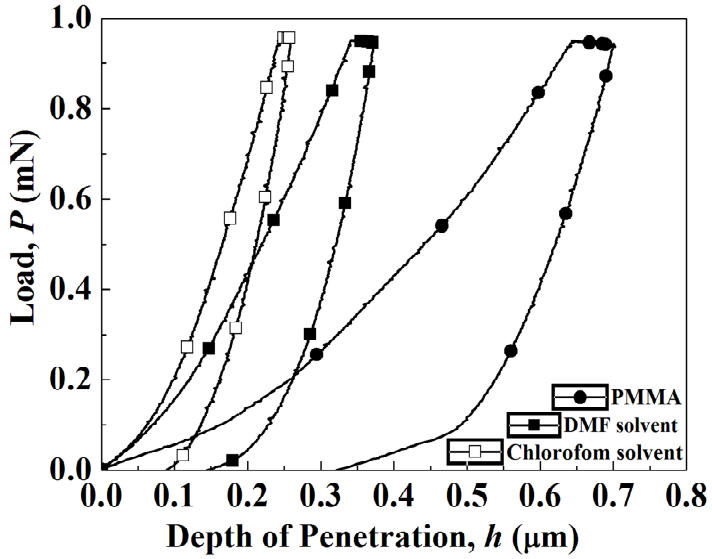

Figure 6.14: Typical load-penetration depth (P-h) curves of BN-PMMA composites containing 3 wt% of three layer BN, prepared with chloroform and DMF solvent.

lower than that of pure PMMA. The h_{max} of the composite prepared from chloroform is lower than that prepared from DMF. The hardness and Elastic modulus values of the composites were calculated from the P-h curves by fitting the unloading part of the curve with a method proposed by Oliver and Pharr[58] and the results are presented in Table 6.3.

We show the variation of H and E of the BN-PMMA composites as a function of urea to boric acid ratio used for the preparation of BN in Figures 6.15 (a) and (b) respectively. These figures reveal that both H and E of PMMA have increased markedly upon incorporation of graphene-like BN. The variation of H and E with the number of layers of the BN additive is shown as insets in Figure 6.15. It can be clearly seen that both H and E increase significantly with decreasing number of layers. Furthermore, the composites prepared in chloroform solvent gives better mechanical properties than those from DMF solvent. The maximum increase of H

and E (prepared from chloroform solvent) were found to be 125 and 130%, respectively in the case of PMMA incorporating three-layer BN. For composite prepared with DMF solvent the increases were 108 and 118% for H and E, respectively.

Table 6.3: Mechanical properties of pure PMMA and BN-PMMA composites obtained using instrumented indentation technique.

	Urea/Boric acid	No of layers	Surface area of BN (m^2/g)	Hardness (GPa)	Elastic Modulus (GPa)
PMMA				0.137 ± 0.017	2.2 ± 0.12
$CHCl_3$ solvent	12	10	415	0.25 ± 0.002	4.41 ± 0.022
	24	7	797	0.271 ± 0.014	4.78 ± 0.23
	48	3	927	0.31 ± 0.006	5.11 ± 0.18
DMF solvent	12	10	415	0.195 ± 0.009	3.42 ± 0.084
	24	7	797	0.239 ± 0.022	4.32 ± 0.34
	48	3	927	0.285 ± 0.091	4.81 ± 0.13

These results demonstrate that the mechanical properties of polymer composites containing two-dimensional nanomaterials depend significantly on the number of layers. The increase in the strength and modulus found by us is much greater to that reported for BN nanotubes as well as for carbon nanotubes.[38-42] They are also superior to those reported for single and four layer graphene.[43,44] It is well known that the mechanical properties of composites depend primarily on the efficiency of load transfer between the matrix and the reinforcement phase, which is aided by a strong interfacial bond between the constituent phases. As the number of BN layers decreases, the effective surface area increases, facilitating greater

interaction between BN and PMMA. This is the reason why composite with the least number of BN layers has the highest strength.[43,46]

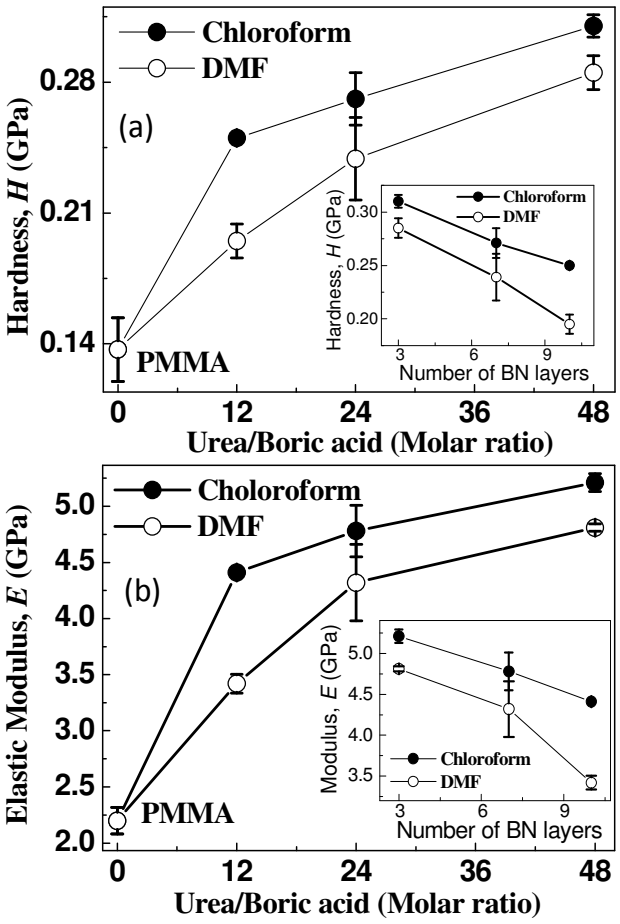

Figure 6.15: Variation of (a) hardness and (b) elastic modulus of BN-PMMA composites prepared with chloroform and DMF solvents as a function of urea to boric acid ratio used for the synthesis of BN. Insets show the variation of hardness and elastic modulus as a function of number of BN layers.

6.5 Conclusions

In conclusion, single- and few-layer graphene-like BN flakes could be prepared successfully by reacting boric acid with different proportions of urea at 1173 K. The number of BN layers decreases with the increase in urea content in the reaction mixture, allowing a control on the number of BN layers. To the best

of our knowledge, this is the first report of a bottom-up chemical synthesis of few-layer BN, enabling a large-scale production. The surface area of the BN layers increases with the decrease in layer thickness as expected, the sample with lowest layer thickness exhibiting a surface area of 927 m^2/g and high CO_2 uptake. Few-layer BN can be functionalized and solubilized by employing Lewis bases.

In a different approach, we have also been able to synthesize novel nanostructures of BN formed by graphene-like species, using vapor phase reaction of BBr_3 and NH_3 at high-temperatures. While nanosheets of BN containing one to three layers occur in the cold zone of the reaction chamber, nanopans with a single layer BN at the bottom occur in the hot zone. The nanopans are formed in abundance and may find useful applications and provides a new direction in which gas phase reactions are employed to obtain interesting nanostructures.

We have also systematically investigated the role played by the number of BN layers in determining the mechanical properties of a composite. Experimental results show that both the stiffness and the hardness of the PMMA are highest for the composite with the smallest number of BN layers. These results demonstrate that the mechanical properties of polymer composites containing 2-D nanomaterials depend significantly on the number of layers, with the properties improving linearly with decreasing number of layers. The larger surface area with fewer layers, enhanced interaction of BN with the polymer and hence improve the properties.

References

1. E. Hernandez, C. Goze, P. Bernier and A. Rubio, *Phys. Rev. Lett*., **80**, *4502,* 1998.

2. A. P. Suryavanshi, M. Yu, J. Wen, C. Tang and Y. Bando, *Appl. Phys. Lett.,* **84**, *2527,* 2004.

3. P. Kim, L. Shi, A. Majumdar and P. L. McEuen, *Phys. Rev. Lett.*, **87**, *215502,* 2001.

4. X. Blase, A. Rubio, S. G. Louie and M. L. Cohen, *Europhys. Lett.*, **28**, *335,* 1994.

5. K. Watanabe, T. Taniguchi and H. Kanda, *Nat. Mater.*, **3**, *404,* 2004.

6. G. Lee, M. Park, J. Kim, J. I. Lee and H. G. Yoon, *Composties: Part A*, **37**, *727,* 2006.

7. G. Pezzotti, I. Kamada and S. J. Miki, *Eur. Ceram. Soc.*, **20**, *1197,* 2000.

8. W. H. Balmain, *J. Prakt. Chem.*, **27**, *422,* 1842.

9. B. T. Kelly: *Physics of Graphite,* Applied Science Publisher, London, 1981.

10. J. Huang and Y. T. Zhu, *Defect and Diffusion Forum,* **186,** *1,* 2000.

11. P. B. Mirkarimi, K. F. Mccartly and D. L. Medlin*, Mater. Sci. Eng. R***,** **21**, *47,* 1997.

12. A. R. Verma and P. Krishna, *Polymorphism and Polytypism in Crystals,* John Wiley & Sons Inc., New York, 1966.

13. V. L. Solozhenko, *Thermochimica Acta,* **218,** *395,* 1993.

14. A. V. Kurdyumov, V. F. Britun and I. A. Petrusha, *Diamond Related Mater.*, **5,** *1225,* 1996.

15. G. Demazeau, *Diamond Relat. Mater.*, **4,** *284,*1995.

16. Q. Yu and G. Lian, *J. Am. Ceram. Soc*., **87**, *352,* 2004.

17. S. Podsiadlo, *Thermochim. Acta*, **256**, *367,* 1995.

18. S. Podsiadlo, *Thermochim. Acta,,* **256**, *375,* 1995.

19. A. Gomathi, C. N. R. Rao, *Mater. Res. Bull.*, **41**, *941*, 2006.

20. A. Gomathi, *Mater. Res. Bull.*, **42**, *870*, 2007.

21. H. W. Kroto, J. R. Health, S. C. Obrien, R. F. Curl and R. E. Smalley, *Nature*, **318**, *162*, 1985.

22. F. Jensen and H. Toflund, *Chem. Phys. Lett.,* **201**, *89*, 1993.

23. G. Seifert, P. W. Fowler, D. Mitchell, D. Porezag and T. Frauenheim, *Chem. Phys. Lett.*, **268**, *352*, 1997.

24. O. Stephan, Y. Bando, A. Loiseau, F. Willaime, N. Shramchenko, T. Tamiya and T. Sato, *Appl. Phys. A*, **67**, *107*, 1998.

25. T. Oku, A. Nishiwaki and I. Narita, *Sci. Tech. Adv. Mater*, **5**, *635*, 2004.

26. S. Iijima, *Nature*, **354**, *56*, 1991.

27. A. Rubio, J. L. Corkill and M. L. Cohen, *Phys. Rev. B*, **49**, *5081*, 1994.

28. N. G. Chopra, R. J. Luyken, K. Cherrey, V. H. Crespi, M. L. Cohen, S. G. Louie and A. Zettl, *Science*, **269**, *966,* 1995.

29. D. Golberg , Y. Bando, C. C. Tang and C. Y. Zhi, *Adv. Mater.*, **19**, *2413*, 2007.

30. K. S. Novoselov, A. K. Geim, S. V. Morozov, D. Jiang, Y. Zhang, S. V. Dubonos, I. V. Grigorieva and A. A. Firsov, *Science,* **306,** *666*, 2004.

31. A. K. Geim and K. S. Novoselov, *Nat. Mater.*, **6**, *183,* 2007.

32. C. N. R. Rao, A. K. Sood, K. S. Subrahmanyam and A. Govindaraj, *Angew. Chem., Int. Ed*, **48**, *7752,* 2009.

33. D. Pacile, J. C. Meyer, C. O. Girit and A. Zettl, *Appl. Phys. Lett.*, **92**, *133107,* 2008.

34. W. Q. Han, L. J. Wu, Y. M. Zhu, K. Watanabe and T. Takiguchi, *Appl. Phys. Lett.*, **93**, *223103,* 2008.

35. C. Zhi, Y. Bando, C. Tang, H. Kuwahara and D. Golberg, *Adv. Mater.*, **21**, *2889,* 2009.

36. J. C. Meyer, A. Chuvilin, G. A. Siller, J. Biskupek and U. Kaiser, *Nano Lett.*, **9**, *2683*, 2009.

37. C. Jin, F. Lin, K. Suenaga and S. Iijima, *Phys. Rev. Lett.*, **102**, *195505,* 2009.

38. W. J. Lee, S. E. Lee and C. G. Kim, *Compos. Struct.*, **76,** *406*, 2006.

39. L. Q. Liu and H. D. Wagner, *Compos. Interface*, **14,** *285,* 2007.

40. P. K. Mallick, *Fiber-reinforced composites*, Marcel Dekker, New York, *130*, 1993

41. M. Cadek, J. N. Coleman, V. Barron, K. Hedicke and W. J. Blau *Appl. Phys. Lett.*, **81,** *1523*, 2002.

42. C. Y. Zhi, Y. Bando, W. L. Wang, C. C. Tang, H. Kuwahara and D. Golberg, *J Nanomaterials*, **1,** *642036*, 2008.

43. T. Ramanathan, A. A. Abdala, S. Stankovich, D. A. Dikin, M. Herrera-Alonso, R. D. Piner, D. H. Adamson, H. C. Schniepp, X. Chen, R. S. Ruoff, S. T. Nguyen, I. A. Aksay, R. K. Prudhomme and L. C. Brinson, *Nat. Nanotechnol.*, **3,** *327*, 2008.

44. B. Das, E. K. Prasad, U. Ramamurty and C. N. R. Rao, *Nanotechnology*, **20,** *125705*, 2009.

45. E. K. Prasad, B. Das, U. Maitra, U. Ramamurty and C. N. R. Rao, *Proc. Natl. Acad. Sci.*, **106,** *13186*, 2009.

46. C. Zhi, Y. Bando, C. Tang, H. Kuwahara and D. Golberg, *Adv. Mater.*, **21**, *2889*, 2009.

47. C. L. Jia, M. Lentzen, K. Urban, *Science*, **299**, *870,* 2003.

48. S. Saha, D. V. S. Muthu, D. Goldberg, C. Tang, C. Zhi, Y. Bando and A. K. Sood, *Chem. Phys. Lett.*, **421**, *86,* 2006.

49. C. Zhi, Y. Bando, C. Tang and D. Golberg, *J. Am. Chem. Soc.*, **127**, *17144,* 2005.

50. Y. L. Gu, M. T. Zheng, Y. L. Liu and Z. L. Xu, *J. Am. Ceram. Soc.*, **90**, *1589,* 2007.

51. S. Pal, S. R. C. Vivekchand, A. Govindaraj and C. N. R. Rao, *J. Mater. Chem.*, **17**, *450,* 2007.

52. R. T. Paine and C. K. Narula, *Chem. Rev.*, **90**, *73*, 1990.

53. F. Banhart, M. Zwanger and H. J. Muhr, *Chem. Phys. Letts.*, **231**, *98,* 1994.

54. O. Stephan, Y. Bando, A. Loiseau, F. Willaime, N. Shramchenko, T. Tamiya and T. Sato, *Appl. Phys. A,* **67**, *107,* 1998.

55. F. Xu, Y. Xie, X. Zhang, S. Zhang, X. Liu and X. Tian, *Inorg. Chem*., **43**, *82,* 2004.

56. I. S. Dumitrescu, I. Haiduc and D. B. Sowerby, *Inorg. Chem.*, **32**, *3755,* 1993.

57. F. Jensen and H. Toftlund, *Chem. Phys. Letts*, **201**, *89,* 1993.

58. W. C. Oliver and G. M. Pharr, *J. Mater. Res.*, **7**, *1564*, 1992.

CHAPTER 7

Multiferroic and magnetoelectric properties of core-shell $CoFe_2O_4$@$BaTiO_3$ nanocomposites*

Summary

This chapter presents the multiferroic and magnetoelectric properties of core-shell $CoFe_2O_4$@$BaTiO_3$ nanostructures. Core-shell $CoFe_2O_4$@$BaTiO_3$ nanoparticles and nanotubes have been prepared using a combination of solution processing and high temperature calcination. Both the core-shell nanostructures exhibit magnetic and dielectric hysteresis at room temperature and magnetoelectric effect. The dielectric constant of both the nanocomposites decreases upon application of magnetic field. The core-shell nanoparticles exhibit 1.7% magnetocapacitance around 134 K at 1 T, while the core-shell nanotubes show a remarkable 4.5% magnetocapacitance around 310 K at 2 T.

---

*A paper based on this study has been published in *Appl. Phys. Lett.* (**2010**).

7.1 Introduction

Multiferroics are materials with coexistence of at least two primary ferroic orders, ferroelectric, ferromagnetic or ferroelastic.[1-3] However, the definition has been expanded recently to include non-primary order parameters, like antiferromagnetism or ferrimagnetism. In general, multiferroic materials have a spontaneous magnetization that can be reoriented by an applied magnetic field, a spontaneous polarization that can be reoriented by an applied electric field and a spontaneous deformation that can be reoriented by an applied stress. Very few multiferroic materials exist in nature or have been synthesized in the laboratory. This includes few perovskite transition metal oxides, rare-earth manganites and ferrites, bismuth compounds ($BiFeO_3$ and $BiMnO_3$) and spinel chalcogenides ($ZnCr_2Se_4$). Apart from single phase multiferroics, composites and heterostructures exhibiting more than one ferroic order parameters are studied extensively. For example, magnetic thin films on piezoelectric substrates and nanocomposites of magnetic and ferroelectric materials are shown to exhibit multiferroic properties.[4-7] Besides scientific interest to understand the fundamental physics behind, multiferroics have potential for applications as actuators, switches, magnetic field sensors or new types of electronic memory devices.

Materials with simultaneous ferromagnetic and ferroelectric order along with some coupling between the two are known as magnetoelectric.[8-10] Among multiferroics, magnetoelectrics are the most important and most extensively studied.[11] The coexistence of ferromagnetic and ferroelectric order in the same material is limited because the fundamental requirements for ferromagnetism and ferroelectricity are almost mutually exclusive.[3] For example, most of the

ferroelectrics are transition metal oxides, in which transition metal ions have empty d shells. On the contrary, magnetism requires transition metal ions with partially filled d shells. While a ferroelectric material must be an insulator (otherwise, an applied electric field would induce an electric current to flow, rather than causing an electrical polarization), ferromagnets although not required to have specific electrical properties are often metallic. Another important requirement for the existence of ferroelectricity is a structural distortion from the ideal high-symmetry phase that removes the center of symmetry and allows an electric polarization. There are only 31 point groups that allow a spontaneous electric polarization and similarly only 31 point groups that allow a spontaneous magnetic polarization.[1] Only thirteen point groups are found in both sets, allowing both properties to exist in the same phase.

Even though ferromagnetism and ferroelectricity are mutually exclusive, there are several novel routes to magnetic ferroelectrics like frustrated magnetism,[12-15] lone-pair effect,[16-18] charge-ordering[19-22] and local non-centrosymmetry.[23]

Barium titanate is a widely used perovskite ferroelectric oxide (yearly production: ~ 11 000 tons), with many novel properties like high-dielectric constant, large piezoelectric coefficient, low loss and lead freeness.[24,25] Depending on the temperature, $BaTiO_3$ crystallizes in five distinct polymorphic forms:[26] rhombohedral (T <183 K), orthorhombic (183 to 273 K), tetragonal (273 to 403 K), cubic (403 to 1733 K) and hexagonal (1733 K up to melting). Technologically, tetragonal and cubic phases are the most important and extensively used in a broad array of electronic devices such as multilayered ceramic capacitors (MLCCs), thermistors/thermal switches and resistors.[27] The structure of $BaTiO_3$ is a network of corner-linked oxygen octahedra, with the Ti^{4+} filling the octahedral holes and the

Ba^{2+} filling the dodecahedral holes as shown in Figure 7.1.[28-30] The coordination number of Ba^{2+} and Ti^{4+} is 12 and 6 respectively. The hybridization between empty Ti 3d states and occupied O 2p states results displacement of the Ti^{4+} ion from the centre of octrahedra. This collective shift of cations inside a periodic crystal is responsible for the bulk electric polarization.

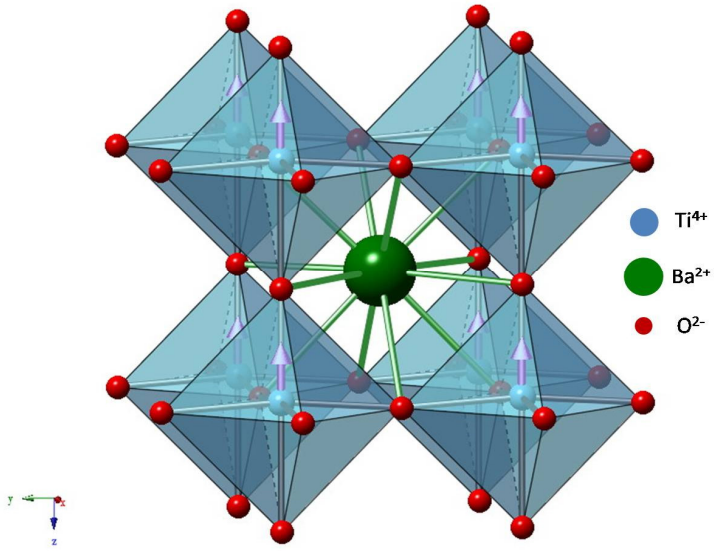

Figure 7.1: Crystal structure of $BaTiO_3$

Due to the current tendency towards the miniaturization of electronic devices, numerous research efforts have been made to prepare $BaTiO_3$ in nanometer size. But the reduction of physical sizes of ferroelectrics has a significant effect on polarization and this represents a limitation for the miniaturization process. Ferroelectricity in nanometre size $BaTiO_3$ is predicted to disappear below a critical size.[31-34] The effects of depolarization in nanometer size ferroelectrics can be explained in terms of a randomly oriented surface charge layer that begins to dominate the ordered ferroelectric interior as the size decreases.

Cobalt ferrite ($CoFe_2O_4$) is a hard magnetic material with high coercivity and moderate magnetization. These properties, along with their good physical and chemical stability, make $CoFe_2O_4$ suitable for various applications such as magnetic recording, electronic devices, information storage, magnetic resonance imaging and drug-delivery technology.[35-42] $CoFe_2O_4$ possesses a nearly inverse spinel structure of the formula $(Co_xFe_{1-x})_A[Co_{1-x}Fe_{1+x}]_B$ where A and B indicate tetrahedral and octahedral sites, respectively. The site occupancy varies from x = 0.20 to 0.07 depending on the preparation methods.[43,44] A schematic of $CoFe_2O_4$ structure is shown in Figure 7.2. The oxygen anions (O^{2-}) adopt a close-packed cubic crystal structure and the metal cations occupy the interstices in two-lattice arrangement. In each unit cell, containing 32 oxygen anions, 8 cations are coordinated by 4 oxygen (tetrahedral sites) and 16 cations are coordinated by 6 oxygen (octahedral sites).

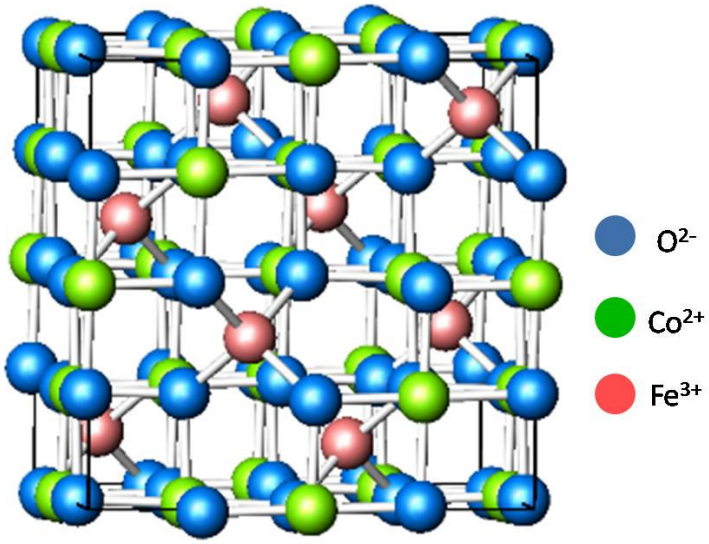

Figure 7.2: Crystal Structure of $CoFe_2O_4$

Magnetic properties of $CoFe_2O_4$ are directly related to its structure. Interactions between A-B, A-A and B-B sublattices are antiferromagnetic with A-B interaction dominating over other two interactions. As $CoFe_2O_4$ is inverse spinel, there are

nearly equal numbers of Fe^{3+} present in both A and B sublattices and they interact antiferromagnetically. Hence, net magnetic moment due to Fe^{3+} is zero and magnetism in $CoFe_2O_4$ is mainly due to Co^{2+} present in the B sublattice. The calculated and observed per molecule moment in bulk $CoFe_2O_4$ at 0 K are 3 μ_B and 3.7 μ_B respectively.[45] The deviation of observed moment from the calculated value can be attributed to the fact that Co^{2+} has some orbital moment and $CoFe_2O_4$ is not completely inverse spinel.[45] The bulk $CoFe_2O_4$ is characterized by the Curie temperature of ~790 K, saturated magnetization of ~81 emu g^{-1} and a high magnetocrystalline anisotropy constant $K_1 = 270 \times 103$ J m^{-3} at 293 K.[46, 47]

7.2 Scope of the present Investigations

Multiferroic and magnetoelectric materials are of great importance both scientifically as well as technologically. The coexistence of magnetic and electric ordering in a single material not only allows an additional degree of freedom in the design of actuators, transducers and storage device but also brings about a completely new device paradigm via the mutual coupling between the two order parameters. These properties can be realized in a few single phase materials. But single phase magnetoelectric materials are limited with disadvantages like low working temperature and inadequate magnetic and electric polarization. Van Suchtelen et al. in 1972 proposed that composites of piezoelectric and magnetostrictive phases can be electromagnetically coupled via stress mediation.[48] Subsequently, several theoretical and experimental efforts have been made to choose right pair of piezoelectric and magnetostrictive materials to achieve multiferroic and magnetoelectric properties.[49–52] Special attention has been paid to composites of $BaTiO_3$-$CoFe_2O_4$, $CoFe_2O_4$-$BiFeO_3$, and $CoFe_2O_4$-$PbTiO_3$.[43-56] Zheng et al.[53]

measured properties of nanofilms of $CoFe_2O_4$@$BaTiO_3$, where nanopillars of $CoFe_2O_4$ were embedded in a $BaTiO_3$ matrix and found a small change in magnetization at the ferroelectric transition temperature of $BaTiO_3$. Composites of $CoFe_2O_4$ with $BaTiO_3$ are reported to exhibit magnetoelectric effect by Doung et al[57] and Wie et al,[58] who suggest mechanical coupling between magnetostrictive and piezoelectric phases through magnetostrition to be responsible for the magnetoelectric effect. These workers did not, however, measured the magnetocapacitance as a function of applied magnetic field in these materials. Nanocomposites of $CoFe_2O_4$ with $Pb(Zr,Ti)O_3$ show a very small magnetocapacitance (<0.1% at 1 T) at room temperature.[59] We considered it purposeful to investigate magnetic and dielectric properties of different types of core-shell nanostructures between $CoFe_2O_4$ and $BaTiO_3$ to explore the occurrence of magnetoelectric effect in these composites. For this purpose, we have prepared $CoFe_2O_4$@$BaTiO_3$ core-shell nanoparticles as well as core-shell nanotubes.

7.3 Experimental and related aspects

7.3.1 Synthesis of core-shell nanoparticles

$CoFe_2O_4$ nanoparticles were prepared by the hydrothermal treatment of a slurry obtained by reducing 15 mL aqueous mixture of $Co(NO_3)_2$•$6H_2O$ (0.058 g), $Fe(NO_3)_3$•$9H_2O$ (0.16 g) and polyvinylpyrrolidone (0.2 g) with sodium borohydride (0.9 g dissolved in 5 mL of Millipore water) at 393 K for 12 hour.[18] We then prepared a precursor solution of $BaTiO_3$ containing a mixture of 30 ml aqueous solution of 0.029 g of $BaCO_3$ and 0.1 g of citric acid with 30 ml ethanolic solution of 1 g of citric acid and 0.048 mL titanium isopropoxide. $CoFe_2O_4$ (0.1 g) nanoparticles were dispersed in 60 ml of the $BaTiO_3$ precursor solution under vigorous sonication.

After prolong sonication, the mixture was dried at 333 K under stirring and subsequently calcined at 1053 K for 5 hours to obtain $CoFe_2O_4$@$BaTiO_3$ core-shell nanoparticles.

7.3.2 Synthesis of core-shell nanotubes

$CoFe_2O_4$ nanotubes were obtained by using polycarbonate membrane templates with a pore diameter of 220 nm. The templates were soaked overnight in a 20 mL ethylene glycol solution containing 0.047 g of $CoCl_2.6H_2O$ and 0.109 g of $FeCl_3.6H_2O$ followed by drying at 393 K and calcination at 803 K for 3 hours. These nanotubes were added into 10 mL of the $BaTiO_3$ precursor solution, sonicated for five minutes and dried at 333 K. The dried mixture was subsequently calcined at 1053 K for 5 hours to obtain $CoFe_2O_4$@$BaTiO_3$ core-shell nanotubes. $BaTiO_3$ precursor solution alone was dried at 333 K and followed by calcination at 1073 K for 5 hours to obtain $BaTiO_3$ nanoparticles.

7.3.3 Characterization techniques

X-Ray diffraction (XRD): XRD patterns were recorded at 298 K with a Bruker-D8 X-ray diffractometer using Cu-Kα radiation.

Electron Microscopy: Field emission scanning electron microscopy (FESEM) images were recorded with a field emission scanning electron microscope (FESEM, FEI Nova-Nano SEM-600, Netherlands). TEM images were recorded with a JEOL JEM 3010 instrument (Japan) operated at an accelerating voltage of 300 kV.

Magnetic Measurements: The magnetic measurements of this work were carried out by using a vibrating sample magnetometer in a Physical Property Measurement System (PPMS) of Quantum Design, USA. Hysteresis loops were recorded at different temperatures. In the temperature dependent ZFC magnetization, the sample

was cooled to lowest temperature in the absence of field, then the field was applied at the lowest temperature and the data were recorded on re-heating the sample. In the FC measurements the sample was cooled in the applied field to lowest temperature and the data were recorded on re-heating the sample, keeping the field applied.

Dielectric Measurements: For dielectric measurements, disc-shaped pellets were sintered at 773 K for 3 h, followed by gold sputtering on both sides to form a capacitor. The pellets were later heated for 2 hour at 473 K at a heating rate of 2 K/min. The electrodes were made using copper wire and silver paste. Dielectric measurements were carried out on such samples with a Precision Impedance Analyser (Agilent 4294 A) in the frequency range of 100 Hz to 1 MHz. The ferroelectric measurements on theses samples have been carried out using Radiant Technologies Precision Workstation. Magneto-dielectric measurements were carried out using a cryo-cooled closed cycle superconducting magnet by applying 0 to 2.3 T magnetic fields.

7.4 Results and discussion

7.4.1 Core-shell nanoparticles

$CoFe_2O_4$ nanoparticles used as the starting materials for the preparation of core-shell $CoFe_2O_4$@$BaTiO_3$ nanoparticles were shown in Figure 7.3 (a). The size of these agglomerating magnetic nanoparticles was found to be around 12 nm. A dispersion of $CoFe_2O_4$ nanoparticles in $BaTiO_3$ precursor solution was dried under vigorous magnetic stirring and the dried sample was examined under TEM. This sample was comprised of core-shell nanostructures with few $CoFe_2O_4$ nanoparticles encapsulated within an amorphous shell as can be seen from the TEM image of Figure 7.3 (b). Upon calcination at high temperature this sample yields core-shell

$CoFe_2O_4$@$BaTiO_3$ nanoparticles as shown in the TEM image of Figure 7.3 (c). The diameter of these core-shell nanoparticles was between 40 and 60 nm, with the ferrite particles at the core with an average thickness of $BaTiO_3$ shell being ~ 18 nm.

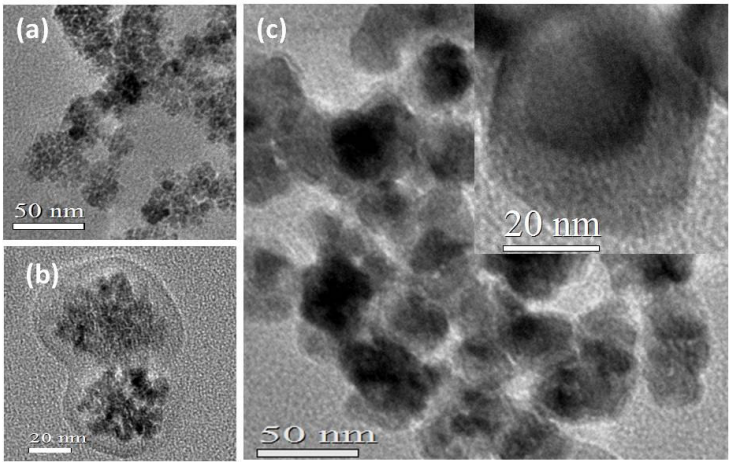

Figure 7.3: TEM images of (a) $CoFe_2O_4$ nanoparticles, (b) $CoFe_2O_4$ nanoparticles encapsulated within an amorphous shell and (c) $CoFe_2O_4$@$BaTiO_3$ core-shell nanoparticles (inset shows magnified TEM image of a core-shell nanoparticles).

The inset of Figure 7.3 (c) shows magnified TEM image of a $CoFe_2O_4$@$BaTiO_3$ core-shell nanoparticles. Selected area electron diffraction pattern of the core-shell nanoparticles shows them to be mixtures of $CoFe_2O_4$ and $BaTiO_3$. The powder XRD

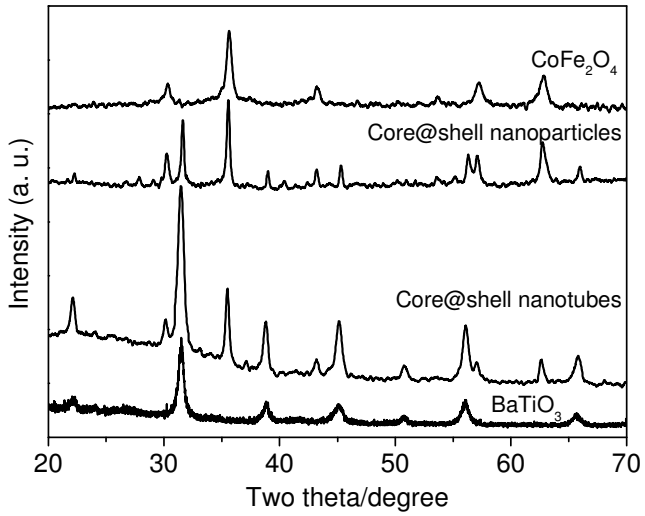

Figure 7.4: XRD patterns of $CoFe_2O_4$, $BaTiO_3$ and core-shell nanostructures.

patterns of core-shell nanostructures were compared with XRD patterns of $BaTiO_3$ and $CoFe_2O_4$ nanoparticles (see Figure 7.4). All the peaks of the patterns can be indexed to the pure phase of tetragonal $BaTiO_3$ and cubic $CoFe_2O_4$.

$CoFe_2O_4$ nanoparticles showed a large divergence between field cooled (FC) and zero field cooled (ZFC) magnetization data in the 10-390 K range at 100 Oe, the divergence increases with decreasing temperature (see Figure 7.5 (a)).[60,61] These nanoparticles exhibit magnetic hysteresis at 300 K, shown in the inset of Figure 7.5 (a). The saturation magnetization (M_s), remanent magnetization (M_r) and coercive field (H_c) of $CoFe_2O_4$ nanoparticles were found to be 60 emu/g, 12 emu/g and 166 Oe, respectively, these values are smaller than the that of bulk $CoFe_2O_4$ as expected.[62]

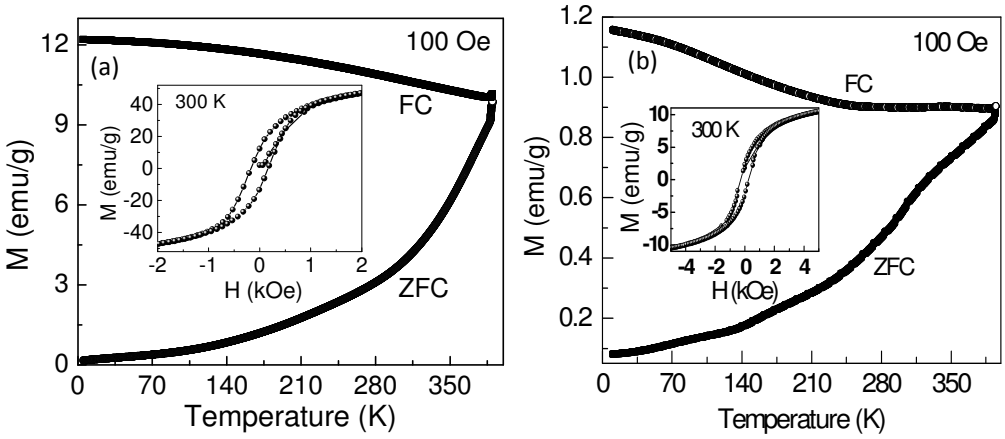

Figure 7.5: Temperature dependence of the magnetization under FC and ZFC conditions of (a) $CoFe_2O_4$ nanoparticles and (b) $CoFe_2O_4$@$BaTiO_3$ core-shell nanoparticles. Insets show respective magnetic hysteresis loops at 300 K.

The FC and ZFC magnetization data of $CoFe_2O_4$@$BaTiO_3$ core-shell nanoparticles at 100 Oe field shows large divergence (Figure 7.5 (b)) just as the $CoFe_2O_4$ nanoparticles. The ZFC plot also shows a shoulder around 140 K similar to the feature reported in the literature.[61] The core-shell nanoparticles also show magnetic hysteresis at 300 K (see inset of Figure 7.5 (b)), the M_s and M_r values

being 13 emu/g and 2.4 emu/g, these values are lower than those of pure $CoFe_2O_4$ nanoparticles (the M_s and M_r values of the core-shell nanoparticles calculated on the basis of the weight of $CoFe_2O_4$ alone are 20 emu/g and 4 emu/g, respectively). The coercive field, however, increases to 264 Oe in the core-shell particles, probably because the magnetization becomes harder in the presence of nonmagnetic shell.[63]

Temperature-dependence of the dielectric constant of $BaTiO_3$ nanoparticles (diameter ~20 nm) and $CoFe_2O_4$@$BaTiO_3$ core-shell nanostructures were measured at different frequencies (1 kHZ to 1 MHZ). In the case of $BaTiO_3$ nanoparticles, the temperature-dependent dielectric constant exhibits a peak at around 400 K,

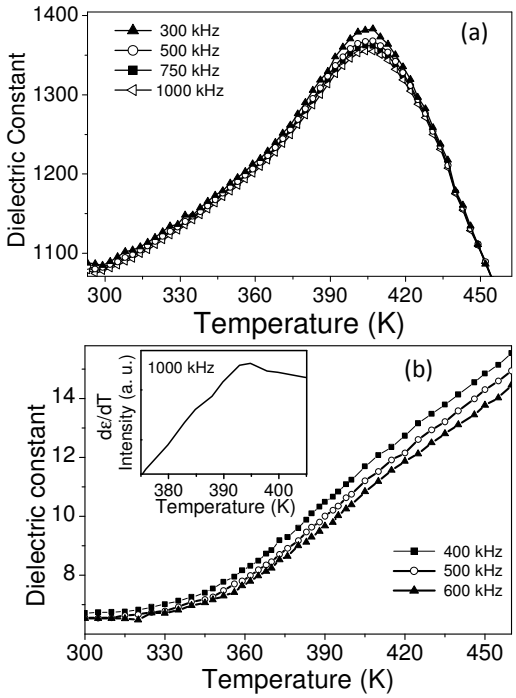

Figure 7.6: Temperature dependence of dielectric constant of (a) $BaTiO_3$ nanoparticles and (b) $CoFe_2O_4$@$BaTiO_3$ core-shell nanoparticles. Inset shows derivative of the dielectric constant as a function of temperature.

corresponding to the ferroelectric T_c of bulk $BaTiO_3$[64] (Figure 7.6 (a)). In Figure 7.6 (b), we show dielectric constant of $CoFe_2O_4$@$BaTiO_3$ core-shell nanoparticles as a

function of temperature. The dielectric constant increases with increasing temperature with a clear hump at ~ 390 K. Inset of Figure 7.6 (b) shows derivative of the dielectric constant as a function of temperature in order to demonstrate the transition around 390 K. The dielectric constant increases with decreasing frequency, but the T_c does not change significantly with frequency. $BaTiO_3$ nanoparticles as well as $CoFe_2O_4$@$BaTiO_3$ core-shell nanoparticles do not exhibit good saturating ferroelectric hysteresis loops (Figure7.7). The instability of the ferroelectric phase depends on factors such as smaller grain size, defect chemistry, incorporation of $CoFe_2O_4$, presence of hydroxyl groups, porosity level and residual stresses and it is difficult to separate one effect from another.[65,66] From the available data, we find

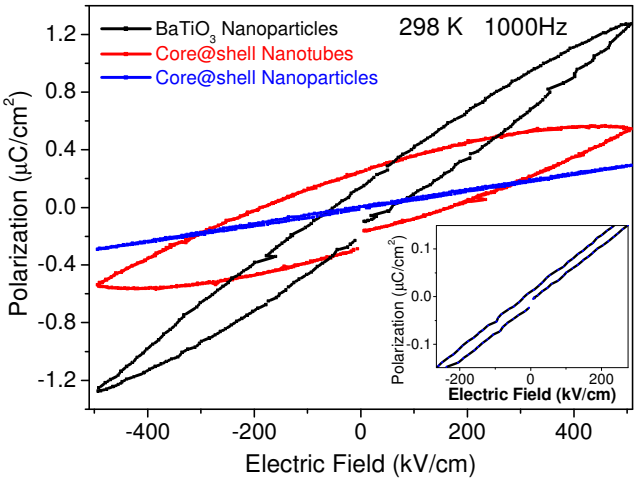

Figure 7.7: Ferroelectric hysteresis loops of $BaTiO_3$ nanoparticles and $CoFe_2O_4$@$BaTiO_3$ core-shell nanostructures. Inset shows magnified ferroelectric hysteresis loops of core-shell nanoparticles.

that the coercive polarization (P_c) and remnant polarization (P_r) to be 51 kV/cm and 0.13 μC/cm^2 respectively for $BaTiO_3$ nanoparticles, the corresponding values for core-shell nanoparticles being 13 kV/cm and 0.02 μC/cm^2 respectively. Figure 7.8 (a) shows the temperature dependence of the dielectric constant in the temperature

range of 45 to 315 K in the absence and presence of 1 T magnetic field. Both the curves show a transition around 170 K which corresponds to the rhombohedral-orthorhombic phase transition (T_{ro}) of $BaTiO_3$.[64] A decrease in the dielectric

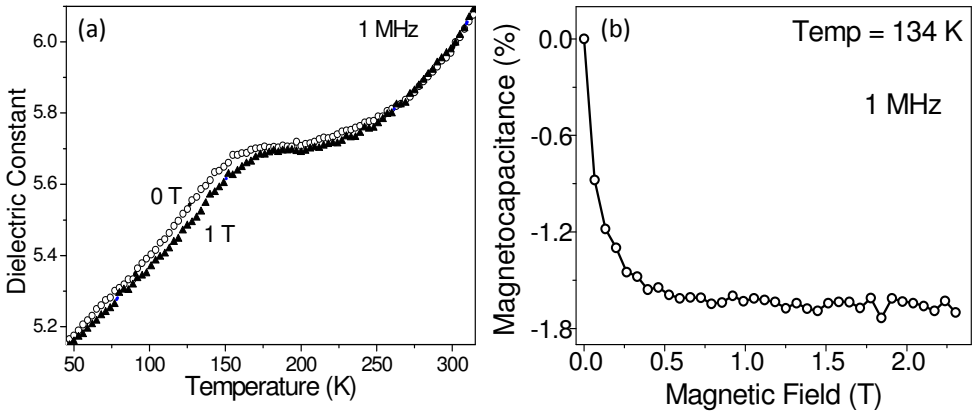

Figure 7.8: (a) Temperature variation in dielectric constant of $CoFe_2O_4$@$BaTiO_3$ core-shell nanoparticles and (b) magnetocapacitance as a function of magnetic field at 134 K.

constant is observed below T_{ro} on application of the magnetic field, showing the presence of magnetoelectric effect in the core-shell structure. Figure 7.8 (b) shows the magnetocapacitance of the sample as a function of magnetic field at 134 K. The magnetocapacitance increases with increasing magnetic field till 0.5 T accounting for ~ 1.7 % change, but is independent of frequency.

7.4.2 Core-shell nanotubes

$CoFe_2O_4$ nanotubes obtained by using polycarbonate membrane as a template were used as the starting material for the synthesis of $CoFe_2O_4$@$BaTiO_3$ nanotubes. Figure 7.9 (a) shows a TEM image of $CoFe_2O_4$ nanotubes having an outer diameter of ~ 80 nm. The high-temperature reaction of $BaTiO_3$ precursor solution with these nanotubes yields $CoFe_2O_4$@$BaTiO_3$ nanotubes. TEM investigation reveals that the core-shell nanotubes were comprised of $CoFe_2O_4$ nanotubes with $BaTiO_3$ nanoparticles of ~ 15 nm size sticking on its walls. The outer diameter of these

nanotubes was found to be around 100 nm (see FESEM and TEM image in Figure 7.9 (b) and (c) respectively). X-ray diffraction (shown in Figure 7.4) and selected area electron diffraction patterns confirms that core-shell nanotubes were made up of pure phase of $CoFe_2O_4$ and $BaTiO_3$.

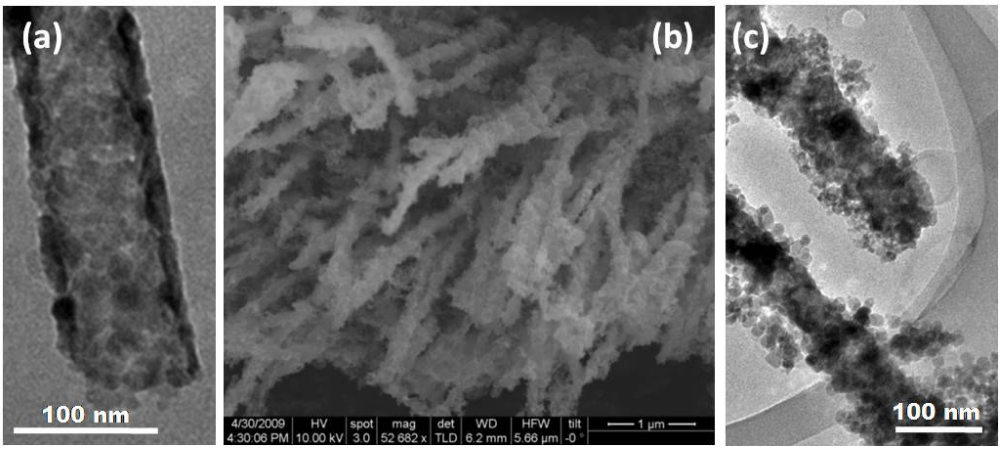

Figure 7.9: (a) TEM images of $CoFe_2O_4$ nanotubes, (b) FESEM and (c) TEM image of $CoFe_2O_4$@$BaTiO_3$ core-shell nanotubes.

Similar to $CoFe_2O_4$ nanoparticles, $CoFe_2O_4$ nanotubes also showed large divergence between field cooled (FC) and zero field cooled (ZFC) magnetization

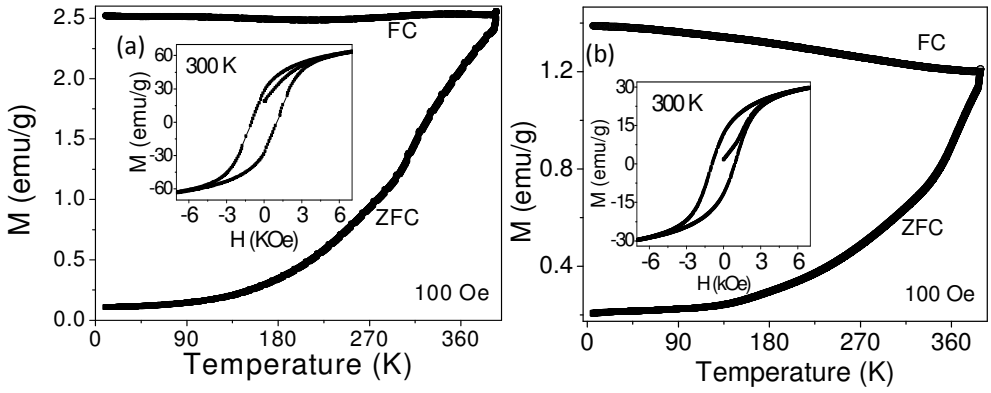

Figure 7.10: Temperature dependence of the magnetization under FC and ZFC conditions of (a) $CoFe_2O_4$ nanotubes and (b) $CoFe_2O_4$@$BaTiO_3$ core-shell nanotubes. Insets show the respective magnetic hysteresis loops at 300 K.

data at 100 Oe and exhibited magnetic hysteresis at 300 K (Figure 7.10 (a)). The M_s, M_r and H_c values of $CoFe_2O_4$ nanotubes were 75 emu/g, 28 emu/g, and 901 Oe, respectively.

Magnetization data of the $CoFe_2O_4$@$BaTiO_3$ core-shell nanotubes also reveal divergence between FC and ZFC plots similar to the core-shell nanoparticles (Figure 7.10 (b)). We observe magnetic hysteresis at 300 K with M_s and M_r values of 28 and 12 emu/g, respectively, (the M_s and M_r values corresponding to the weight percent contribution of $CoFe_2O_4$ core alone are 40 emu/g and 16 emu/g, respectively). The decrease in magnetization of $CoFe_2O_4$ in the core-shell structures could be due to magnetostriction[53,59] as well as lattice mismatch with $BaTiO_3$.[53] Similar reduction in magnetic moment has been observed in the case of $CoFe_2O_4$ dispersed in a $PbTiO_3$ matrix due to the dissolution of Ti in the interface.[67,68] The H_c of the core-shell nanotubes is 912 Oe, comparable to that of pure $CoFe_2O_4$ nanotubes.

.

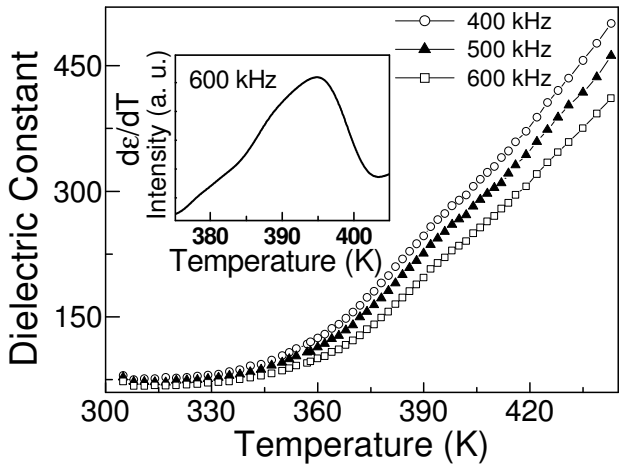

Figure 7.11: Temperature dependence of dielectric constant of $CoFe_2O_4$@$BaTiO_3$ core-shell nanotubes. Inset shows derivative of the dielectric constant to demonstrate the transition at 396 K.

Temperature variation in the dielectric constant of the core-shell nanotubes shows a transition at 396 K corresponding to tetragonal to cubic phase transition of $BaTiO_3$[66] (see Figure 7.11). The P_c and P_r values obtained from the dielectric hysteresis of the core-shell nanotubes are 185 kV/cm and 0.24 μC/cm^2, respectively, values larger than those of the nanoparticles (Figure 7.7). Figure 7.12 (a) shows the temperature variation in the dielectric constant at low temperatures on application of a magnetic field. The dielectric constant decreases with increase in magnetic field above 270 K, close to the orthorhombic to tetragonal phase transition temperature. The magnetocapacitance of core-shell nanotubes at 310 K is shown as a function of magnetic field in Figure 7.12 (b). The magnetocapacitance increases monotonically with increasing magnetic field till 2.1 T, exhibiting a substantial change of 4.5%.

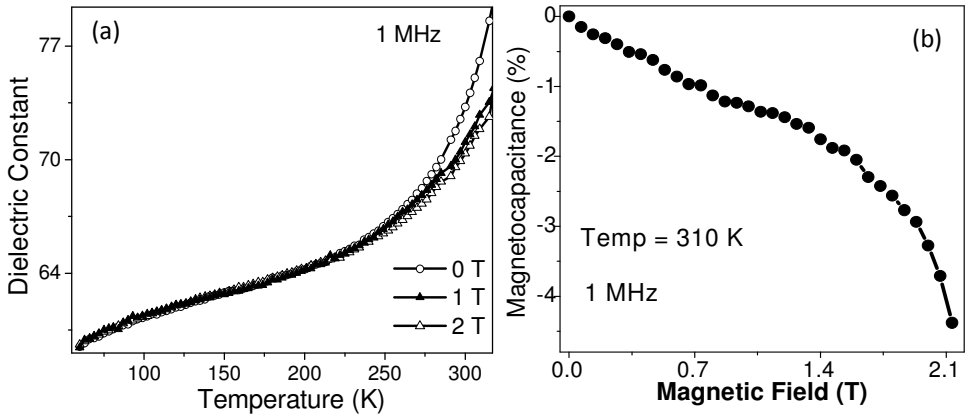

Figure 7.12: (a) Temperature variation in dielectric constant of $CoFe_2O_4$@$BaTiO_3$ core-shell nanotubes and (b) magnetocapacitance as a function of magnetic field at 134 K.

The 4.5% change in magnetocapcitance for core-shell nanotubes found here is a significant improvement over that of the core-shell nanoparticles (1.7%) and is the highest value reported so far in the $CoFe_2O_4$@$BaTiO_3$ system. Furthermore, magnetocapacitance is independent of the frequency of measurement. The maximum magnetocapacitance is observed at different structural transition temperatures of

$BaTiO_3$ for the nanoparticles and nanotubes. This may be because the magnetic moment is high in the different temperature regimes in the case of nanoparticles and nanotubes, the temperature being low (134 K) in the case of former. Furthermore, the smaller size of the $BaTiO_3$ nanoparticles on the $CoFe_2O_4$ nanotubes may wipe out the 170 K transition.

7.5 Conclusions

In conclusion, core-shell $CoFe_2O_4$@$BaTiO_3$ nanoparticles and nanotubes exhibit magnetic hysteresis at room temperature and show magnetoelectric effect. The results obtained with core-shell nanotubes are noteworthy since we observe a 4.7% change in magnetocapacitance at 310 K. The larger change in magnetocapacitance of the core-shell nanotubes may arise from the larger saturation magnetization and remanent magnetization of the nanotubes.

References

1. H. Schmid, *Ferroelectrics*, **162**, *317,* 1994.

2. L. Yan, Y. Yang, Z. Wang, Z. Xing, J. Li and D. Viehland, *J. Mater. Sci.*, **44,** *5080,* 2009.

3. N. A. Hill, *J. Phys. Chem. B*, **104**, *6694*, 2000.

4. R. Ramesh and N. A. Spaldin, *Nature mater.*, **6,** *21,* 2007.

5. J. Li, I. Levin, J. Slutsker, V. Provenzano, P. K. Schenck, R. Ramesh, J. Ouyang and A. L. Roytburd, *Appl. Phys. Lett.,* **87**, *072909*, 2005.

6. J. Barbosa, B. G. Almeida, J. A. Mendes, A. G. Rolo, J. P. Araujo and J. B. Sousa, *J. Appl. Phys.,* **101**, *09M101,* 2007.

7. I. Levin, J. Li, J. Slutsker and A. L. Roytburd, *Adv. Mater.*, **18**, *2044,* 2006.

8. T. Kimura, T. Goto, H. Shintani, K. Ishizaka, T. Arima and Y. Tokura, *Nature*, **426,** *55,* 2003.

9. W. Eerenstein, N. D. Mathur and J. F. Scott, *Nature*, **442**, *759,* 2006.

10. C. W. Nana, M. I. Bichurin, S. Dong and D. Viehland and G. Srinivasan, *J. Appl. Phys.*, **103**, *031101*, 2008.

11. V. E. Wood and A. E. Austin, *Int. J. Magn.*, **5**, *303,* 1974.

12. T. Lottermoser, T. Lonkai, U. Amann, D. Hohlwein, J. Ihringer and M. Fiebig, *Nature,* **30**, *541,* 2004.

13. N. Hur, S. Park, P. A. Sharma, J. S. Ahn, S. Guha and S. W. Cheong, *Nature,* **429**, *392,* 2004.

14. J. A. Alonso, M. T. Casais, M. J. Martnez-Lope and I. Rasines, *J. Solid State Chem.*, **129**, *105,* 1997.

15. S. C. Abrahams and J. L. Bernstein, *J. Chem. Phys.*, **46**, *3776,* 1967.

16. J. R. Teague, R. Gerson and W. J. James, *Solid State Commun.*, **8**, *1073*, 1970.

17. A. M. D. Santos, S. Parashar, A. R. Raju, Y. S. Zhao, A. K. Cheetham and C. N. R. Rao, *Solid State Commun*., **122**, *49*, 2002.

18. Y. F. Popov, A. M. Kadomtseva, G. P. Vorobev and A. K. Zvezdin, *Ferroelectrics,* **162**, *135,* 1994.

19. V. B. Shenoy, D. D. Sarma and C. N. R. Rao, *Chem. Phys. Chem.*, **7**, *2053,* 2006.

20. C. N. R. Rao, *J. Phys. Chem. B,* **104**, *5877,* 2000.

21. S. Parashar, L. Sudheendra, A. R. Raju and C. N. R. Rao, *J. Appl. Phys.*, **95,** *2181*, 2004.

22. A. Guha, N. Khare, A. K. Raychaudhuri and C. N. R. Rao, *Phys. Rev. B: Condens. Matter*, **62**, *R11941*, 2000.

23. K. Ramesha, A. Llobet, T. Proffen, C. R. Serrao and C. N. R. Rao, *J. Phys.: Condens. Matter*, **19**, *102202,* 2007.

24. W. Maison, R. Kleeberg, R. B. Heimann and S. Phanichphant, *J. Euro. Ceram. Soc.*, **23**, *127*, 2003.

25. M. T. Buscaglia, V. Buscaglia, and R. Alessio, *Chem. Mater.***, 19***, 711***,** 2007.

26. D. Young and B. Lee, *J. Ceram. Process. Res*., **3**, *41*, 2002.

27. M. Hu, G. Miller, E. Payzant and C. Rawn, *J. Mater. Sci.*, **35**, *2927,* 2000.

28. V. M. Goldschmidt. *Shrifter Nofke Videnskaps-Akad. Oslo I: mat-Naturv. Kl.*, **2**, *8*, 1926.

29. H. D. Megaw, *Nature*, **155**, *484,* 1945.

30. S. Miyake and R. Ueda, *J. Phys. Soc. Jap.,* **1**, *32*, 1946.

31. J. Hong and D. Fang, *Appl. Phys. Lett*., **92**, *012906,* 2008.

32. G. Geneste, E. Bousquet, J. Junquera and P. Ghosez, *Appl. Phys. Lett.*, **88**, *112906,* 2006.

33. R. Bottcher, C. Klimm, D. Michel, H. C. Semmelhack, G. Volkel, H. J. Glasel and E. Hartmann, *Phys. Rev. B*, **62**, *2085,* 2000.

34. W. L. Zhong, Y. G. Wang, P. L. Zhang and B. D. Qu, *Phys. Rev. B*, **50**, *698,* 1994.

35. V. Pallai and D. O. Shah, *J. Magnet. Magnet. Mater.*, **163**, *243-248,* 1996.

36. R Skomski, *J. Phys.: Condens. Matter.,* **15**, *R1*, 2003.

37. F. Caruso, M. Spasova, A. Susha, M. Giersig and R. A. Caruso, *Chem. Mater.*, **13**, *109*, 2001.

38. T. Hyeon, *Chem. Commun.*, **8**, *927*, 2003.

39. T. Hyeon, Y. Chung, J. Park, S. S. Lee, Y. W. Kim and B. H. Park, *J. Phys. Chem. B*, **106**, *6831*, 2002.

40. T. Hyeon, S. S. Lee, J. Park, Y. Chung and H. B. Na, *J. Am. Chem. Soc.*, **123***, 12798,* 2001.

41. S. Yu and M. Yoshimura, *Adv. Funct. Mater.*, **12**, *9*, 2002.

42. S. Yu and M. Yoshimura, *Chem. Mater.*, **12**, *3805,* 2000.

43. G. A. Sawatzky, F. V. D. Moude and A. K. Morrish, *J. Appl. Phys.*, **39**, *1204*, 1968.

44. M. Veverka, P. Veverka, O. Kaman, A. Lancok, K. Zaveta, E. Pollert, K. Knızek, J. Bohacek, M. Benes, P. Kaspar, E. Duguet and S. Vasseur, *Nanotechnology,* **18**, *345704*, 2007.

45. B. D. Cullity and C. D. Graham, *Introduction to magnetic materials*, 2nd edition, Wiley, New Jersey, 2009.

46. N. Bloembergen *Proc. Inst. Radio Eng.*, **44**, *1259*, 1956.

47. P. E. Tannenwald, *Phys. Rev.*, **99**, *463,* 1955.

48. J. Van Suchtelen, *Philips Res. Rep.* **27**, *28,* 1972.

49. R. E. Newnham and S. Trolier-McKinstry, *J. Appl. Crystallogr.,* **23**, *447*, 1990.

50. J. V. D. Boomgaard, A. M. J. G. V. Run and J. V. Suchtelen, *Ferroelectrics* **14**, *727*, 1976.

51. M. I. Bichurin, V. M. Petrov, Y. V. Kiliba and G. Srinivasan, *Phys. Rev. B,* **66**, *13404,* 2002.

52. J. Ryu, S. Priya, K. Uchino and H. E. Kim, *J. Electroceramics,* **8**, *107*, 2002.

53. H. Zheng, J. Wang, S. E. Lofland, Z. Ma, L. M. Ardabili, T. Zhao, L. S. Riba, S. R. Shinde, S. B. Ogale, F. Bai, D. Viehland, Y. Jia, D. G. Schlom, M. Wuttig, A. Roytburd and R. Ramesh, *Science*, **303**, *661*, 2004.

54. H. M. Zheng, Q. Zhan, F. Zavaliche, M. Sherburne, F. Straub, M. P Cruz, L. Q. Chen, U. Dahmen and R. Ramesh, *Nano Lett.*, **6**, *1401,* 2006.

55. F. Zavaliche, H. Zheng, L. M. Ardabili, S. Y. Yang, Q. Zhan, P. Shafer, E. Reilly, R. Chopdekar, Y. Jia and P. Wright, *Nano Lett.,* **5**, *1793,* 2005.

56. I. Levin, J. Li, J. Slutsker and A. L. Roytburd, *Adv. Mater*., **18**, *204447,* 2006.

57. G. V. Duong and R. Groessinger, *J. Magn. Magn. Mater*., **316**, *624,* 2007.

58. J. Nie, G. Xu, Y. Yang and C. Cheng, *Mater. Chem. Phys*., **115**, *400*, 2009.

59. X Gao, B. J. Rodriguez, L. Liu, B. Birajdar, D. Pantel, M. Ziese, M. Alexe and D. Hesse, *ACS Nano,* **4**, *1099*, 2010.

60. Z. Gu, X. Xiang, G. Fan and F. Li, *J. Phys. Chem. C,* **47**, *18459*, 2008.

61. Z. Wang, X. Liu, M. Lv, P. Chai, Y. Liu, X. Zhou and J. Meng, *J. Phys. Chem. C*, **112**, *15171*, 2008.

62. M. Grigorova, H. J. Blythe, V. Rusanov, V. Petkov, V. Masheva, D. Nihtianova, L. M. Martinez, J. S. Munoz and M. Mikhov, *J. Magn. Magn. Mater.*, **183**, *163,* 1998.

63. H. F. Zhang, S. W. Or and H. L. W. Chan, *Mater. Res. Bull*., **44**, *1339*, 2009.

64. C. Kittel, *Introduction to Solid State Physics*, 7th ed. Wiley, New York, 1995.

65. U. A. Joshi, S. Yoon, S. Baik and J. S. Lee, *J. Phys. Chem. B*, **110**, *12249*, 2006.

66. E. K. Akdogan, M. R. Leonard and A. Safari, *Handbook of Low and High Dielectric Constant Materials and Their Applications*, (Ed: H. S. Nalwa), Academic, New York, **2**, *61*, 1999.

67. J. Li, I. Levin, J. Slutsker, V. Provenzano, P. K. Schenck, R. Ramesh, J. Ouyang, and A. L. Roytburd, *Appl. Phys. Lett.*, **87**, *072909*, 2005.

68. P. Nathwani and V. S. Darshane, *J. Phys. C*, **21**, *3191*, 1988.